

University of Alberta

*Three Dimensional Multimode Interference
for Optical Layer Routing*

by

Nan Xie ©

A thesis submitted to the Faculty of Graduate Studies and Research in partial fulfillment of the requirements for the degree of *Master of Science*

Department of *Electrical and Computer Engineering*

Edmonton, Alberta

Spring 2006



Library and
Archives Canada

Bibliothèque et
Archives Canada

Published Heritage
Branch

Direction du
Patrimoine de l'édition

395 Wellington Street
Ottawa ON K1A 0N4
Canada

395, rue Wellington
Ottawa ON K1A 0N4
Canada

Your file *Votre référence*

ISBN: 0-494-13912-9

Our file *Notre référence*

ISBN: 0-494-13912-9

NOTICE:

The author has granted a non-exclusive license allowing Library and Archives Canada to reproduce, publish, archive, preserve, conserve, communicate to the public by telecommunication or on the Internet, loan, distribute and sell theses worldwide, for commercial or non-commercial purposes, in microform, paper, electronic and/or any other formats.

The author retains copyright ownership and moral rights in this thesis. Neither the thesis nor substantial extracts from it may be printed or otherwise reproduced without the author's permission.

AVIS:

L'auteur a accordé une licence non exclusive permettant à la Bibliothèque et Archives Canada de reproduire, publier, archiver, sauvegarder, conserver, transmettre au public par télécommunication ou par l'Internet, prêter, distribuer et vendre des thèses partout dans le monde, à des fins commerciales ou autres, sur support microforme, papier, électronique et/ou autres formats.

L'auteur conserve la propriété du droit d'auteur et des droits moraux qui protègent cette thèse. Ni la thèse ni des extraits substantiels de celle-ci ne doivent être imprimés ou autrement reproduits sans son autorisation.

In compliance with the Canadian Privacy Act some supporting forms may have been removed from this thesis.

Conformément à la loi canadienne sur la protection de la vie privée, quelques formulaires secondaires ont été enlevés de cette thèse.

While these forms may be included in the document page count, their removal does not represent any loss of content from the thesis.

Bien que ces formulaires aient inclus dans la pagination, il n'y aura aucun contenu manquant.


Canada

To Mom and Dad

Abstract

The theory of Three-dimensional multimode interference (3DMMI) is presented in this thesis. Simulation of 3DMMI has illustrated various imaging possibilities for optical layer routing. 3DMMI waveguides have been analyzed for their performance in terms of imaging quality and parameter or fabrication tolerances.

Two-layer routing promises to benefit a variety of applications requiring routing optical signals from one layer to another vertical layer of waveguides. Three-dimensional multimode interference two layer routing (3DMMI-2LR) is also introduced for the first time.

The optically transparent polymer SU-8 was used to fabricate 3DMMI structures because of its chemical, physical, and optical properties. The 3DMMI waveguides have been characterized for power loss and visual 3DMMI imaging.

Acknowledgement

I want to extend my sincere gratitude to my mom Shu-Yun and dad Rui-Xiang for their emotional and living support throughout my early education and my pursuit of this degree. I am forever grateful for their continuing support and encouragement of my career. I am also forever grateful for the love, support, and motivation from my best friend and my love, Miyuki.

I sincerely thank my supervisor Dr. James N. McMullin and co-supervisor Dr. Christopher J. Haugen for their guidance, teachings, and mentoring. I want to thank Dr. Ray G. DeCorby for connecting me to TRILabs, the site of my research, his help, and for reviewing my thesis. I want to thank Dr. Haugen and TRILabs for providing me the financial and technical resources to complete my degree. I am also thankful to Hue Nguyen and the Nanofab facility staff for their teachings and assistance. I want to thank lab manager David Clegg for his assistance in product ordering and set-ups in the lab. I want to extend my gratitude to the TRILabs staff and students for discussions, help, and social conversations. To Dr. M. David Checkel, thank you for your involvement in my thesis examination and further review of my thesis. Lastly, I thank my 'bottle army' of 106 for giving me the strength and perseverance during the many hours day and night at my desk.

Table of Contents

[1] Introduction	1
1.1 Progress of Communication.....	1
1.2 The Electrical Bottleneck.....	1
1.3 Optical Communication	3
1.4 Integrated Optics.....	5
1.5 The MMI.....	6
1.6 Two Dimensional Imaging.....	9
1.7 Thesis Objective.....	10
1.8 Thesis Organization	12
[2] 3DMMI Theory and Simulation.....	13
2.1 Introduction.....	13
2.2 Optical Waveguide Theory.....	13
2.2.1 Planar Waveguides	13
2.2.2 Rectangular Dielectric Waveguide.....	15
2.3 MMI Theory.....	17
2.3.1 Modal Propagation Analysis	17
2.3.2 Propagation Constants and the Effective Width	18
2.3.3 MMI Imaging.....	20
2.4 3DMMI Imaging	24
2.4.1 3DMMI Modal Propagation Analysis.....	24
2.4.2 3DMMI Propagation Constants and the Effective Widths.....	26
2.4.3 3DMMI Imaging Equations	27
2.5 3DMMI Simulation.....	33
2.5.1 Simulation Tools and Conditions	33
2.5.2 Initial Simulation	33
[3] Imaging and Tolerance Analysis.....	45

3.1	Introduction.....	45
3.2	Imaging Length and Quality	45
3.2.1	Image Periodicity	45
3.2.2	Image Range	48
3.2.3	Image Resolution	50
3.3	Input Characteristics	51
3.3.1	Input Halfwidth.....	51
3.3.2	Input Location.....	54
3.3.3	Input Wavelength	56
3.3.4	Input Polarization.....	57
3.4	Waveguide Characteristics.....	59
3.4.1	Refractive Index.....	59
3.4.2	Waveguide Width.....	61
3.5	Additional Analysis.....	63
3.5.1	Fabrication Tolerances	63
3.5.2	Optical Bandwidth	68
[4]	3DMMI Application and Design.....	69
4.1	3DMMI Applications.....	69
4.1.1	The Advantage of 3DMMI.....	69
4.1.2	Two-Layer Devices	69
4.2	3DMMI 2-Layer Routing.....	70
[5]	3DMMI Fabrication.....	78
5.1	Introduction.....	78
5.2	The SU-8 Polymer	78
5.2.1	Optical Polymers.....	78
5.2.2	Properties of SU-8.....	78
5.2.3	Existing SU-8 Optical Waveguides and Structures.....	80
5.3	3DMMI Fabrication Process and Results	82

5.3.1	General Fabrication Process	82
5.3.2	Fabrication Process Results	86
[6]	3DMMI Characterization	92
6.1	Introduction.....	92
6.2	Test Setup.....	92
6.3	Power Loss Measurements	93
6.3.1	Insertion Loss.....	93
6.3.2	Propagation and Coupling Loss	94
6.4	3DMMI Imaging.....	95
[7]	Summary and Future Endeavors	101
7.1	Summary of Project	101
7.2	Future Endeavors	102
	List of References.....	104
	Appendix A: Matlab Calculation Codes/Analysis Plots.....	112
	Appendix B: Detailed SU-8 2050 Process Steps.....	122

List of Tables

<i>Table 2-1: General Interference Single Images</i>	21
<i>Table 2-2: Summary of 3DMMI Image Lengths</i>	32
<i>Table 2-3: Simulation of General Interference Self-Image</i>	34
<i>Table 2-4: Simulation of General Interference Mirror X-Y Image</i>	35
<i>Table 2-5: Simulation of General Interference 2x2 Images</i>	36
<i>Table 2-6: Simulation of General Interference Mirror X Image</i>	37
<i>Table 2-7: Simulation of General Interference Mirror Y Image</i>	38
<i>Table 2-8: Simulation of Restricted Interference Symmetric-X Image</i>	39
<i>Table 2-9: Simulation of Restricted Interference Symmetric-Y Image</i>	40
<i>Table 2-10: Simulation of Restricted Interference Symmetric-XY Image</i>	42
<i>Table 2-11: Simulation of Restricted Paired Interference XY Image</i>	43
<i>Table 3-1: Periodicity of 3DMMI (Symmetric Imaging)</i>	47
<i>Table 3-2: 3DMMI Initial Simulation Image Range</i>	50
<i>Table 3-3: 3x3 Symmetrical Images with Different HW</i>	53
<i>Table 3-4: MxN Symmetrical Images with HW 3.33μm</i>	54
<i>Table 3-5: Imbalance by Input Shifts</i>	55
<i>Table 3-6: W_x and W_y Deviation Effect on Symmetrical Images</i>	63
<i>Table 3-7: Fabrication Tolerance of 3DMMI ($w_0 = 6.66\mu$m)</i>	67
<i>Table 4-1: 3DMMI-2LR Small Dimensions Design</i>	72
<i>Table 4-2: 3DMMI-2LR Simulated Images-Small Dimensions</i>	73
<i>Table 4-3: Power Loss of 3DMMI-2LR for Small Dimensions</i>	73
<i>Table 4-4: 3DMMI-2LR Large Dimensions Design</i>	74
<i>Table 4-5: 3DMMI-2LR Simulated Images-Large Dimensions</i>	76
<i>Table 5-1: Physical and Optical Properties of SU-8 Photoresist</i>	79
<i>Table 6-1: SU-8 Waveguide Propagation and Total Coupling Loss</i>	95

List of Figures

<i>Fig. 1-1: TIR</i>	4
<i>Fig. 1-2: (a) Conventional 2-Mode Interference (b) 2x2 MMI Coupler</i>	6
<i>Fig. 1-3: General Tapered MMI Coupler</i>	8
<i>Fig. 1-4: General Schematic of MIP-S</i>	9
<i>Fig. 1-5: 3D Waveguide Side View</i>	10
<i>Fig. 1-6: (a) Two Dimensional 6 Images (b) Two Dimensional 64 Images</i>	11
<i>Fig. 2-1: Planar Optical Waveguide</i>	14
<i>Fig. 2-2: Planar Waveguide Modes</i>	14
<i>Fig. 2-3: General Rectangular Dielectric Waveguide</i>	16
<i>Fig. 2-4: Effective Index Method</i>	19
<i>Fig. 2-5: Goos-Hänchen Shifts</i>	19
<i>Fig. 2-6: General Interference Imaging</i>	22
<i>Fig. 2-7: Restricted Symmetric Interference Imaging</i>	24
<i>Fig. 2-8: 3DMMI Rectangular Waveguide</i>	25
<i>Fig. 2-9: General Self-Image Input Field</i>	34
<i>Fig. 2-10: General Self-Image Output Field</i>	34
<i>Fig. 2-11: General Mirror X-Y Input Field</i>	35
<i>Fig. 2-12: General Mirror X-Y Output Field</i>	35
<i>Fig. 2-13: General 2x2 Images Input Field</i>	36
<i>Fig. 2-14: General 2x2 Images Output Field</i>	36
<i>Fig. 2-15: General Mirror X Input Field</i>	37
<i>Fig. 2-16: General Mirror X Output Field</i>	37
<i>Fig. 2-17: General Mirror Y Input Field</i>	38
<i>Fig. 2-18: General Mirror Y Output Field</i>	38
<i>Fig. 2-19: Restricted Symmetric-X Input Field</i>	39
<i>Fig. 2-20: Restricted 1 X-Axis Image Output Field</i>	39
<i>Fig. 2-21: Restricted 2 X-Axis Images Output Field</i>	39
<i>Fig. 2-22: Restricted Symmetric-Y Input Field</i>	40

<i>Fig. 2-23: Restricted 1 Y-Axis Image Output Field.....</i>	<i>40</i>
<i>Fig. 2-24: Restricted 2 Y-Axis Images Output Field</i>	<i>40</i>
<i>Fig. 2-25: Restricted Symmetric-XY Input Field.....</i>	<i>41</i>
<i>Fig. 2-26: Restricted 1x1 Image Output Field.....</i>	<i>41</i>
<i>Fig. 2-27: Restricted 2x2 Images Output Field</i>	<i>41</i>
<i>Fig. 2-28: Restricted 3x3 Images Output Field</i>	<i>42</i>
<i>Fig. 2-29: Restricted Paired Excitation XY Input Field.....</i>	<i>43</i>
<i>Fig. 2-30: Restricted Paired 1st Single Image Output Field.....</i>	<i>43</i>
<i>Fig. 2-31: Restricted Paired 2x2 Images Output Field.....</i>	<i>43</i>
<i>Fig. 2-32: Restricted Paired 2nd Single Image Output Field</i>	<i>43</i>
<i>Fig. 3-1: Symm XY Input $z=0\mu\text{m}$</i>	<i>46</i>
<i>Fig. 3-2: Periodic Symm XY $z=520.7\mu\text{m}$</i>	<i>46</i>
<i>Fig. 3-3: Periodic Symm XY $z=1028.0\mu\text{m}$</i>	<i>46</i>
<i>Fig. 3-4: Periodic Symm XY $z=1508.7\mu\text{m}$</i>	<i>46</i>
<i>Fig. 3-5: Periodic Symm XY $z=2042.7\mu\text{m}$</i>	<i>46</i>
<i>Fig. 3-6: Periodic Symm XY $z=2523.4\mu\text{m}$</i>	<i>46</i>
<i>Fig. 3-7: Periodic Symm XY $z=3044.1\mu\text{m}$</i>	<i>47</i>
<i>Fig. 3-8: Periodicity POI Symm XY.....</i>	<i>48</i>
<i>Fig. 3-9: Image Resolution</i>	<i>50</i>
<i>Fig. 3-10: Approximate Resolution Matching Gaussian Input HW.....</i>	<i>52</i>
<i>Fig. 3-11: 3x3 Symmetrical Images</i>	<i>53</i>
<i>Fig. 3-12: 3x3 Symmetrical Images</i>	<i>53</i>
<i>Fig. 3-13: 3x3 Symmetrical Images</i>	<i>53</i>
<i>Fig. 3-14: 3x3 Symmetrical Images</i>	<i>53</i>
<i>Fig. 3-15: Symmetrical 12x12 Images</i>	<i>54</i>
<i>Fig. 3-16: Symmetrical 5x5 Images</i>	<i>54</i>
<i>Fig. 3-17: Symmetrical 2x2 Images</i>	<i>54</i>
<i>Fig. 3-18: Imbalance 2x2 $x + 0\mu\text{m}$</i>	<i>55</i>
<i>Fig. 3-19: Imbalance 2x2 $x + 1\mu\text{m}$</i>	<i>55</i>

<i>Fig. 3-20: Imbalance 2x2 $x + 2\mu\text{m}$</i>	55
<i>Fig. 3-21: Imbalance 2x2 $x + 2\mu\text{m}$ $y + 2\mu\text{m}$</i>	55
<i>Fig. 3-22: Symmetrical MxN Image Distance Difference</i>	57
<i>Fig. 3-23: Polarization Effect on Effective Width</i>	58
<i>Fig. 3-24: Polarization Effect on Image Distance</i>	59
<i>Fig. 3-25: Refractive Index Effect on Image Distance (n_g and n_c)</i>	60
<i>Fig. 3-26: Scalable 3DMMI Image Distances</i>	61
<i>Fig. 3-27: Symmetrical 2x2 $W_x+0\mu\text{m}$ $W_y+0\mu\text{m}$</i>	62
<i>Fig. 3-28: Symmetrical 2x2 $W_x+1\mu\text{m}$ $W_y+0\mu\text{m}$</i>	62
<i>Fig. 3-29: Symmetrical 2x2 $W_x+3\mu\text{m}$ $W_y+0\mu\text{m}$</i>	62
<i>Fig. 3-30: Symmetrical 2x2 $W_x+5\mu\text{m}$ $W_y+0\mu\text{m}$</i>	62
<i>Fig. 3-31: Symmetrical 2x2 $W_x+3\mu\text{m}$ $W_y+2\mu\text{m}$</i>	63
<i>Fig. 3-32: 3DMMI Fabrication Tolerance 3D-Mesh Plot Top View</i>	65
<i>Fig. 3-33: 3DMMI Fabrication Tolerance δL_x</i>	66
<i>Fig. 3-34: 3DMMI Fabrication Tolerance W_x</i>	67
<i>Fig. 3-35: 3DMMI Fabrication Tolerance n_{gx}</i>	67
<i>Fig. 3-36: 3DMMI Optical Bandwidth ($w_0 = 6.66\mu\text{m}$)</i>	68
<i>Fig. 4-1: Schematic of 3DMMI-2LR</i>	71
<i>Fig. 4-2: 3DMMI-2LR $3\mu\text{m}$ Unequal Layers Input</i>	72
<i>Fig. 4-3: 3DMMI-2LR $3\mu\text{m}$ Equal Layers Input</i>	72
<i>Fig. 4-4: 3DMMI-2LR $3\mu\text{m}$ Unequal Layers Output</i>	72
<i>Fig. 4-5: 3DMMI-2LR $3\mu\text{m}$ Equal Layers Output</i>	72
<i>Fig. 4-6: 3DMMI-2LR $50\mu\text{m}$ Input ($z=0\mu\text{m}$)</i>	75
<i>Fig. 4-7: 3DMMI-2LR $50\mu\text{m}$ Input to Routing Section ($z=2670\mu\text{m}$)</i>	75
<i>Fig. 4-8: 3DMMI-2LR $50\mu\text{m}$ General Interference Routed Field ($z=44476.8\mu\text{m}$)</i>	76
<i>Fig. 4-9: 3DMMI-2LR $50\mu\text{m}$ General Interference Output from Waveguide</i> ($z=47146.8\mu\text{m}$)	76
<i>Fig. 4-10: 3DMMI-2LR $50\mu\text{m}$ Symmetric-X Interference Routed Field</i>	

<i>(z=7895.85 μm, Δ_x=1)</i>	76
<i>Fig. 4-11: 3DMMI-2LR 50 μm Symmetric-X Interference Routed Field</i>	
<i>(z=13121.7 μm, Δ_x=2)</i>	76
<i>Fig. 4-12: 3DMMI-2LR 50 μm Symmetric-X Interference Output from Waveguide</i>	
<i>(z=15791.7 μm)</i>	76
<i>Fig. 5-1: Generalized 3DMMI Fabrication Process Procedures</i>	83
<i>Fig. 5-2: (a) Wavelength Absorbance of SU-8 with Given Thickness, (b) SU-8 Film Exposure Energy Requirement [Ref. 76: MicroChem SU-8 2000 Reference Sheet]</i>	
.....	84
<i>Fig. 5-3: Kopp 7380 UV Filter Wavelength Transmission [Ref. 78: Kopp Glass]</i>	
.....	84
<i>Fig. 5-4: SU-8 T-Topping with Widths (a) 50 μm, (b) 40 μm, (c) 30 μm, (d) 20 μm, (e) 10 μm</i>	86
<i>Fig. 5-5: SEM End View of SU-8 50x50 μm² Cross-Section</i>	87
<i>Fig. 5-6: The Effects of T-Topping on 50x50 μm² Waveguides (a) Without Ethylene Glycol, (b) With Ethylene Glycol</i>	87
<i>Fig. 5-7: Filled UV-15 Cladding with 50x50 μm² SU-8 Waveguides</i>	88
<i>Fig. 5-8: Top-view of SU-8 cuts (a) with UV-15 fill (b) with removable photoresist</i>	
.....	89
<i>Fig. 5-9: 3DMMI-2LR Mask Lithography Technique</i>	90
<i>Fig. 5-10: 2DMMI-2LR Section End-View(50x100 μm²)</i>	90
<i>Fig. 6-1: 3DMMI Test Equipment Layout</i>	92
<i>Fig. 6-2: Insertion Loss of SU-8 Multimode Waveguides</i>	94
<i>Fig. 6-3: Optical Confinement of SU-8 3DMMI 50x50 μm² Structures</i>	96
<i>Fig. 6-4: Symmetric-XY Self-Image 50x50 μm²</i>	97
<i>Fig. 6-5: Symmetric-XY 2x2 Images 50x50 μm²</i>	97
<i>Fig. 6-6: General 2x2 Images</i>	98
<i>Fig. 6-7: Symmetrical 3x3 Images (a) actual image (b) simulated image</i>	99

List of Abbreviations and Symbols

3D	Three Dimension(al)
3DMMI	3D Multi-Mode Interference
3DMMI-2LR	3D Multi-Mode Interference 2 Layer Routing
Al₂O₃	Aluminum Oxide
BPM	Beam Propagation Method
C	Carbon
dB	Decibel (power ratio)
dBm	Decibel (power/1mW)
DBR	Distributed Bragg Reflector
DWDM	Dense Wavelength Division Multiplexing
E	Electric Field
EIM	Effective Index Method
EL	Excess Loss
EMI	Electro-Magnetic Interference
EO	Electro-Optic
F	Fluorine
FDBPM	Finite-Difference BPM
FDTD	Finite-Difference Time-Domain
GH	Goos-Hänchen
H	Magnetic Field
HW	Half-Width
InP	Indium Phosphate
LED	Light Emitting Diode
LSF	Line Spread Function
MEMS	Micro-Electro-Mechanical Systems
MFD	Mode Field Diameter
MIPS-P	Multimode Interference Photonic Switch with Partial

	Index-modulation Region
MQW	Multiple Quantum Well
MSM	Metal Semiconductor Metal
MZI	Mach Zehnder Interferometer
O	Oxygen
PEB	Post Exposure Bake
PIN	P-doped Intrinsic N-doped
PMMA	Polymethyl-methacrylate
POF	Polymer Optical Fiber
POI	Power Overlap Integral
RC	Resistant-Capacitance
RIE	Reactive Ion Etch
SB	Soft Bake
SEED	Self-Electrooptic Effect Devices
SEM	Scanning Electron Microscope
SiO₂	Silicon Dioxide
TE	Transverse Electric
TIR	Total Internal Reflection
TM	Transverse Magnetic
UV	Ultra-Violet
VCSEL	Vertical Cavity Surface Emitting Laser
VDWDM	Very Dense Wavelength Division Multiplexing

[1] Introduction

1.1 Progress of Communication

Throughout human history, communication has been the foundation of activity including cultural exchange, trade, and survival. The word “communication” is defined in dictionaries as *the activity of conveying information, allowing access between people or places*. Today, communication is not only the exchange of information between human beings or locations, it also refers to the exchange of information in the machines, gadgets, and devices we use everyday. As technology advances, communication users continue to demand higher speed, longer distance, higher quality, and greater user-friendliness. The emergence of the optical fiber during the last two decades has satisfied some of these demands. Fiber communication has so far provided large benefits for long-distance networks mainly because of its low-loss and high bandwidth nature. For inter-device communications, such as in computer systems, optical interconnects have yet to match the density levels of electronic integrated circuits. So far, device-to-device communication via electrical wiring, copper cables, and chip-to-chip interconnects has maintained its dominance. Optical means of information exchange still lack maturity at the device level, between devices, and within devices. In recent years, consumer demand has escalated, and conductor-based paths of communication have been progressing closer to their fundamental problems.

1.2 The Electrical Bottleneck

Metal wiring has dominated the electronic world since the beginning of electronic devices because it is the medium in which electrons can be transported most efficiently. Today’s wired communication, long or short-distance, and between or

within devices, operates with these inexpensive metal interconnections. As the demand for higher speed, higher bandwidth, and higher efficiency has risen in the past decade, the performance increase of metal interconnects has been inadequate. This inadequacy will continue to escalate to a point where interconnects can no longer sustain rising device performances and user demands. This effect is known as the ‘electrical bottleneck’. Electrical interconnections’ drawbacks are becoming ever-increasingly apparent, especially when realizing that their fundamental limits are fast approaching. These drawbacks are summarized below [1]:

- power dissipation as heat,
- attenuation at high frequencies causing signal distortion,
- electrical crosstalk between parallel lines due to inherent capacitance and inductance,
- impedance mismatches causing signal reflections,
- strong signal perturbations due to external EMI,
- and bandwidth shortage dependent on the bus speed and the bus width.

As a pinnacle state-of-the-art technology, microprocessors such as the Pentium IV processor produced by Intel Corporation exhibit examples of these electronic drawbacks. Today, the Pentium IV microprocessor is capable of processing-speeds up to 3.8 GHz with 800-1066 MHz interconnect bus speeds, and with gates fabricated with the 90 nm technology [2]. Clearly, the bus speed is inferior compared to the processing speed, indicating that the bottleneck is apparent. As the processing speed of the Pentium IV increases, the number of electrical components and interconnects also increases; more prominently, these new designs will be more densely integrated. As a result, power loss, heating, signal distortion, and bandwidth shortage will all increase. In the future, devices will reach their metal interconnect limits of speed and bandwidth. For example, the communication capacity of metal interconnects is dependent on the area over the square of the length:

$$\frac{\text{bits}}{s} \propto \frac{\text{area}}{\ell^2}, \quad (1.2.1)$$

where ‘area’ is the cross-sectional area and ‘ ℓ ’ is the length of the metal wire [3]. This

relation indicates that the scale up of metal wires, in terms of three-dimensions, will not improve its capacity. In other words, performance cannot be increased by making the system bigger or smaller. To circumvent this and the above disadvantages, optical interconnects and optical means of communication are of interest. All of nature's methods have a fundamental limit of performance acceptance, but optical methods of communication promises improved performance limits compared to traditional metal wires.

1.3 Optical Communication

Optical communication using guided-wave optics originated from a demonstration of Total Internal Reflection (TIR) by John Tyndall in the late 19th Century [4]. The fundamentals of guided-wave transmission of light involve media of different index of refraction shown in Fig. 1-1. Start with Snell's Law

$$n_1 \sin(\theta_1) = n_2 \sin(\theta_2), \quad (1.3.1)$$

where n_1 and n_2 are the respective medium's index of refraction, and θ_1 is the incident angle in medium 1 while θ_2 is the refractive angle in medium 2 with respect to the perpendicular line at the boundary. By extending Snell's Law, the incident angle becomes the critical angle when the angle of refraction in medium 2 is 90° . This indicates that TIR occurs when the refractive index of the incident medium is larger than the refractive medium and the angle of incident is equal or larger than the critical angle. In this case, reflected and refracted light will remain in medium 1 indicated by the blue and green light paths while the red path is not TIR.

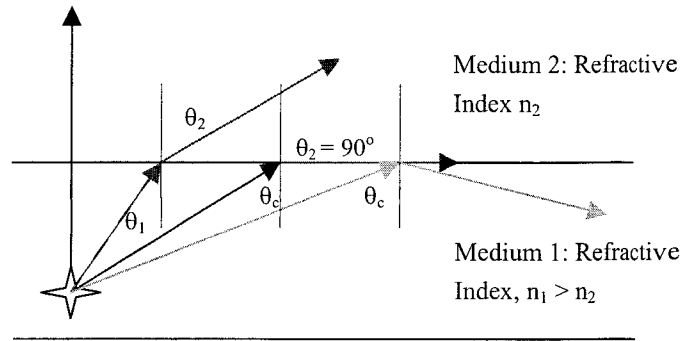


Fig. 1-1: TIR

The most commercialized communication based on TIR has been the optical fiber. In recent years, this technology has been the dominant force driving the high-speed, long/short-haul, high-bandwidth, highly efficient, and voice/data wired communication. Unlike metal wiring, optical connection capacities are less dependent on the length [3]. In addition, optical connections also offer the following advantages [1]:

- lower power dissipation,
- modulation frequency loss independence,
- very low to no signal crosstalk,
- coatings or medium perturbations to prevent reflections,
- immunity to EM interference,
- bandwidth matching to system device/component performance,
- high packing densities,
- and lower communication energy.

With these in mind, optical fiber technology prevails over all other wired technology especially looking into the future. Despite the fact that optical communication continues to develop in cities, countries, and between countries, this technology is still limited in its application in other areas of device-to-device communication. Diverging away from macro-scale optical interconnects, micro-scale optical communication is becoming an increasingly important field of research. The field of integrated optics, also part of optical communication, is developing quickly as an alternative to current electronic devices.

1.4 Integrated Optics

The idea of integrated optics was first introduced by Stewart E. Miller in 1969. In his paper, he proposed the integration of optical waveguides in silicon or semiconductor similar to the integration of electronic circuits for computing [5]. A core dielectric region embedded within a different refractive index region will guide and confine optical waves. This technology allows for a monolithic integration of various optical components in either hybrid systems with other electronic components or all-optical systems. Integrated optics permits the realization of integrated optical wiring, integrated laser resonators, electro-optic (EO) modulators, frequency-selective filters, couplers, power splitters, and many other devices. In terms of couplers and splitters, various directional couplers, circular couplers, and y-splitters have been realized to permit precise power transfer between waveguides with various input and output ports [4].

In the past decade, researchers have realized the importance of integrated optical devices not only for computing, but also for improving various other devices that required metal connections [6]. In order to replace metal wiring, it is essential to integrate optical components involving a transmitter of light, an optical interconnect, and a receiver of the transmitted signal. The basic goal of all integrated optics designers may involve their work on one of the three areas or EO components for translations between optical and electrical systems.

In the optical sources area, abundant research work has been done on Light Emitting Diodes (LED), Vertical Cavity Surface Emitting Lasers (VCSEL), Multiple Quantum Well (MQW) emitters, and Distributed Bragg Reflector (DBR) emitters. On the optical receiver side, researchers have been interested in P-doped Intrinsic N-doped (PIN) semiconductor photodiodes, avalanche photodiodes, Metal-Semiconductor-Metal (MSM) detectors, and quantum well detectors such as MQW devices. Another area of consideration is the modulation and demodulation of optical signals using various devices such as the Mach-Zehnder Interferometer (MZI) modulator and Self-Electrooptic Effect Devices (SEED) [7]. In order to accommodate

large increases in the number of ports for input or output, two-dimensional arrays of the devices above have been introduced, especially arrayed VCSEL, MQW, and SEED. Many of these arrayed devices promise to serve the demand for increased bandwidth and channels of communication for future interconnects and computing systems.

As part of the transport system for optical signals, couplers and splitters are also very important devices. One of the focuses in this area for researchers is the Multi-Mode Interference (MMI) device, where a mode is one possible electro-magnetic field solution profile of the propagating wave equation described in Chapter 2. This type of device can efficiently split, couple, and route optical signals with an arbitrary number of input and output ports permitting flexible designs and results.

1.5 The MMI

The fundamentals of MMI stem from John Talbot's Effect, published in 1836, which is the interference of multiple modes forming self-images [8]. In 1992, the first MMI planar optical coupler was proposed by Lucas Soldano and his colleagues as shown in Fig. 1-2(b) [9]. Unlike conventional couplers shown in Fig. 1-2(a), the coupling region was increased in width.

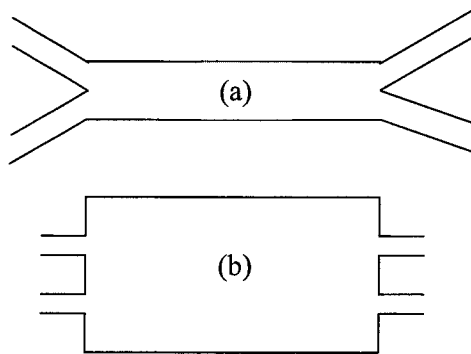


Fig. 1-2: (a) Conventional 2-Mode Interference (b) 2x2 MMI Coupler

Based in a $\text{SiO}_2\text{-Al}_2\text{O}_3\text{-SiO}_2$ cladding-core-cladding material setup on a substrate of silicon, the designed lengths of the coupler allowed realization of self-images with minimized excess or insertion losses. The researchers concluded that their work would prompt further developments of M inputs by N outputs MMI couplers for integrated optoelectronic circuit networks and efficient waveguide switches.

One year later, Ferreras et al. [10] demonstrated a 1xN splitter/combiner based on InP with a 24 μm width and varied lengths around 300 μm . They successfully illustrated the ability for a single input to be split into four outputs with self-imaging multimode interference equations. As colleagues of Soldano, Pennings and his group reported additional properties of MMI devices in a paper in 1994 [11]. In their study, MMI transmissions were categorized into three types: MxN general self-imaging, 2xN restricted self-imaging, and 1xN symmetric power splitting. A thorough investigation of transmission, back-reflection, and internal resonance was conducted with 2x2 3dB couplers and 1x2 power splitters. One year later in 1995, Soldano and Pennings [12] joined resources and published a review of MMI principles based on self-imaging. In addition, applications of MMI devices were proposed for coherent receiver front-ends, ring lasers, and MZI structures, which were demonstrated in a Ph. D. thesis from N. S. Lagali [13] in 2000 at the University of Alberta.

In 1999, Heaton and Jenkins [14] analyzed MMI couplers with the General Matrix Theory of self-imaging for predicting the imaging properties of an 11x11 non-uniform MMI coupler. Around the same time, significant research interests were focused on tapered MMI couplers to reduce real estate on a substrate. Levy et al. [15-16] first demonstrated a tapered MMI mid-section resulting in symmetry on both sides of the central region. These researchers conducted the study on a 2x2 MMI coupler with an investigation into splitting ratios and transmissions due to a normalized width variation for both straight and parabolic tapers. In another study conducted by Wei et al. [17-18], the reduced length or size advantage of tapered MMI couplers was realized. In contrast, Z. Wu and K. Utaka have demonstrated insertion-loss imbalance between input ports can be improved through increasing the device length of their horn-shaped MMI combiner [19]. Fig. 1-3 illustrates a general

tapered MMI coupler.

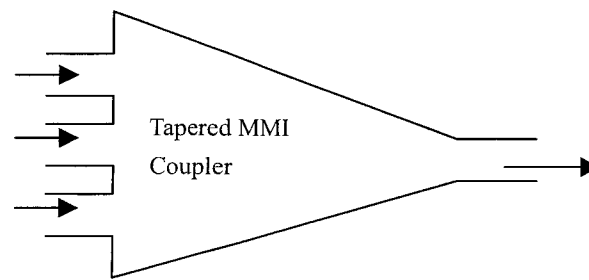


Fig. 1-3: General Tapered MMI Coupler

In 2001, Leuthold and Joyner [20] reported tunable power splitting with MMI couplers. They showed that with proper design of internal dimensions, symmetrical and asymmetrical power splitting ratios could be achieved for $M \times N$ MMI coupler structures. In 2002, Japanese researcher Nagai in K. Utaka's group [21] demonstrated the implementation of a photonic switch using MMI with 1×2 and 2×2 structures at varying current injections. Various power splitting, loss, crosstalk, and efficiency properties were studied with these two fabricated devices. In 2005, Utaka published a review of semiconductor MMI waveguides including Multimode Interference Photonic Switch with Partial Index-modulation Region (MIPS-P) illustrated by Fig. 1-4, and Michelson Interferometer-type Wavelength Converter with Multi-mode Interference Coupler (MIWC-MMIC) [22]. Fig. 1-4 below depicts one possible schematic of the implemented partial index modulation regions to shift the output of the MMI device. Today, MMI couplers are being adapted for fields such as astronomy where a magic T function (sum of two inputs at one output port and difference of two inputs at the other output port) can be realized with the collection of out-of-phase outputs from self-imaging [23], thus resulting in wide bandwidths for stellar interferometers. In addition, MMI couplers are also being implemented for optical temperature sensors [24]. Details of the MMI and self-imaging effects can be understood in Chapter 2.

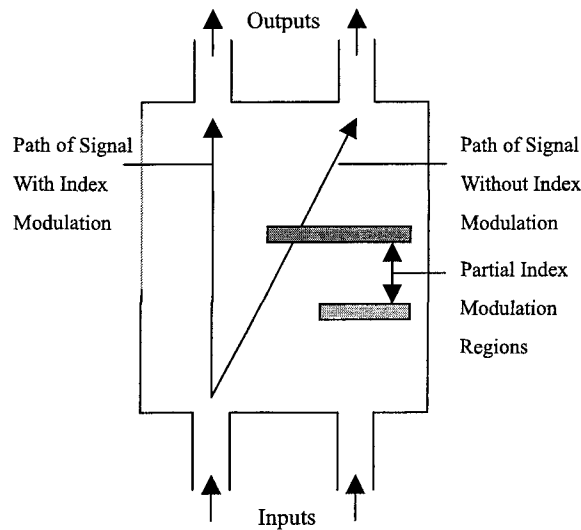


Fig. 1-4: General Schematic of MIP-S

1.6 Two Dimensional Imaging

So far, imaging in MMI devices has been realized in one dimension. In order to accommodate for a greater number of inputs and outputs, in-plane dimensions must be increased dramatically. As modern devices scale to increase density, their in-plane real estates are becoming increasingly scarce. The introduction of three-dimensional MMI (3DMMI) devices will reduce this difficulty and will allow for coupling between a number of novel 3D photonic devices such as photonic crystal-based [25] waveguides or an array of light emitters and detectors. Initially, two-level extensions of optical waveguides can be realized with fabrication technologies such as shadow or grayscale mask Reactive Ion Etching (RIE) and partial exposure photolithography [26-27]. In 1999, Garner et al. demonstrated the ability for vertical splitting of single-mode fields using a three-dimensional waveguide structure fabricated in polymers. This type of design can be illustrated by Fig. 1-5. Recently, Jiang et al. reported the analysis of two-level dielectric waveguides using the Finite-Difference Time-Domain (FDTD) method [28]. For this design, power loss has a strong dependence on the length and angle of a diagonally connected waveguide.

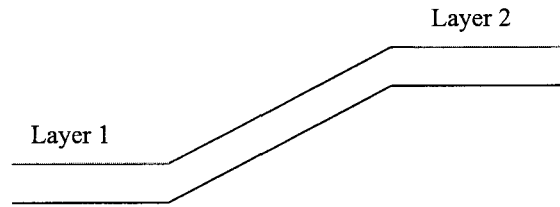


Fig. 1-5: 3D Waveguide Side View

There are also issues with the application of the cladding material and structural integrity issues. For 3DMMI devices, there is no need for sharp corners and bend angles since multimode self-imaging will naturally extend itself into the other plane levels.

1.7 Thesis Objective

In order to allow for a confinement of multiple modes in the vertical direction, the vertical depth of a MMI coupler must be increased. So far, general MMI devices have been fabricated using the planar technology with mainly semiconductor materials. Recently, two groups, He et al. [29] as well as Khalil and Yehia [30] have demonstrated the principles of 3DMMI by introducing a vertical extension of a bulk-waveguide. The difference in this type of design in contrast to the MMI design is that more than one mode can be supported in the vertical direction simply with a larger physical height. Thus, one single mode input at any cross-sectional input location will produce interference imaging in two-dimensions. Interestingly, this idea may be traced back to self-imaging in microwave waveguides developed years ago [31]. A schematic representation of the multiple self-imaging simulations reported in Ref. 30 is shown in Fig. 1-6.

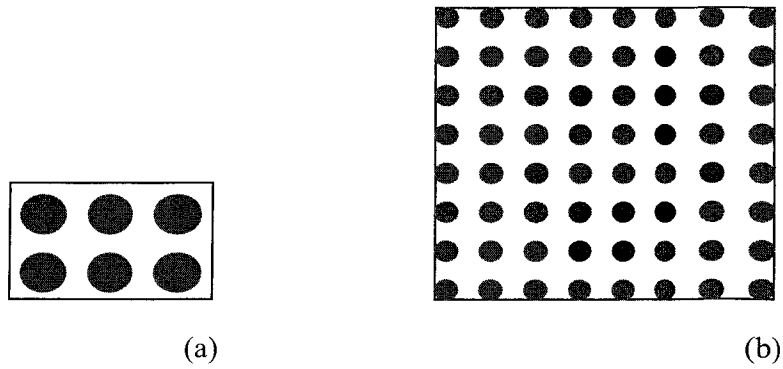


Fig. 1-6: (a) Two Dimensional 6 Images (b) Two Dimensional 64 Images

In this example, $20 \times 30 \mu\text{m}^2$ and $160 \times 160 \mu\text{m}^2$ waveguide cross-sections can be used to simulate 3×2 and 8×8 output images with a central input at the wavelength of 1550 nm. The examples cited above are simulations and there remains a need to fabricate and test devices to demonstrate the practicality of 3DMMI. This dissertation reviews and develops the theory of general MMI and MMI in the 3D sense. 3DMMI work in this study includes:

- 3DMMI $1 \times N$ splitters,
- 3DMMI self-imaging,
- 3DMMI cross-axis imaging,
- 3DMMI image mirroring,
- 3DMMI tolerances of design parameters,
- and 3DMMI 2-Layer Routing.

For simplicity, this thesis includes the fabrication and imaging of self-imaging and multiple imaging with polymers because they are known to have excellent adhesion to a number of surfaces, low loss, ease of fabrication, stability, and precise control of optical characteristics [32]. The fabrication and testing of 3D devices are still difficult with today's technology where microfabrication has solely been based on layer-by-layer methods and optical coupling has relied on the alignment of bare optical fiber. Nonetheless, 3DMMI structures can be fabricated and they can be characterized to reflect the theoretical understanding.

1.8 Thesis Organization

The organization of this thesis is described here. Chapter 2 presents the general rectangular waveguide theory, MMI modal propagation analysis, general imaging of 2D MMI or general MMI, and 3DMMI imaging listed in section 1.7 of this chapter. Chapter 2 also includes Simulation of theory completed with Optiwave Beam Propagation Methods (BPM) and Matlab. Chapter 3 describes in detail the tolerances of designs and problems from the behavior of real devices compared to the ideal. Chapter 4 presents the advantages of 3DMMI, its applications, and design of two-layer routing of optical signals. Chapter 5 explains the fabrication process of the 3DMMI devices including material investigation, process optimization, and results of varying process parameters. Specific details from Chapters 2-5 involving numerical analysis and fabrication method are included in the Appendix. Chapter 6 then demonstrates the behavior of the fabricated 3DMMI devices. The summary of this thesis is then given in Chapter 7 along with a discussion of the development of future devices based on 3DMMI.

[2] 3DMMI Theory and Simulation

2.1 Introduction

This chapter begins with the general theory of optical waveguides, which describes the transverse confinement of EM waves. MMI theory is then derived from the propagation of multiple modes within these waveguides. Three-dimensional MMI, extended from two-dimensional MMI, allows signal routing into multiple layers. There are various routing behaviors within a 3DMMI device making it flexible and pertinent to a wide diversity of applications. Two powerful simulation programs, Matlab and Optiwave BPM, assist in the verification of the above theories and designs. Matlab allows for the numerical analysis of designs and theories while Optiwave BPM generates cross-sectional interference images at an arbitrary distance along the waveguide when varying important parameters.

2.2 Optical Waveguide Theory

2.2.1 Planar Waveguides

Unlike electrical conduction, optical waves travel in a waveguide as distinct optical modes. In simple terms, an optical mode is a spatial energy distribution in one or more dimensions. The most basic optical waveguide is the planar waveguide, which hosts these optical modes. The planar waveguide is characterized by parallel planar boundaries with a finite gap, d , shown in Fig. 2-1. The parallel boundaries exist with three media with respective indices of refraction n_1 , n_2 , and n_3 . In addition, the planar boundaries extend to infinity in the x and z directions, which is impossible for real devices. However, this type of structure forms the basis for analyzing real waveguides of rectangular cross section [33].

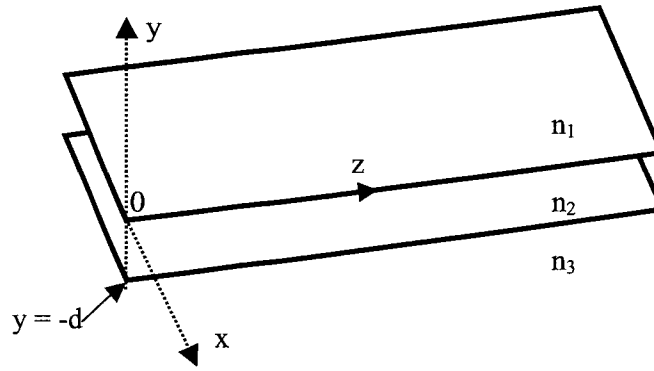


Fig. 2-1: Planar Optical Waveguide

Consider the planar waveguide cross section in the y-z plane shown below:

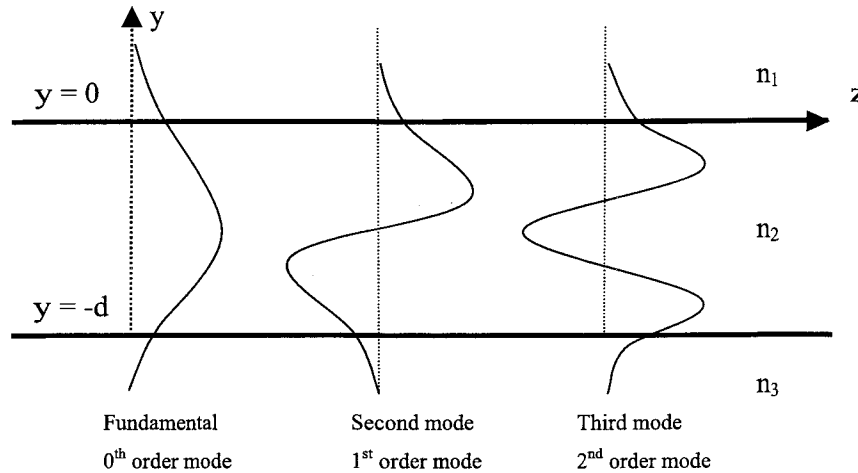


Fig. 2-2: Planar Waveguide Modes

Fig. 2-2 depicts the lowest three optical modes and they can be found as electric field amplitude solutions of Maxwell's wave equation [34-35]:

$$\nabla^2 \vec{E}(\vec{r}, t) = \frac{n^2(\vec{r})}{c^2} \times \frac{\partial^2 \vec{E}(\vec{r}, t)}{\partial t^2}, \quad (2.2.1)$$

where \vec{E} is the electric field vector, \vec{r} is the radius vector, n is the refractive index, c is the speed in a vacuum, and t is the time. Based on Snell's Law and TIR, reflections will occur at $y = 0$ and $y = -d$. This boundary condition simplifies Eq. 2.2.1 for Transverse Electric (TE) plane waves (fields with x directional components only) traveling in the z direction with solutions of the form

$$E_x(y, z, t) = E_x(y) e^{i(\alpha y - \beta z)}, \quad (2.2.2)$$

where ω is the radial frequency and β is the propagation constant in the z direction. The $E_x(y)$ function has the general form

$$E_x(y) = \begin{cases} A \exp(-qy) & 0 \leq y \leq \infty \\ B \cos(hy) + C \sin(hy) & -d \leq y \leq 0 \\ D \exp[p(y+d)] & -\infty \leq y \leq -d \end{cases}, \quad (2.2.3)$$

where A , B , C , D , h , p , and q are constants determined by boundary conditions with continuity of E_x and $\partial E_x / \partial y$, which is part of the magnetic field component H_z .

There are a number of real solutions to Eq. 2.2.3 bounded by $-d \leq y \leq 0$ and they represent each individual mode. This means that $E_x(y, z, t)$, β , and all of its constants from Eq. 2.2.3 are specific for each individual mode. From Fig. 2-2, define region 1 as the cladding, region 2 as the core, and region 3 as the substrate by assuming $n_2 > n_3 > n_1$. Guided modes will exist when $k_3 < \beta < k_2$ for each mode, where k_3 and k_2 are $n_3\omega/c$ and $n_2\omega/c$ respectively. By satisfying this guided mode condition, evanescent decaying fields will exist in region 1 and 3. If this condition is not satisfied, then sinusoidal fields with real power will exist in these two regions as radiation modes with strong power attenuation. The above solutions to Maxwell's wave equation are linear TE modes but linear Transverse Magnetic (TM) modes also exist having only transverse H_x components.

2.2.2 Rectangular Dielectric Waveguide

Solutions to Maxwell's wave equation for rectangular waveguides were developed by Marcatili [36] and Goell [37] and many others from Bell Laboratories in the 1960s. Guided modes exist in planar waveguides when the index of refraction is larger in the core region than the cladding and substrate regions. Practical integrated optical waveguides can be generally represented by rectangular waveguides where the index of refraction of the inner core must be larger than in the surrounding regions. In general, a central core region, with index n_1 and widths of W_x and W_y in the x and y directions respectively, is surrounded by reflective boundary regions with lower

refractive indices n_2 , n_3 , n_4 , and n_5 shown in Fig. 2-3.

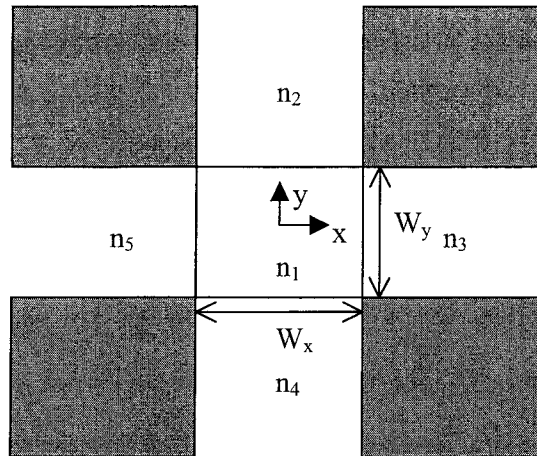


Fig. 2-3: General Rectangular Dielectric Waveguide

Regions 3 and 5 may be extended in the x direction while regions 2 and 4 may be extended in the y direction without affecting the guided modes in region 1. The four shaded regions in Fig. 2-3 indicate the boundaries at the corners of the core region and can be neglected to obtain an approximate solution to Maxwell's wave equation. In addition, these neglected regions may have the same index of refraction as their adjacent regions forming different types of integrated waveguides. In Marcatili's paper, the focus of the analysis was on the wavenumber k in the x and y directions. In Goell's paper, emphasis was set on the cylindrical coordinates of the field solutions. In his case, Bessel functions were involved for the radial approach, which allowed the analysis to include energy in the corner regions depicted as the shaded region in Fig. 2-3. The Marcatili approach is less involved and is accurate but Goell's approach improves accuracy and is much more involved [38]. Nonetheless, these guided mode profiles are similar to planar waveguide modes where approximate evanescent fields extend out of the boundaries between the cladding and the core shown in Fig. 2-2.

For two-dimensional MMI structures, the guide mode region must be wide enough in the x direction to host multiple modes of the order m starting from 0. In the y direction, the height of the propagating region must be low enough in order not to excite higher order modes beyond the fundamental. In other words, energy excitation in the y direction must be restricted to the fundamental mode. The electric field solution is thus restricted to a one-dimensional component only. For

three-dimensional MMI structures, guided modes are approximately represented by a two-dimensional mode number (m,n), where m and n are the mode numbers for the transverse components of E in the x and y directions respectively. The electric field for each individual two-dimensional mode is dependent on the field in both the x and y directions. As an approximation in the first order, the x and y dependence of each modal field can be treated by separation of variables where the two-dimensional electric field is

$$E_{mn}(x, y) \approx E_m(x)E_n(y). \quad (2.2.4)$$

Thus, the E_{00} mode represents the presence of fundamental modes in both the x and y directions while E_{01} represents the 1st order mode seen in the y direction and 0th mode in the x direction, and so on. Since the vertical direction of the guided wave region hosts multiple modes, MMI can occur in both the x and y directions.

The field profile of a guided light signal can be represented as a linear combination of all mode fields extending up to the highest possible wavelength at the highest possible mode number. With the understanding of waveguide modes and rectangular waveguides, the focus will now turn to the MMI theory.

2.3 MMI Theory

2.3.1 Modal Propagation Analysis

In the presence of multiple modes of propagation, the overall spatial field or field profile is the field sum of all permissible modes. Let an input field entering a waveguide with width W_x at $z = 0$ be $\Psi(x,0)$, omitting time dependence. This initial field may compose all possible guided modes of the waveguide (excluding unguided modes such as radiation modes):

$$\Psi(x,0) = \sum_{m=0}^{\nu-1} c_m \psi_m(x), \quad (2.3.1)$$

where $\psi_m(x)$ is the individual modal field distribution, electric or magnetic, ν is the

total number of guided modes, m is the modal number in the x direction, and c_m is the field excitation coefficient for each mode:

$$c_m = \frac{\int \Psi(x,0) \psi_m(x) dx}{\sqrt{\int |\psi_m(x)|^2 dx}}. \quad (2.3.2)$$

The above overlap integral determines the amount of excitation to each individual mode by the input field, where the modal excitation coefficient c_m cannot exceed unity. Despite the fact that Eq. 2.3.1 does not include radiation modes, this type of approximation will be accurate for real applications. The total field of Eq. 2.3.1 can then be extended to any position z along the waveguide:

$$\Psi(x, z) = \sum_{m=0}^{v-1} c_m \psi_m(x) e^{-j\beta_m z}, \quad (2.3.3)$$

where β_m is the propagation constant or the wavenumber in the z direction. These equations are the basis for the modal propagation analysis (MPA) of MMI waveguides. This method is only valid in situations where the physical properties of the waveguide do not change significantly with z . MPA and simulation methods such as BPM help to analyze the behavior of MMI devices.

2.3.2 Propagation Constants and the Effective Width

Consider a ridged MMI waveguide depicted in Fig. 2-4 where the indices of the guide and cladding are n_{guide} and n_{clad} respectively. The guide must be wide enough to host multiple modes. The analysis of the general two-dimensional field problem can be simplified to a one-dimensional problem using the Effective Index Method (EIM) [39]. This method is especially effective for ridge waveguides. First, regions I, II, and III are analyzed as individual planar waveguides. Independently solving planar waveguide equations, effective indices n_c and n_g can be obtained. The planar waveguide based on these effective indices can be treated as a one-dimensional problem in obtaining the field profile in the x direction. These effective indices are to

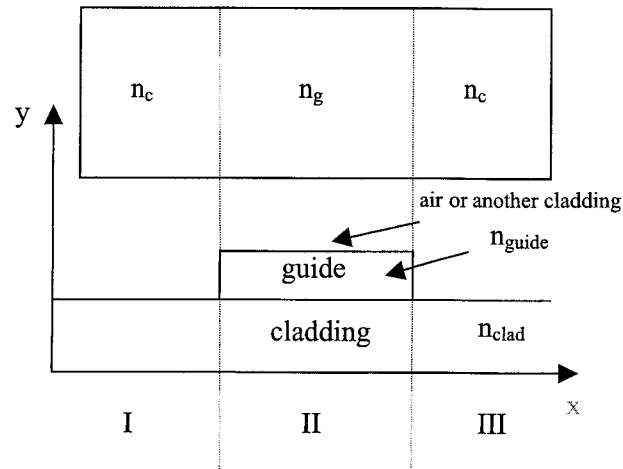


Fig. 2-4: Effective Index Method

be used for the analysis of modal propagation in the z direction. By definition, the dispersion equation relates β_m (propagation constant in the z direction), k_{xm} (lateral wavenumber), and $k_0 = 2\pi/\lambda_0$ (the wavenumber in freespace):

$$k_0^2 n_g^2 = k_{xm}^2 + \beta_m^2, \quad (2.3.4)$$

where m indicates an individual constant for each mode.

For practical applications, the lateral penetration depth of the evanescent fields into the cladding can be interpreted as the Goos-Hänchen (GH) shift [40] of optical ray reflection points into the cladding region depicted by Fig. 2-5. Thus, an effective width can be defined as the addition of the penetration depths d_1 , d_2 , and the physical width.

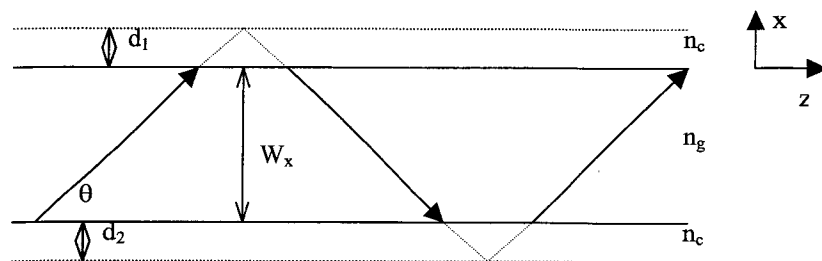


Fig. 2-5: Goos-Hänchen Shifts

This effective width W_{xeff} can be determined from the fundamental mode for simplification [40] as

$$W_{xeff} = W_x + d_1 + d_2 = W_x + \left(\frac{\lambda_0}{\pi} \right) \left(\frac{n_c}{n_g} \right)^{2\varepsilon} \frac{1}{\sqrt{n_g^2 - n_c^2}}, \quad (2.3.5)$$

where $\varepsilon = 0$ for TE modes, $\varepsilon = 1$ for TM modes, and total cladding penetration determined by the GH shift analysis. For well-confined waveguides, the penetration depth is small and is dependent on polarization. With this effective width, the k_{xm} term within the waveguide from equation 2.3.4 can be approximated by

$$k_{xm} = \frac{\pi(m+1)}{W_{xeff}}. \quad (2.3.6)$$

Combining Eq. 2.3.4 and Eq. 2.3.6, the propagation constant β_m can be obtained as approximately

$$\beta_m \cong k_0 n_g - \frac{\pi \lambda_0 (m+1)^2}{4 n_g W_{xeff}^2} \quad (2.3.7)$$

by taking a limited binomial expansion $[(x+1)^{1/2} \approx 1 + x/2$ when $|x| \ll 1$] knowing that $k_{xm}^2 \ll k_0^2 n_g^2$. For modal interference, define a beat length L_π between the lowest-order modes as

$$L_\pi = \frac{\pi}{\beta_0 - \beta_1} \cong \frac{4 n_g W_{xeff}^2}{3 \lambda_0}. \quad (2.3.8)$$

The beat length is defined here as the length at which the input phase difference between two modes becomes π .

2.3.3 MMI Imaging

From Eq. 2.3.3, the phase of the fundamental mode is a common factor and can be removed to form

$$\Psi(x, z) = \sum_{m=0}^{v-1} c_m \psi_m(x) e^{j(\beta_0 - \beta_m)z} = \sum_{m=0}^{v-1} c_m \psi_m(x) Q_m(z), \quad (2.3.9)$$

where

$$\beta_0 - \beta_m \cong \frac{m(m+2)\pi}{3L_\pi} \quad (2.3.10)$$

is derived from Eq. 2.3.7 and Eq. 2.3.8. For an actual imaging length, z is replaced with the imaging distance L . Then Q_m can be given by

$$Q_m(L) = \exp\left[j \frac{m(m+2)\pi}{3L_\pi} L\right]. \quad (2.3.11)$$

The above phase factor is fundamentally important for determining the behavior of MMI designs in terms of single, multiple, asymmetric, symmetric, and paired-imaging. From the perspective of the field profile at a distance L , the image will include reproductions of the original input. Excitation of all modes is known as *General Interference* whereas *Restricted Interference* refers to exciting certain modes only. The following observations are valuable for the understanding of MMI imaging:

$$m(m+2) = \begin{cases} \text{even} & \text{for } m \text{ even} \\ \text{odd} & \text{for } m \text{ odd} \end{cases} \quad (2.3.12a)$$

$$\psi_m(-x) = \begin{cases} \psi_m(x) & \text{for } m \text{ even} \\ -\psi_m(x) & \text{for } m \text{ odd} \end{cases}. \quad (2.3.12b)$$

Single Images

Single images are simply replicas of the original image. From Eqs. 2.3.11, 2.3.12a, and 2.3.12b, the imaging length for single images is an integer multiple of $3L_\pi$. Thus, single images occur when $Q_m = \pm 1$. A self-image, is formed when Q_m is positive for all modes. This occurs when the integer multiple of $3L_\pi$ is even. A cross-image, or x-axis mirror image, is formed when Q_m alternates with $(-1)^m$. Following Eq. 2.3.12, odd integer multiples of $3L_\pi$ produces mirrored images. The results are given in the following table:

Phase Factor Q_m	General Image Type	Imaging Distance
1	Self-Image (Bar-Coupler)	$L = p(3L_\pi) \rightarrow p = 0, 2, 4, \dots$
$(-1)^m$	Mirror-Image (Cross-Coupler)	$L = p(3L_\pi) \rightarrow p = 1, 3, 5, \dots$

Table 2-1: General Interference Single Images

Multiple Images

For MMI, certain lengths between consecutive self and mirror images are also of great interest. These lengths and their multiples are locations where multiple images appear. Using a periodic extension of the input field [41], an analysis can be performed to find that the multiple images distance exist

$$L = \frac{p}{N}(3L_\pi), \quad (2.3.13)$$

where $N \geq 1$ and $p \geq 0$ and they do not have common divisors. The field obtained has replicas of the original input given by

$$\Psi(x, L) = \frac{1}{C} \sum_{q=0}^{N-1} \Psi_{in}(x - x_q) \exp(j\phi_q), \quad (2.3.14)$$

where the positions of the replicas are located at

$$x_q = p(2q - N) \frac{W_{xeff}}{N} \quad (q = 1, \dots, N). \quad (2.3.15)$$

The phases of the q^{th} replica is

$$\phi_q = p(N - q) \frac{q\pi}{N} \quad (2.3.16)$$

and its amplitude is divided by $|C| = \sqrt{N}$ from the original. This result shows precisely the distance of multiple images located at each x_q with phase ϕ_q at equal amplitudes of $1/\sqrt{N}$. In addition, multiple input and output port devices in forms of $M \times N$ can be realized with this outcome. Fig. 2-6 illustrates a simulated MMI field pattern for general interference.

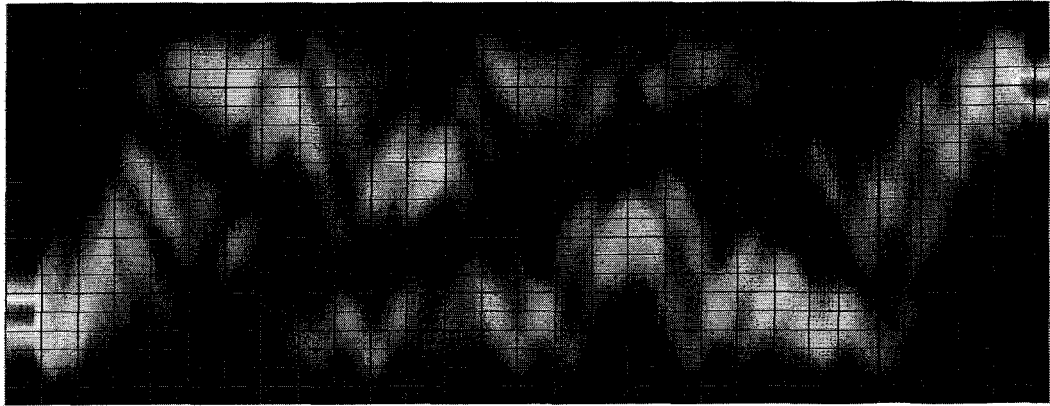


Fig. 2-6: General Interference Imaging

Paired Interference

Since there is a factor of 3 in the denominator within the exponential of Q (Eq. 2.3.11), taking the modulus of $m(m+2)$ with 3 gives 0 when m is not 2, 5, 8, At specific input positions knowing the zero-crossings of the approximate sinusoidal modes shown by Fig. 2-2, c_m will be zero when the $m = 2, 5, 8, \dots$ modes are not excited. Thus, by eliminating these modes, the factor 3 in the denominator within the exponential of Q_m can also be eliminated. The single images can then be obtained at

$$L = p(L_\pi) \quad \text{with } p = 0, 1, 2, \dots, \quad (2.3.17)$$

and multiple images at

$$L = \frac{p}{N}(L_\pi), \quad (2.3.18)$$

with $N \geq 1$ and $p \geq 0$ when they do not have common divisors. Note that the lengths above are simply 1/3 that of general interference lengths. The trick for paired excitation is to eliminate the unwanted modes. An evenly symmetric input such as a Gaussian beam around $x = \pm W_{\text{eff}}/6$ with $x = 0$ at the center of the waveguide, for example, will allow overlap integrals to cancel the symmetric and the asymmetric fields eliminating these unwanted modes. When these modes are eliminated, remaining modes will pair themselves (0-1, 3-4, 6-7, ...) with the even mode leading each paired odd mode by $\pi/2$ at the multiple-image length and π at the mirror-image length. This is known as paired interference. If only one input is present, the resultant images can vary between self-image, cross-image, or split images. The effect of two inputs will be a linear combination of the resultant images from its respective input.

Symmetric Interference

By exciting only the even modes, a multiple image splitter can be 4 times as short as general interference devices. This is exactly the result of symmetrical interference. The input field must be positioned at the center of the waveguide. The modulus of $m(m+2)$ with 4 is 0 for even modes; this reduces length periodicity by 4 given that c_m is zero for all odd modes. The lengths for single imaging and multiple imaging are

$$L = p \left(\frac{3L_\pi}{4} \right) \quad \text{with } p = 0, 1, 2, \dots \quad \text{and} \quad (2.3.19)$$

$$L = \left(\frac{p}{N} \right) \left(\frac{3L_\pi}{4} \right) \quad (2.3.20)$$

respectively. The symmetric images occur equally spaced along the x-axis with $W_{x\text{eff}}/N$. Symmetric interference image length is 4 times less than the general-imaging distance. Fig. 2-7 illustrates a simulated MMI field pattern for symmetric interference imaging. It is important to note that well-formed multiple images of 2, 3, 4, ... occur at shorter distances compared to the self-image.

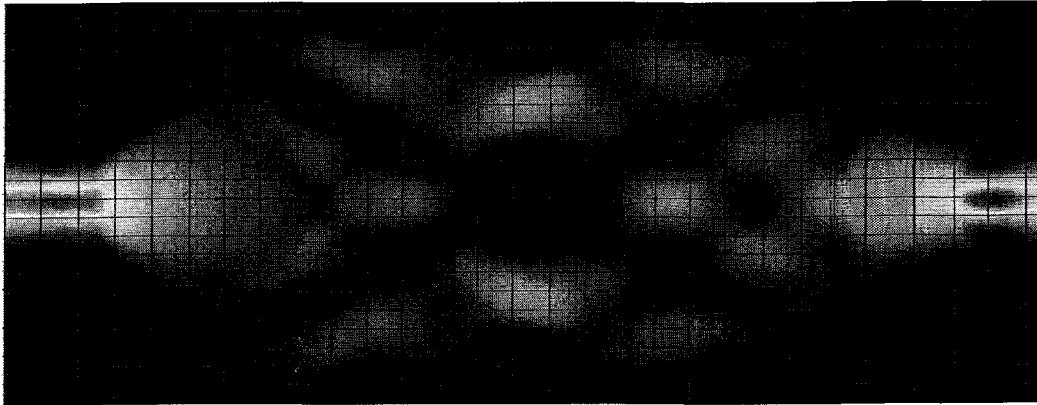


Fig. 2-7: Restricted Symmetric Interference Imaging

Some authors describe MMI as a one-dimensional interference of EM waves. Although the vertical y direction is omitted in the derivation, the theory does include variable imaging in the z direction. Thus, MMI devices should be described as a two-dimensional interference device.

2.4 3DMMI Imaging

2.4.1 3DMMI Modal Propagation Analysis

Another approach to the three-dimensional waveguide shown in Fig. 1-5 is to introduce another dimension in the MMI device. With a three-dimensional MMI,

optical images can exist in more than one planar layer. Little work has been done on 3DMMI, but the idea is a direct extension of the two-dimensional case. A three-dimensional rectangular waveguide is illustrated in Fig. 2-8.

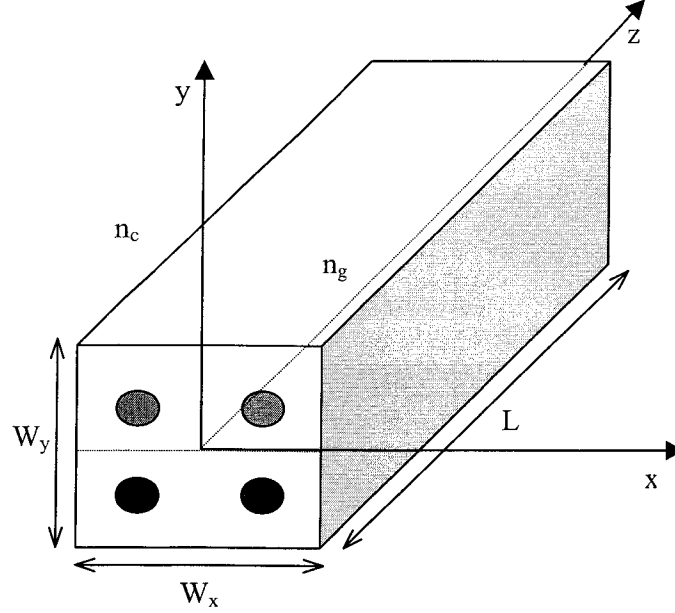


Fig. 2-8: 3DMMI Rectangular Waveguide

Assume a guide index of n_g and a cladding index around the guide of n_c . The widths of the guide in x and y are W_x and W_y respectively and the length is L . The center of the x - y - z axes from Fig. 2-8 is located at the center of the waveguide.

Because of the extra dimension y , Eq. 2.3.1 is extended to the following:

$$\Psi(x, y, 0) = \sum_{n=0}^{\kappa-1} \sum_{m=0}^{\nu-1} c_{mn} \psi_{mn}(x, y), \quad (2.4.1)$$

where n is the mode number in the y direction, κ is the maximum number of modes in the y direction, ψ_{mn} is the (m,n) two-dimensional mode field, and c_{mn} is the mode coefficient found from the total input field as

$$c_{mn} = \frac{\int_{-\infty}^{\infty} \int_{-\infty}^{\infty} \Psi(x, y, 0) \psi_{mn}^*(x, y) dx dy}{\int_{-\infty}^{\infty} \int_{-\infty}^{\infty} |\psi_{mn}(x, y)|^2 dx dy}. \quad (2.4.2)$$

Similar to Eq. 2.3.9 and removing the time dependence and phase of the fundamental mode as before, the following equation can be obtained for the mode field at distance

z:

$$\Psi(x, y, z) = \sum_{n=0}^{\kappa-1} \sum_{m=0}^{\nu-1} c_{mn} \psi_{mn}(x, y) \exp[-j(\beta_{mn} - \beta_{00})z], \quad (2.4.3)$$

where β_{mn} is the propagation constant of the (m,n) two-dimensional order mode and β_{00} is the propagation constant of the fundamental mode.

2.4.2 3DMMI Propagation Constants and the Effective Widths

For the three-dimensional case, the dispersion equation 2.3.4 must be extended to

$$k_0^2 n_g^2 = k_{xm}^2 + k_{yn}^2 + \beta_{mn}^2, \quad (2.4.4)$$

where k_{yn} is the wavenumber of respective n modes in the y direction. Allowing for the GH shifts, the effective width $W_{y\text{eff}}$ in the y direction can also be determined as

$$W_{y\text{eff}} = W_y + \left(\frac{\lambda_0}{\pi} \right) \left(\frac{n_c}{n_g} \right)^{2\varepsilon} \frac{1}{\sqrt{n_g^2 - n_c^2}}, \quad (2.4.5)$$

where $\varepsilon = 0$ for TE modes, and $\varepsilon = 1$ for TM modes. The effective width $W_{x\text{eff}}$ in the x direction is the same from Eq. 2.3.5 and the expansion factor after the physical width is also the same. With this effective width, the k_{yn} term within the waveguide from Eq. 2.4.4 can be approximated by

$$k_{yn} = \frac{\pi(n+1)}{W_{y\text{eff}}}, \quad (2.4.6)$$

and k_{xm} is the same as in Eq. 2.3.6. From the above relation, it can be shown that the propagation constant β_{mn} can be obtained from Eq. 2.4.4 as approximately

$$\beta_{mn} \cong k_0 n_g \left(1 - \frac{1}{2} \left[\left(\frac{\lambda_0(m+1)}{2n_g W_{x\text{eff}}} \right)^2 + \left(\frac{\lambda_0(n+1)}{2n_g W_{y\text{eff}}} \right)^2 \right] \right) \quad (2.4.7)$$

by taking a limited binomial expansion $[(x+1)^{1/2} \approx 1 + x/2 \text{ when } |x| \ll 1]$ knowing that k_{xm}^2 and $k_{yn}^2 \ll k_0^2 n_g^2$. For interference, the beat lengths in the x and y directions can be determined from the two lowest-order modes as:

$$L_{x\pi} = \frac{\pi}{\beta_{00} - \beta_{10}} \cong \frac{4n_g W_{xeff}^2}{3\lambda_0} \quad \text{and} \quad (2.4.8)$$

$$L_{y\pi} = \frac{\pi}{\beta_{00} - \beta_{01}} \cong \frac{4n_g W_{yeff}^2}{3\lambda_0} \quad (2.4.9)$$

respectively where β_{10} and β_{01} are the propagation constants of the second modes in the x and y directions respectively.

2.4.3 3DMMI Imaging Equations

Substituting Eq. 2.4.7 into Eq. 2.4.3, a new three-dimensional variable phase factor Q_{m3d} can be obtained:

$$Q_{m3d} = \exp\left[j \frac{m(m+2)\pi}{3L_{x\pi}} L\right] \exp\left[j \frac{n(n+2)\pi}{3L_{y\pi}} L\right]. \quad (2.4.10)$$

This new phase factor is the fundamental quantity for determining the behavior of 3DMMI designs. In this case, for imaging to occur, both beat conditions in Q_{m3d} must be met simultaneously. With Eq. 2.4.10, general and restricted interferences will result in three dimensions.

General Interference: Self-Imaging

A self-image is a direct replica of the original input at the same physical location in the cross-sectional area but at a distance L. The quantity of Eq. 2.4.10 must be unity for any type of input that excites all modes. In this case, there are four quadrants of input but self-imaging can occur with an input at any location. By equating Q_{m3d} to unity, the distance L can be found to be the following:

$$L = 6\Delta_x L_{x\pi} = 6\Delta_y L_{y\pi} \quad (2.4.11)$$

with

$$\frac{W_{xeff}}{W_{yeff}} = \sqrt{\frac{\Delta_y}{\Delta_x}}, \quad (2.4.12)$$

where Δ_x and Δ_y are any positive integers.

General Interference: Mirror-Imaging

In a two-dimensional cross-sectional plane, mirror imaging can occur across the x-axis, y-axis, or both.

1. Mirror Across X-axis

In this case, the first beating condition of Q_{m3d} is unity for all m and the second condition can be either -1 when n is odd or 1 when n is even. The result is the following:

$$L = 6\Delta_x L_{x\pi} = 3\Delta_y L_{y\pi} \quad \text{and} \quad (2.4.13)$$

$$\frac{W_{xeff}}{W_{yeff}} = \sqrt{\frac{\Delta_y}{2\Delta_x}}, \quad (2.4.14)$$

where Δ_y must be odd. In this case, mirroring cannot be achieved with a square cross-sectional waveguide. The width ratio in the x and y directions can be calculated using Eq. 2.4.14.

2. Mirror Across Y-axis

Similar to mirroring across the x-axis, this type of mirroring occurs when the second beating condition of Q_{m3d} is unity for all n and the first condition can be either -1 when m is odd or 1 when m is even. The imaging lengths satisfy the following:

$$L = 3\Delta_x L_{x\pi} = 6\Delta_y L_{y\pi} \quad \text{and} \quad (2.4.15)$$

$$\frac{W_{xeff}}{W_{yeff}} = \sqrt{\frac{2\Delta_y}{\Delta_x}}, \quad (2.4.16)$$

where Δ_x must be odd. Again, mirroring here cannot be achieved with a square cross-sectional waveguide and the width ratio in the x and y directions can be calculated using Eq. 2.4.16.

3. Mirror Across both Y and X Axes (Cross Imaging)

Trivially, a cross image is formed when both beating conditions are -1 forming

unity. In this case, the beating conditions will restrict the imaging lengths to be the following:

$$L = 3\Delta_x L_{x\pi} = 3\Delta_y L_{y\pi} \quad \text{and} \quad (2.4.17)$$

$$\frac{W_{xeff}}{W_{yeff}} = \sqrt{\frac{\Delta_y}{\Delta_x}}, \quad (2.4.18)$$

where both Δ_x and Δ_y must be odd to avoid overlapping with the self-images. Notice that the width ratio in Eq. 2.4.18 is the same as in the case of self-imaging. Similar to that of two-dimensional MMI behavior, a cross-image for 3DMMI occurs at a distance before self-images.

General Interference: Multiple-Imaging

The analysis of multiple imaging is again similar to two-dimensional MMI. It can be shown that the length is of the following:

$$L = \frac{3\Delta_x L_{x\pi}}{N_x} = \frac{3\Delta_y L_{y\pi}}{N_y}, \quad (2.4.19)$$

where similar to two-dimensional MMI analysis, Δ_x or Δ_y cannot have common divisors with the positive integers N_x and N_y respectively. In addition, Δ_x or Δ_y must be odd integers to avoid self-image lengths. The above length allows for N_x number of images in the x direction and N_y number of images in the y direction of the waveguide. From Eq. 2.4.13, the following relation must be satisfied:

$$\frac{W_{xeff}}{W_{yeff}} = \sqrt{\frac{\Delta_y N_x}{\Delta_x N_y}}, \quad (2.4.20)$$

with both x and both y subscripts at different levels (numerator and denominator). Similar to two-dimensional MMI, it can also be shown that lateral distance between the centers of individual images is W_{xeff}/N_x or W_{yeff}/N_y and the distance between the centers of edge images to the edge of the effective width is $W_{xeff}/2N_x$ or $W_{yeff}/2N_y$. In simple terms, images both in the x and y directions are equally spaced in the effective width dimensions.

Restricted Interference: Paired Excitation

Similar to the two-dimensional MMI case, inputs can be located symmetrically around $\pm W_{x\text{eff}}/6$, $\pm W_{y\text{eff}}/6$, or a position with both such x and y terms. The basic idea again is to eliminate the excitation of certain modes to reduce the imaging length. If a single input is present, there are possibilities of self-image, cross-image, and split-images. If two inputs are present, the result is the linear combination of their respective images. For a symmetrical input around $\pm W_{x\text{eff}}/6$, the image length is the following:

$$L = \frac{\Delta_x L_{x\pi}}{N_x}. \quad (2.4.21)$$

For a symmetrical input around $\pm W_{y\text{eff}}/6$, the length is the following:

$$L = \frac{\Delta_y L_{y\pi}}{N_y}. \quad (2.4.22)$$

For a symmetrical input around a position with one x and one y term above such as at $+W_{x\text{eff}}/6$ and $+W_{y\text{eff}}/6$, the length is the following:

$$L = \frac{\Delta_x L_{x\pi}}{N_x} = \frac{\Delta_y L_{y\pi}}{N_y}. \quad (2.4.23)$$

In all three above cases, similar to before, Δ_x or Δ_y cannot have common divisors with the positive integers N_x and N_y respectively if there are multiple images.

From a previous analysis, at the specific location of the paired excitation symmetric around $\frac{b_x W_{x\text{eff}}}{N_x}$, $\frac{b_y W_{y\text{eff}}}{N_y}$, or both from the edge of the waveguide, there will be image overlapping [42]. The factor b_x or b_y is an integer between 1 and the number of images overlapping to form the final image. In the case of 1x2 two-dimensional MMI, non-uniform power splitting ratio of the two outputs could become 15:85 or 28:72 instead of 50:50. An increased number of inputs will result in an increased number of overlapping images if positioned near these specific locations. For the purpose of this thesis, this idea will be omitted to focus on uniform power distributions.

Restricted Interference: Symmetrical Excitation

Symmetrical interference can occur with the input symmetric to the x, y, and both axes. Symmetry about the x-axis means the input is symmetrical around $x=0$. Symmetry about the y-axis means the input must be symmetrical around $y=0$. By eliminating odd modes, the imaging length can be reduced similar to two-dimensional MMI. For symmetry about the x-axis only, the image length is

$$L = \frac{3\Delta_x L_{x\pi}}{4N_x}. \quad (2.4.24)$$

Similarly, for symmetry about the y-axis only, the image length is

$$L = \frac{3\Delta_y L_{y\pi}}{4N_y}. \quad (2.4.25)$$

Lastly, for the symmetry about both axes, the image length is

$$L = \frac{3\Delta_x L_{x\pi}}{4N_x} = \frac{3\Delta_y L_{y\pi}}{4N_y}, \quad (2.4.26)$$

which means that the effective widths must be chosen as

$$\frac{W_{xeff}}{W_{yeff}} = \sqrt{\frac{\Delta_y N_x}{\Delta_x N_y}}. \quad (2.4.20)$$

For this case, the input is situated at the symmetrical center of the waveguide cross-section.

Now with 3DMMI theory and length equations explained, they will be simulated for verification in the next section. To summarize the theory of 3DMMI, Table 2-2 reviews all of the length equations:

Imaging Type	Image Location	Restrictions
General: Self	$L = 6\Delta_x L_{x\pi} = 6\Delta_y L_{y\pi}$	$\frac{W_{xeff}}{W_{yeff}} = \sqrt{\frac{\Delta_y}{\Delta_x}}$
General: Mirror-X	$L = 6\Delta_x L_{x\pi} = 3\Delta_y L_{y\pi}$	$\frac{W_{xeff}}{W_{yeff}} = \sqrt{\frac{\Delta_y}{2\Delta_x}} \quad \Delta_y \in \text{odd}$
General: Mirror-Y	$L = 3\Delta_x L_{x\pi} = 6\Delta_y L_{y\pi}$	$\frac{W_{xeff}}{W_{yeff}} = \sqrt{\frac{2\Delta_y}{\Delta_x}} \quad \Delta_x \in \text{odd}$
General: Mirror X-Y	$L = 3\Delta_x L_{x\pi} = 3\Delta_y L_{y\pi}$	$\frac{W_{xeff}}{W_{yeff}} = \sqrt{\frac{\Delta_y}{\Delta_x}} \quad \Delta_x \& \Delta_y \in \text{odd}$
General: Multiple	$L = \frac{3\Delta_x L_{x\pi}}{N_x} = \frac{3\Delta_y L_{y\pi}}{N_y}$	$\frac{W_{xeff}}{W_{yeff}} = \sqrt{\frac{\Delta_y N_x}{\Delta_x N_y}} \quad \Delta_x \& N_x \in \text{n.c.d.}^1$ $\Delta_y \& N_y \in \text{n.c.d.}$
Paired: $\pm W_{xeff}/6$	$L = \frac{\Delta_x L_{x\pi}}{N_x}$	Input around $\pm W_{xeff}/6$
Paired: $\pm W_{yeff}/6$	$L = \frac{\Delta_y L_{y\pi}}{N_y}$	Input around $\pm W_{yeff}/6$
Paired: X&Y	$L = \frac{\Delta_x L_{x\pi}}{N_x} = \frac{\Delta_y L_{y\pi}}{N_y}$	Input around the combination of $\pm W_{xeff}/6$ and $\pm W_{yeff}/6$
Symmetric: X	$L = \frac{3\Delta_x L_{x\pi}}{4N_x}$	Input around $x=0$
Symmetric: Y	$L = \frac{3\Delta_y L_{y\pi}}{4N_y}$	Input around $y=0$
Symmetric: X-Y	$L = \frac{3\Delta_x L_{x\pi}}{4N_x} = \frac{3\Delta_y L_{y\pi}}{4N_y}$	$\frac{W_{xeff}}{W_{yeff}} = \sqrt{\frac{\Delta_y N_x}{\Delta_x N_y}} \quad \text{Input at } (0,0)$

1 - no common divisor

Table 2-2: Summary of 3DMMI Image Lengths

2.5 3DMMI Simulation

2.5.1 Simulation Tools and Conditions

The validity of the 3DMMI theory was verified with two software packages: Matlab and Beam Propagation Method (BPM) by Optiwave [43]. The Matlab program allows for calculation and verification of theoretical image lengths. This program also allows for the determination of variables within the imaging equations. All of the documented codes of Matlab can be found in Appendix A. The BPM software is a graphical tool for the design and simulation of various rectangular waveguide structures with a number of variable simulation parameters. This program is based on the Finite-Difference BPM (FDBPM) with Full-Vector, Semi-Vector, Scalar, and the Alternating Direction Implicit scheme algorithms [43]. For verifying 3DMMI theory, the following parameters and general conditions were used in the BPM simulations:

- $W_x = W_y = 30\mu\text{m}$
- Gaussian Input (Amplitude = 1)
- $n_g = 1.585, n_c = 1.52$
- $\lambda_0 = 1550\text{nm}$
- Average Reference Index
- Semi-Vector Algorithm
- TE Polarization (relative to x)
- Number of x and y points in mesh = 200

2.5.2 Initial Simulation

Matlab was first used to determine the theoretical values of image lengths with determined effective widths. Next, the BPM program was utilized to simulate and to verify the types of imaging achievable with 3DMMI. Each type of imaging was verified individually with a comparison of theoretical and simulated image lengths.

The wavelength was chosen to be 1550 nm, which is in one of the important bands of wavelengths for fiber communication. The refractive indices were chosen to be $n_g = 1.585$ and $n_c = 1.52$, which were similar to the materials used later for fabrication. Since imaging lengths are strongly dependent on width, $30 \mu\text{m} \times 30 \mu\text{m}$ was chosen to minimize the simulation image length L required by BPM. The highest and lowest field amplitude is illustrated in red and blue respectively in all simulated images. Simulation run-times typically depend on the length of the waveguide and the number of cross-sectional view planes. These times could range from 5min to 3 hours.

General: Self-Image

In this case, a simple square waveguide was used with an input at the center of the top left quadrant as depicted in Fig. 2-9. In this case, the effective widths in the x and y directions were the same, thus both beat lengths were also equal. The shortest imaging length occurred when $\Delta_x = 1$, or the first possible image distance.

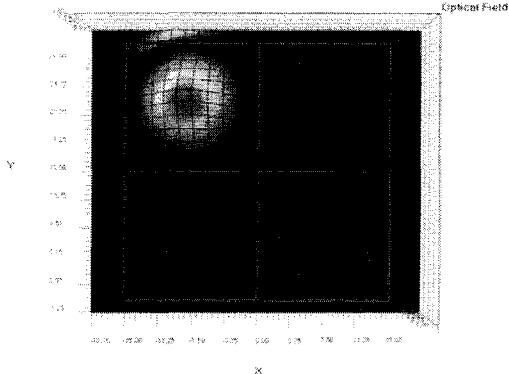
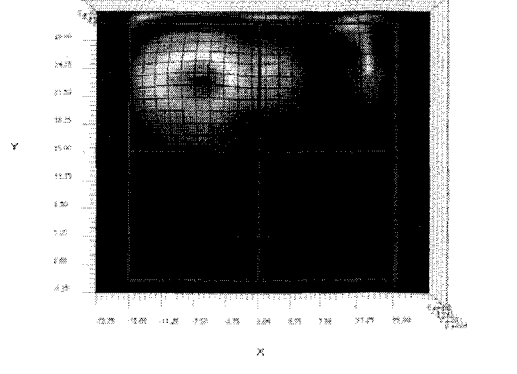
Self-Image	
Theoretical Length:	7911.5 μm
Simulation Length:	7935.9 μm
Input Field:	Output Field:
 <p style="text-align: center;"><i>Fig. 2-9: General Self-Image Input Field</i></p>	 <p style="text-align: center;"><i>Fig. 2-10: General Self-Image Output Field</i></p>

Table 2-3: Simulation of General Interference Self-Image

General: Mirror X-Y Image

Again, a simple square waveguide was used with an input at the center of the top left quadrant depicted in Fig. 2-11. In this case, the effective widths in the x and y directions were the same, thus both beat lengths were also equal. The shortest imaging length occurred when $\Delta_x = 1$.

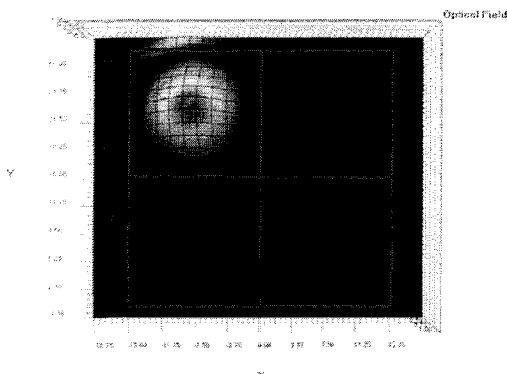
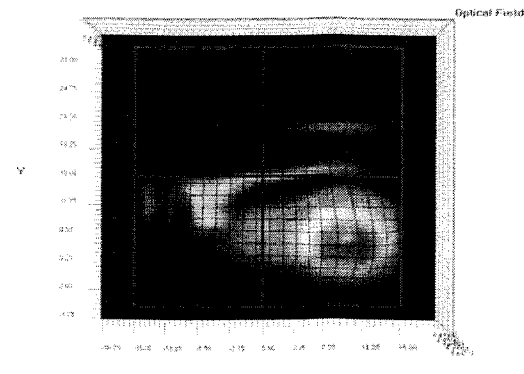
Mirror X-Y Image	
Theoretical Length:	3955.8 μm
Simulation Length:	3947.9 μm
Input Field:	Output Field:
 <p><i>Fig. 2-11: General Mirror X-Y Input Field</i></p>	 <p><i>Fig. 2-12: General Mirror X-Y Output Field</i></p>

Table 2-4: Simulation of General Interference Mirror X-Y Image

General: Multiple Images

The same square waveguide was used with an input at the center of the top left quadrant depicted in Fig. 2-13. In this case, the effective widths in the x and y directions were the same, thus both beat lengths were also equal. The shortest imaging length occurred when $\Delta_x = 1$ with $N_x = 2$, or 2 images in the x and y directions.

Multiple Images	
Theoretical Length:	1977.9 μm
Simulation Length:	2014.0 μm
Input Field:	Output Field:

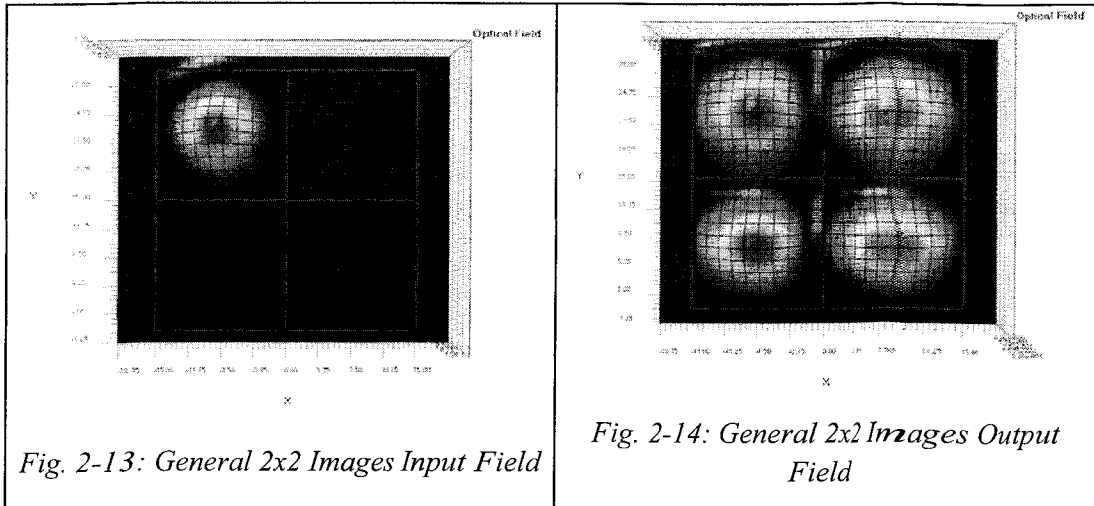


Fig. 2-13: General 2x2 Images Input Field

Fig. 2-14: General 2x2 Images Output Field

Table 2-5: Simulation of General Interference 2x2 Images

General: Mirror-X Image

For this type of image, Eq. 2.4.14 does not permit a square dimensional waveguide. From this equation, if the effective widths are equal, Δ_y cannot be odd. This violates the condition that Δ_y must be odd for mirror-x imaging. For simplicity, let $\Delta_x = 1$ and $\Delta_y = 1$ and 3. With these conditions, $W_{x\text{eff}}$ can be determined if $W_{y\text{eff}}$ is known from $W_y = 30 \mu\text{m}$. The ratio of $W_{x\text{eff}}/W_{y\text{eff}}$ can be $\sqrt{\frac{1}{2}}$ and $\sqrt{\frac{3}{2}}$ which gives $W_x = 20.9 \mu\text{m}$ and $37.0 \mu\text{m}$ respectively. The effective width ratio is, of course, not restricted to the above two values. The simulation of mirroring with respect to the x-axis using $W_x = 20.9 \mu\text{m}$ is illustrated below:

Mirror-X Image	
Theoretical Length ($W_x = 20.9 \mu\text{m}$):	3955.8 μm
Simulation Length ($W_x = 20.9 \mu\text{m}$):	4058.12 μm
Input Field:	Output Field:

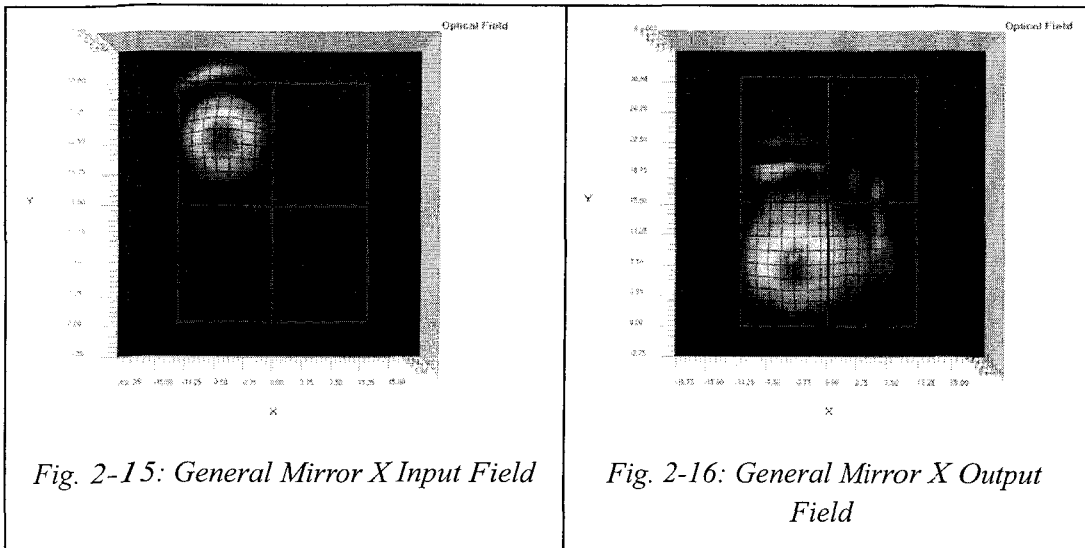


Fig. 2-15: General Mirror X Input Field

Fig. 2-16: General Mirror X Output Field

Table 2-6: Simulation of General Interference Mirror X Image

General: Mirror-Y Image

For this type of image, again, a square waveguide cannot be used. If the effective widths are equal, Δ_x cannot be odd, as indicated in Table 2-2. The condition that Δ_x must be odd for mirror-y imaging would be violated. For simplicity, let $\Delta_x = 1$ and $\Delta_y = 1$. With these conditions, $W_{x\text{eff}}$ can be determined if $W_{y\text{eff}}$ is known from $W_y = 30 \mu\text{m}$. The ratio of $W_{x\text{eff}}/W_{y\text{eff}}$ can be $\sqrt{\frac{2}{1}}$ and $\sqrt{\frac{2}{3}}$ which gives $W_x = 42.9 \mu\text{m}$ and $24.3 \mu\text{m}$ respectively. The effective width ratio is again, of course, not restricted to the above two values. Surprisingly, the imaging lengths for both $W_x = 42.9 \mu\text{m}$ and $24.3 \mu\text{m}$ are the same. Thus, the simulation of mirroring with respect to the y-axis using $W_x = 24.3 \mu\text{m}$ is illustrated below:

Mirror-Y Image	
Theoretical Length ($W_x = 24.3 \mu\text{m}$):	7911.5 μm
Simulation Length ($W_x = 24.3 \mu\text{m}$):	8016.0 μm
Input Field:	Output Field:

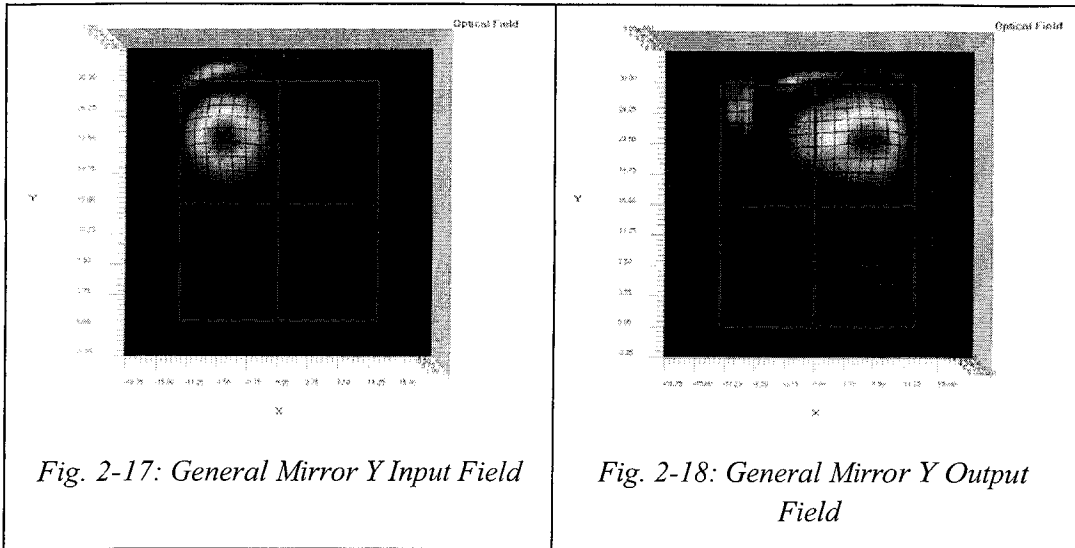


Table 2-7: Simulation of General Interference Mirror Y Image

Restricted: Symmetric-X Image

With an input symmetric to the x-axis, multiple images can form as well as its self-image. The important conclusion from the corresponding image equation in Table 2-2 is that only images in the x direction can be determined. Thus, the equation does not predict the number or appearance of images in the y direction. The input was located at $x = 0 \mu\text{m}$ and $y = 8 \mu\text{m}$ according to Fig. 2-8. The shortest imaging length occurred when $\Delta_x = 1$ with $N_x = 1$ and $N_x = 2$.

Symmetric-X Image	
Theoretical Length (1 Image):	989.0 μm
Theoretical Length (2 Images):	494.5 μm
Simulation Length (1 Image):	988.0 μm
Simulation Length (2 Images):	494.5 μm
Input Field:	Output Field:

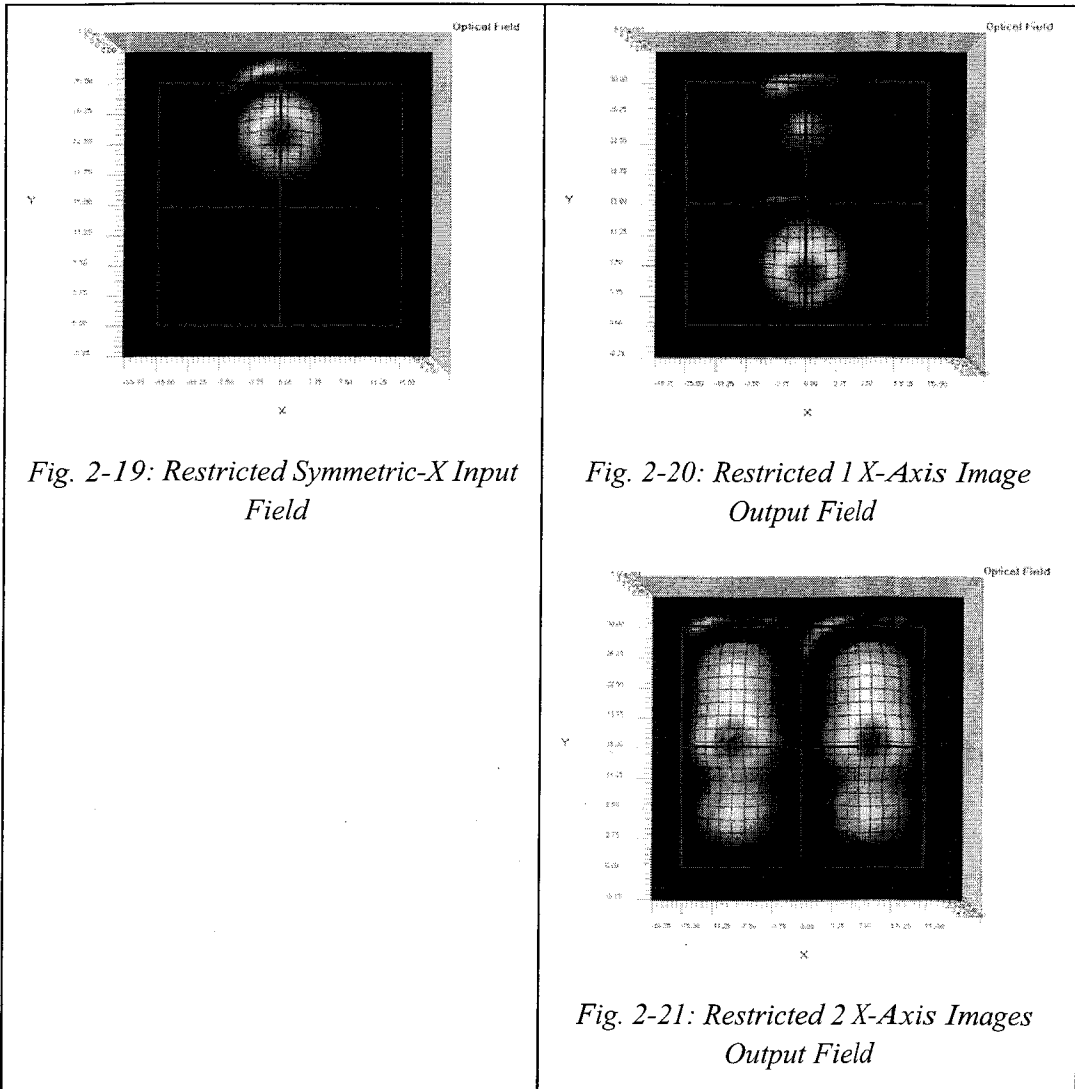


Table 2-8: Simulation of Restricted Interference Symmetric-X Image

Restricted: Symmetric-Y Image

Again, the length equation for this case predicts only the number of images in the y direction. Thus, the equation does not predict the number of images in the x direction. The input was located at $x = 8 \mu\text{m}$ and $y = 0 \mu\text{m}$ according to Fig. 2-8. The shortest imaging length occurred when $\Delta_x = 1$ with $N_y = 1$ and $N_y = 2$.

Symmetric-Y Image
Theoretical length and simulation lengths are identical from that of Symmetric-X Images

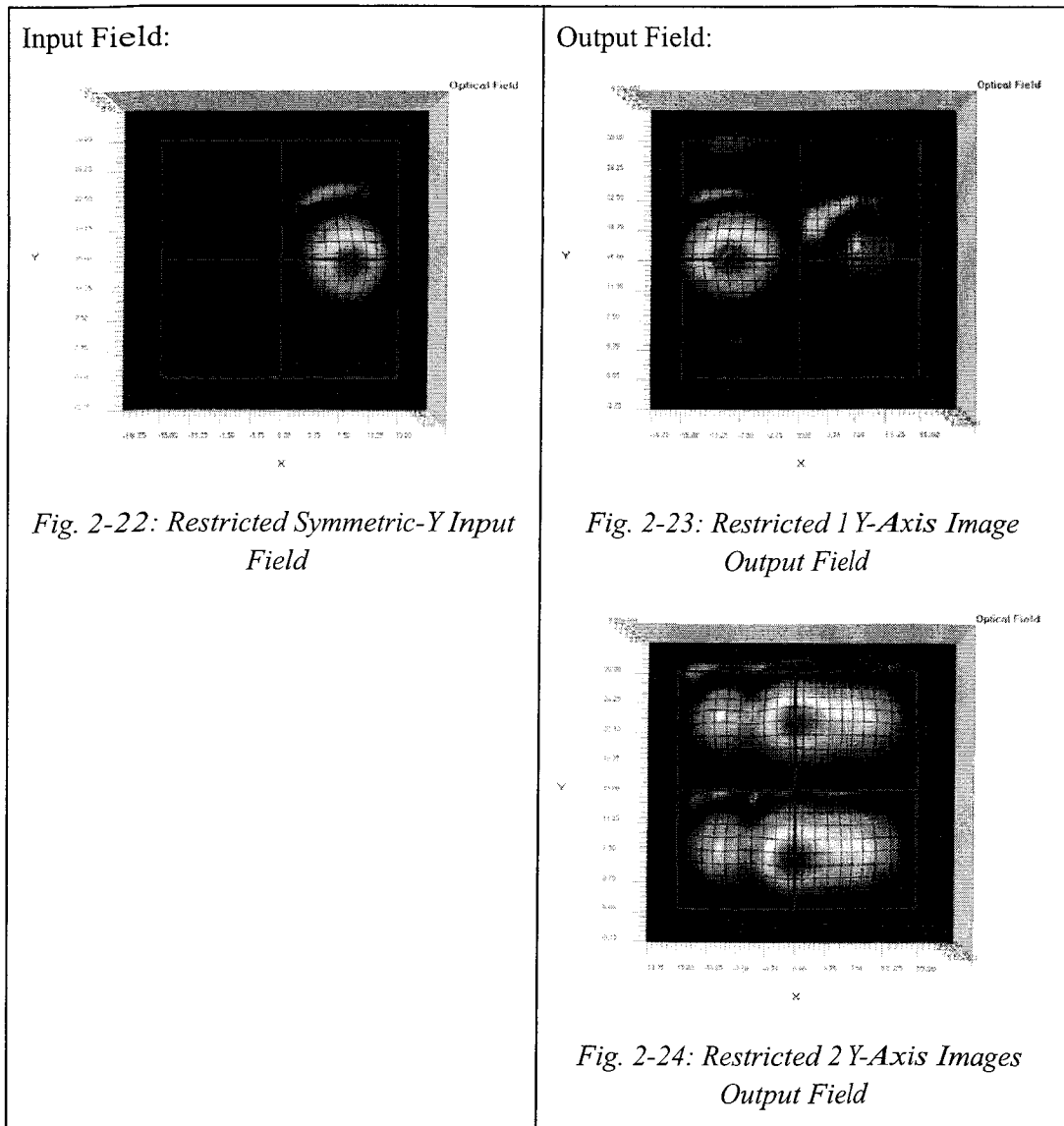
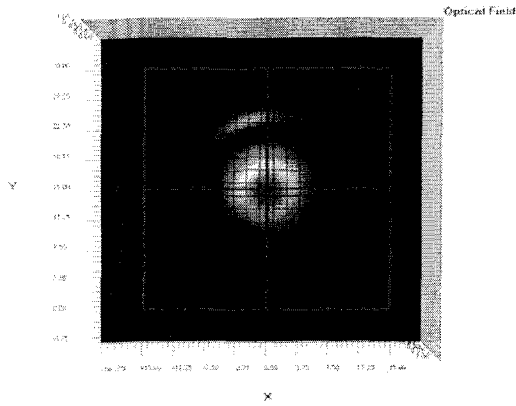
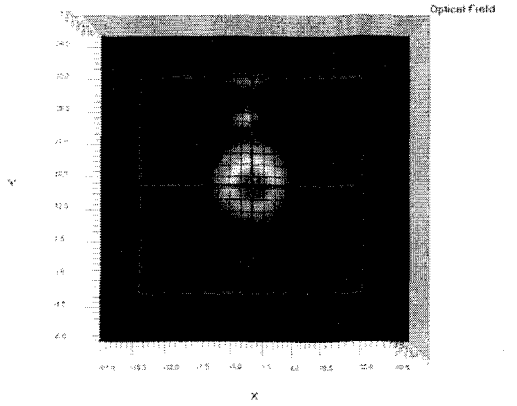
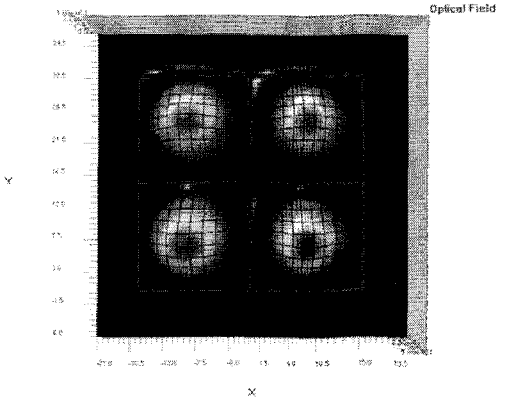


Table 2-9: Simulation of Restricted Interference Symmetric-Y Image

Restricted: Symmetric-XY Image

The input for this type of imaging technique can only exist at the physical center of the waveguide input cross-section. By utilizing total x-y symmetry, images form more symmetrically throughout z and best preserve the Gaussian nature of the input. A central input meant that it was located at $x = 0 \mu\text{m}$ and $y = 0 \mu\text{m}$ according to Fig. 2-8. The shortest imaging length occurred when $\Delta_x = \Delta_y = 1$ with 1x1, 2x2, and 3x2 images.

Symmetric-XY Image	
Theoretical Length (1 Image):	989.0 μm
Theoretical Length (2x2 Images):	494.5 μm
Theoretical Length (3x3 Images):	330.0 μm
Simulation Length (1 Image):	1028.0 μm
Simulation Length (2x2 Images):	520.7 μm
Simulation Length (3x3 Images):	333.8 μm
Input Field:	Output Field:
	
<i>Fig. 2-25: Restricted Symmetric-XY Input Field</i>	<i>Fig. 2-26: Restricted 1x1 Image Output Field</i>
	
	<i>Fig. 2-27: Restricted 2x2 Images Output Field</i>

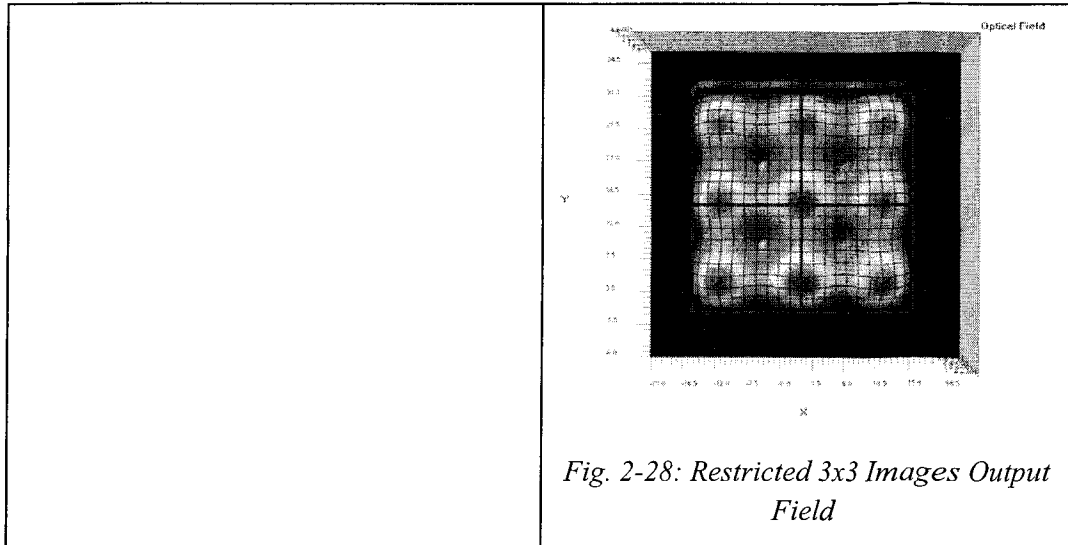


Table 2-10: Simulation of Restricted Interference Symmetric-XY Image

Restricted: Paired Interference XY

Since paired interference with a symmetrical input strictly around $\pm W_{\text{eff}}/6$ or $\pm W_{\text{yeff}}/6$ produces similar results, an input symmetric about both an x and y value is the most interesting for 3DMMI. Let the input be at $x = +W_{\text{eff}}/6 \mu\text{m}$ and $y = +W_{\text{yeff}}/6 \mu\text{m}$ according to Fig. 2-8. In this case, both x and y direction images can be predicted. The input was limited with a half-width of $3 \mu\text{m}$ rather than $5 \mu\text{m}$ to minimize output image overlapping. The shortest imaging length occurred when $\Delta_x = 1$ with $N_x = 1, 2$ and $\Delta_x = 2$.

Paired Interference XY Image	
Theoretical Length (1 st Single Image):	1318.6 μm
Theoretical Length (2x2 Images):	659.3 μm
Theoretical Length (2 nd Single Image):	2637.2 μm
Simulation Length (1 st Single Image):	1364.6 μm
Simulation Length (2x2 Images):	682.3 μm
Simulation Length (2 nd Single Image):	2689.0 μm
Input Field:	Output Field:

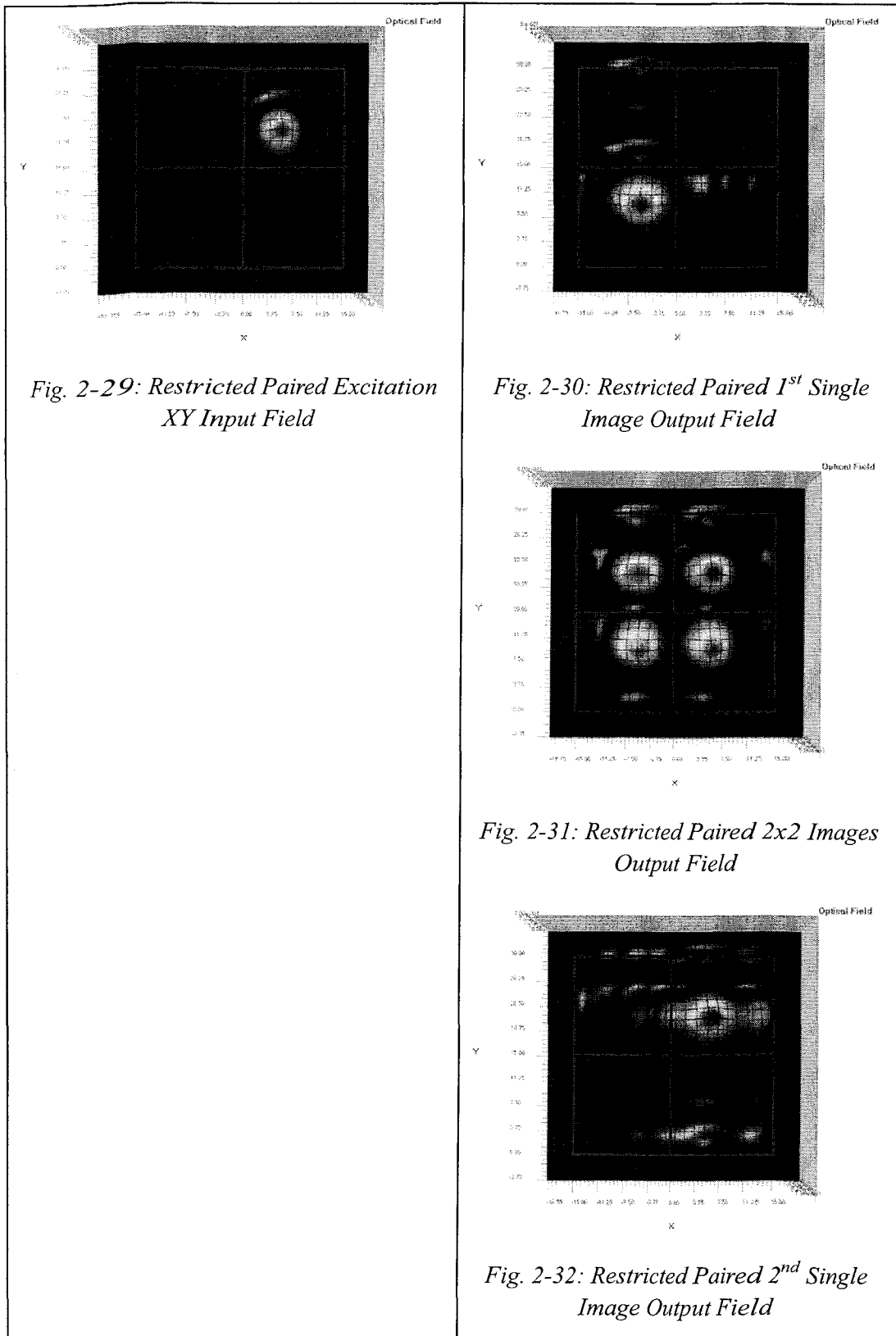


Fig. 2-29: Restricted Paired Excitation XY Input Field

Fig. 2-30: Restricted Paired 1st Single Image Output Field

Fig. 2-31: Restricted Paired 2x2 Images Output Field

Fig. 2-32: Restricted Paired 2nd Single Image Output Field

Table 2-11: Simulation of Restricted Paired Interference XY Image

For this and symmetric restricted interference, image lengths are greatly reduced compared to general interference. The only difficulty is to align the input at the restricted locations.

From Fig. 2-32 and some other resulting figures, the Gaussian nature of the input was not preserved. There are also mismatches between the simulation and the theoretical image lengths. These and other issues are studied in the next chapter along with an analysis of different parameters such as device dimensions, input wavelength, index differences, polarization, and other tolerance concerns.

[3] Imaging and Tolerance Analysis

3.1 Introduction

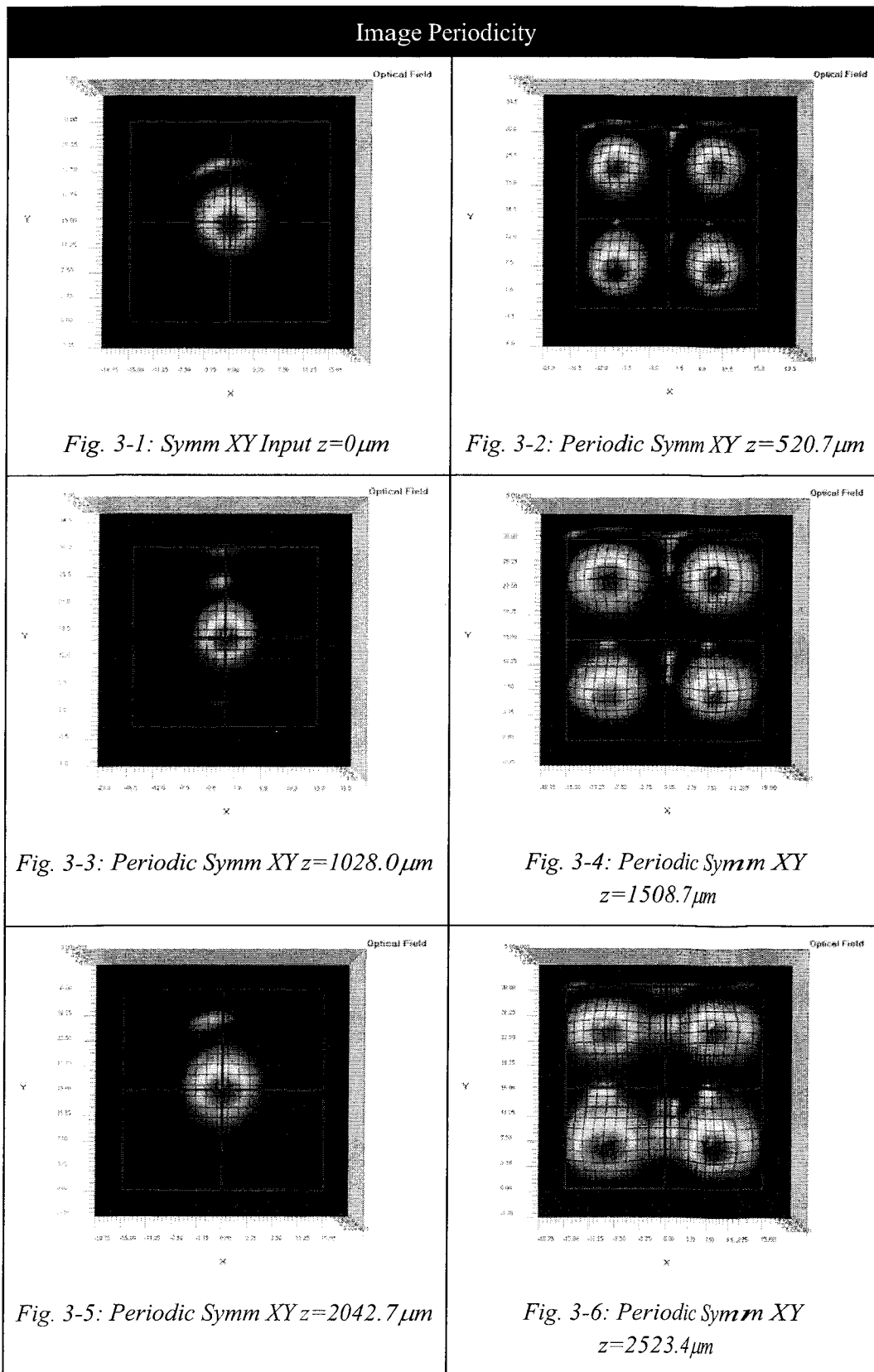
The purpose of 3DMMI is to be able to distribute uniform power to N images at image distances that are tolerant to various parameter perturbations. From the simulations completed in the previous chapter, it is evident that images are not perfect replicas of the input. The simulation distances obtained were not the best imaging distances and it is crucial to understand that imaging does not occur at one location. The best image location is the location of the best representation of the original input. These and other important tolerance parameters including variations in the input and the waveguide were studied. The imaging type under study was chosen to be only Symmetric-XY interference for simplicity. Other types of interference imaging will produce similar tolerance results.

3.2 Imaging Length and Quality

3.2.1 Image Periodicity

Imaging is physically periodic since there is a finite number of modes and the spatial frequency of each mode is a multiple of a fundamental frequency. This is an important feature of MMI devices since designed images can be tailored at a number of distances. In a practical rectangular waveguide, image distortion will occur due to the non-ideal nature of the medium such as local variations in indices of refraction, cross-sectional dimension, and as well as asymmetric cladding losses. Thus, periodic 3DMMI images will undergo slight deterioration with distance since width or index of refraction can never be constant through out the entire guide. This idea can be shown with the simulation of symmetrical images. The original input was split symmetrically

into 2x2 images and back to a single image at multiple locations in z shown below:



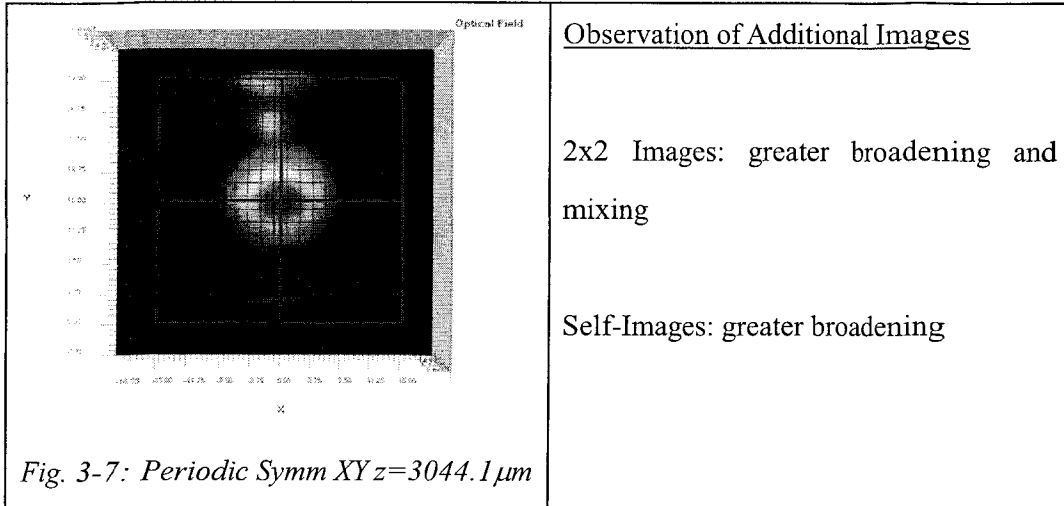


Table 3-1: Periodicity of 3DMMI (Symmetric Imaging)

All of the self and 2x2 images above appear periodically and broaden as the signal travels along z. This broadening is mainly due to various estimation and asymmetry in the simulation algorithm. This simulation behavior should reflect the behavior of imaging in practical waveguides with slight variations along z. The behavior of the above simulation can also be evaluated by the Power Overlap Integral (POI), which is defined as

$$POI = \frac{|\int E_1(x, y)E_2(x, y)dxdy|^2}{\int |E_1(x, y)|^2 dxdy \cdot \int |E_2(x, y)|^2 dxdy} \quad (3.2.1)$$

with two fields E_1 and E_2 to determine the representation of an image field with respect to the original. The simulated POI is illustrated in Fig. 3-8. An ideal situation will give a graph with all POI peaks equal to one for self-images and all POI valleys equal to zero for 2x2 images, assuming the input image does not overlap the 2x2 images. Although not an indication of image spatial broadening, this graph provides some indication of the reduced peak power output for coupling. From the simulation, imaging beyond a distance of the third self-image will be severely broadened with lowered POI less than 80%. Severe broadening will introduce lobed peaks near a self-image or 2x2 images, which are all undesirable. In summary, depending on tolerances, the most desirable images should be chosen at the shortest possible distance, preferably the first image location.

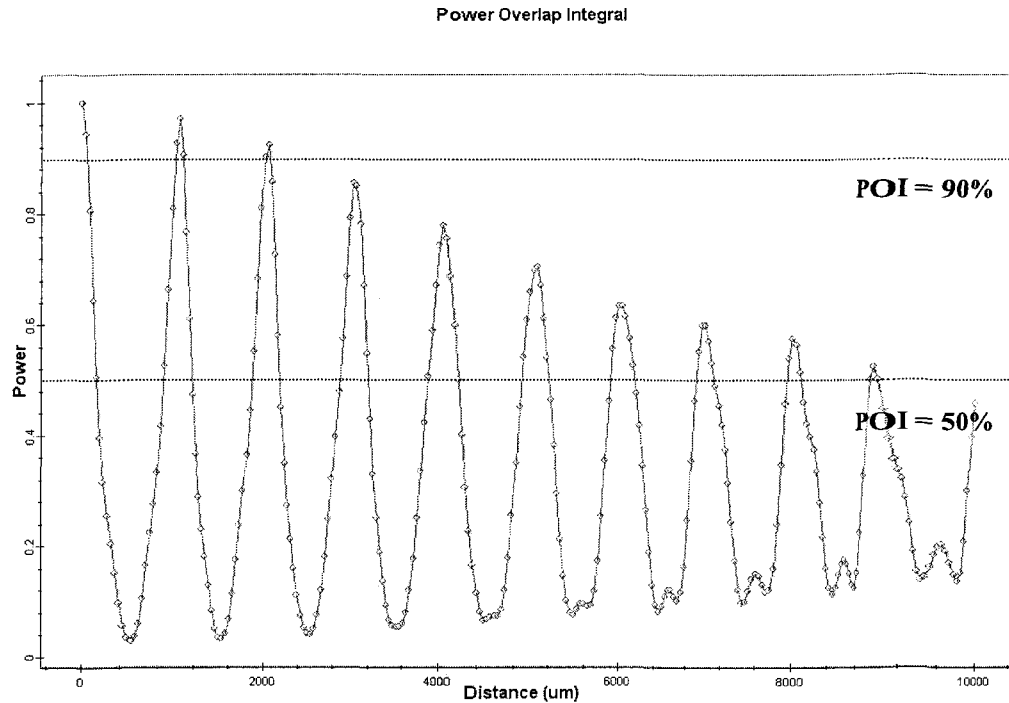


Fig. 3-8: Periodicity POI Symm XY

3.2.2 Image Range

As mentioned before, the image cross-sectional fields in the above figures were chosen at maximum peak values. In reality, there is a range of image locations in z as fields combine or split into the desired images. Thus, slight variations in device lengths can be tolerated at the expense of lower peak power or inferior image shape. Consider a self-image in the symmetric-XY case. Choose the location for the highest POI and define the image range as the -3 dB power image locations on both sides of the maximum. In this case, the maximum power occurred at $z = 1028 \mu\text{m}$ with relative peak power of 0.904. The lower end -3 dB power field distribution occurred at $928 \mu\text{m}$ and the higher end at $1096 \mu\text{m}$, which corresponds to an image range of $168 \mu\text{m}$. In a practical application where the image length is $1028 \mu\text{m}$, an image range of $168 \mu\text{m}$ indicates that higher than -3 dB power coupling can be achieved in a large variation of lengths around the nominal. Similar results were seen with the 2x2 image

locations illustrated by valley minima. Despite the fact that the -3 dB power image range for 2x2 images was 168 μm , the tradeoff was image mixing between the four images.

For practical applications, a more demanding approach for the image range is the 90% or -0.5 dB power loss from the peak. For the same above case, the -0.5 dB power image range is 65 μm for the first self-image while it is 58 μm for the first 2x2 images. In any individual case, the image range will generally be around the maximum peak location. With a large number of possible perturbations, the image range is difficult to obtain theoretically with an analytical approach to the known MPA relations. With simulations, the general idea of image range can be estimated and related to practical applications. The following table summarizes the image range of the different types of 3DMMI images. Note that the analysis of images with respect to X and Y will be represented only by Y.

Imaging Type	Image Distance (μm)	Image Range (μm)	
		-3dB	-0.5dB
Self Image			
General:	8026.0 μm	-	111 μm
Paired:	2689.0 μm	-	59 μm
Symmetric:	1028.0 μm	168 μm	65 μm
Mirror Y Image			
General:	8006.0 μm	-	103 μm
Symmetric:	4005.3 μm	308 μm	79 μm
Cross Image			
General:	3998.0 μm	348 μm	46 μm
Paired:	1364.6 μm	-	78 μm
2x2 Images			
General:	2024.1 μm	-	44 μm

Paired:	682.3 μm	-	55 μm
Symmetric:	520.7 μm	168 μm	58 μm

Note: - indicates -3dB not achievable

Table 3-2: 3DMMI Initial Simulation Image Range

3.2.3 Image Resolution

Image Resolution is a measure of how sharp the input is represented by the output image. In every waveguide, there exists an approximate resolution for the desired image. Image resolution can be analyzed with an amount of mode-to-mode transfer from an initial object at $z = 0$ to the image at $z = L$ [44]. This resolution can be simply defined as the half power full width of the resultant field shown in Fig. 3-9.

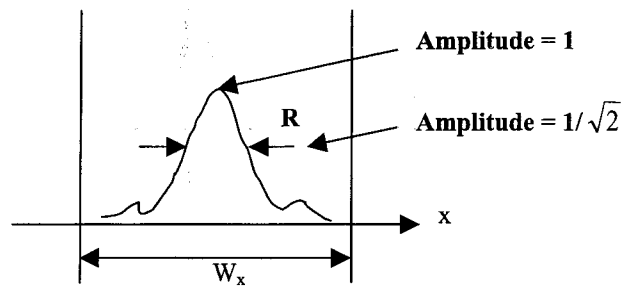


Fig. 3-9: Image Resolution

In an ideal situation where all information from object modes is transferred to corresponding image modes, the resolution R is approximated as

$$R \approx \frac{0.89W_{xeff}}{M}, \quad (3.2.2)$$

where M is the total number of propagation modes. In practical cases, higher order modes are attenuated. Assuming a Gaussian model for the loss, further analysis showed that the resolution for practical Gaussian fields is then adjusted to

$$R \approx \frac{1.50W_{xeff}}{M}. \quad (3.2.3)$$

Intuitively, resolution is dependent on how many modes can span across the entire effective width.

For 3DMMI, mode-to-mode transfer is described in two dimensions since the modes are defined in two dimensions. From previously, two-dimensional fields can be approximated by a separation of variables of the two transverse directions. If the above analysis describes the resolution in the x direction, then the result would be the same in the y direction. Thus, resolution for a two dimensional image will remain the same in both transverse directions for a symmetrical input.

3.3 Input Characteristics

3.3.1 Input Halfwidth

Consider a Gaussian distribution by omitting the scalar factor in the form of

$$G(x, y) = \exp \left[-\frac{1}{2} \left(\frac{x - x_c}{\sigma_x} \right)^2 - \frac{1}{2} \left(\frac{y - y_c}{\sigma_y} \right)^2 \right] \quad (3.3.1)$$

where x_c and y_c represents the position of the field, and σ_x and σ_y are the standard deviations in each direction. The Input Halfwidth (HW) is defined as the transverse half width of a Gaussian field at $1/e$ or $\sqrt{2}$ times its standard deviation. A broad input, one with higher HW, not only decreases the image resolution, it will also decrease contrast due to multiple image mixing. The total number of modes in a three-dimensional square dielectric waveguide can be approximated as

$$M_{xy} \approx M^2 \approx \frac{\pi}{4} \left(\frac{2W_x}{\lambda_0} \right)^2 (n_g^2 - n_c^2), \quad (3.3.2)$$

where M is the same from section 3.2.3, and M_{xy} is rounded to the nearest integer and is based on mode plotting in frequency space [4]. If $W_x = 30 \mu\text{m}$, the effective width is $31.1 \mu\text{m}$, and M_{xy} is 238. From Eq. 3.2.3, the resulting resolution is approximately $3.11 \mu\text{m}$. Since the half power full width of a Gaussian input field is $\sqrt{2(\ln 2)}HW$,

the input HW is found to be approximately 2.64 μm . Since resolution relies on the effective width and the number of supported modes, this dependence can be illustrated by the following Fig. 3-10.

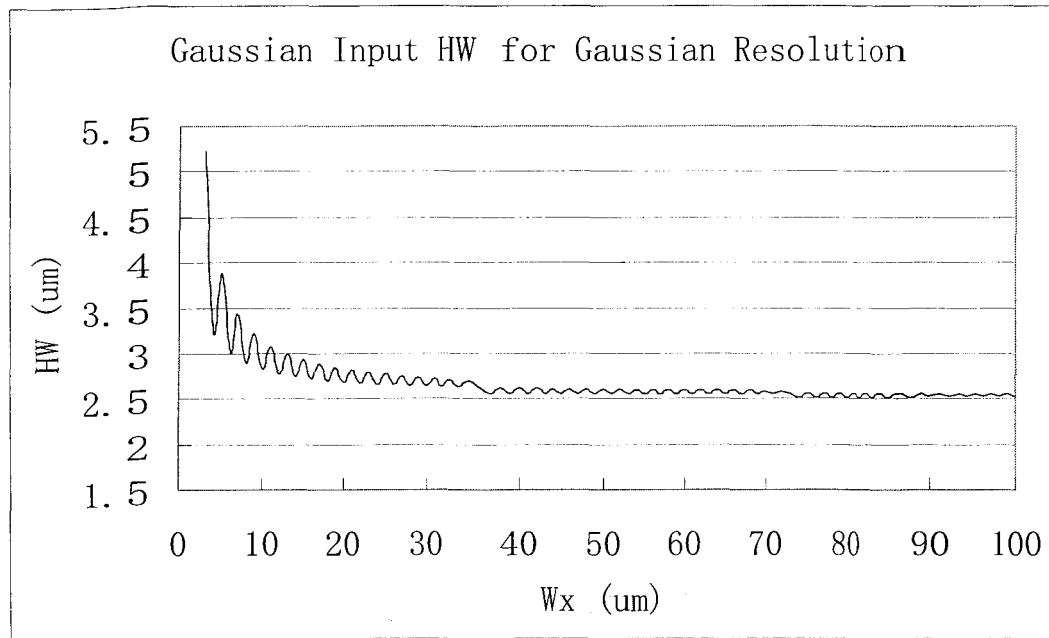


Fig. 3-10: Approximate Resolution Matching Gaussian Input HW

As the width increases, effective width and the number of supported modes also increase. The behavior of Fig. 3-10 indicates that as the number of modes increase, HW required approaches to about 2.5 μm .

For HW of 1 μm , resolvable width is violated; thus, clean and well-defined images with high POIs are not produced. Fig. 3-10 estimates HW required in the presence of a large number of supportable modes within the waveguide. It is important to note that Eq. 3.3.2 holds for high values of M_{xy} , preferably >100 modes. This is reflected from the sharp drop in HW from the 0-250 modes range, or $W_x < 8 \mu\text{m}$. From the following Table 3-3, the limited HW = 2.0 μm produces a low-resolution image and this is not the case for HW = 3.4 μm . In practical applications, the input HW must be chosen to be slightly higher than the estimated HW length according to Fig. 3-10. However, when the HW is too large relative to the width of the waveguide, image contrast will decrease as shown in Fig. 3-13 and Fig. 3-14. Image contrast is highest when M or less number of images is extended with no

overlapping in W_x or W_y . If the input is a Gaussian distributed field, then it can be described spatially by its Mode Field Diameter (MFD). MFD is the diameter of Gaussian function when its power falls to $1/e^2$ or 2 times the HW. Spatially, in a $100 \times 100 \mu\text{m}^2$ guide with $\text{HW} = 5 \mu\text{m}$, the $10 \mu\text{m}$ MFD fits 10 times in either the x or y directions producing good contrast images.

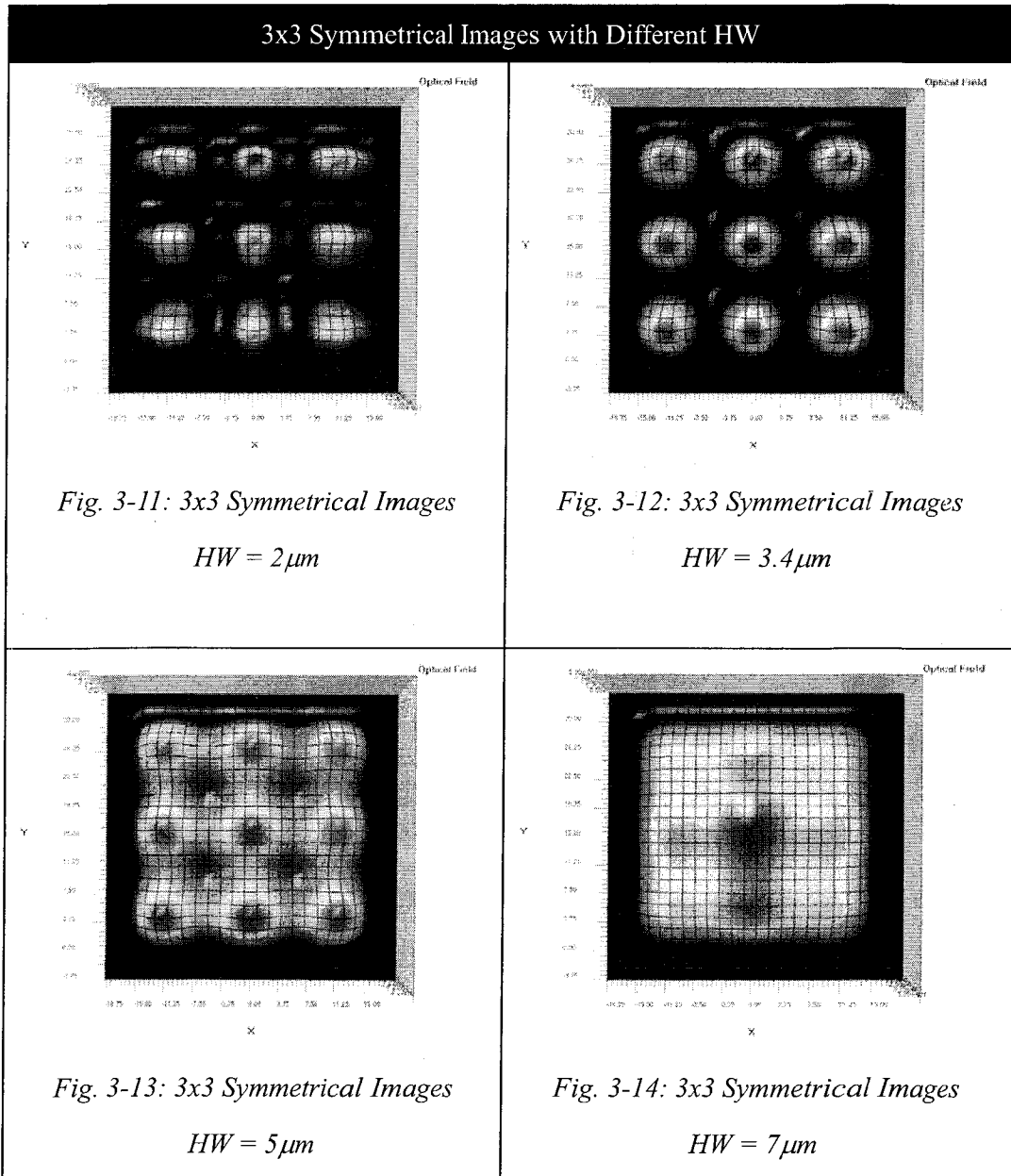


Table 3-3: 3x3 Symmetrical Images with Different HW

To prove the dense high resolution and high contrast capability of 3DMMI, Table 3-4 depicts $M \times N$ images appearing in a $100 \times 100 \mu\text{m}^2$ cross-section with $\text{HW} = 3.33 \mu\text{m}$.

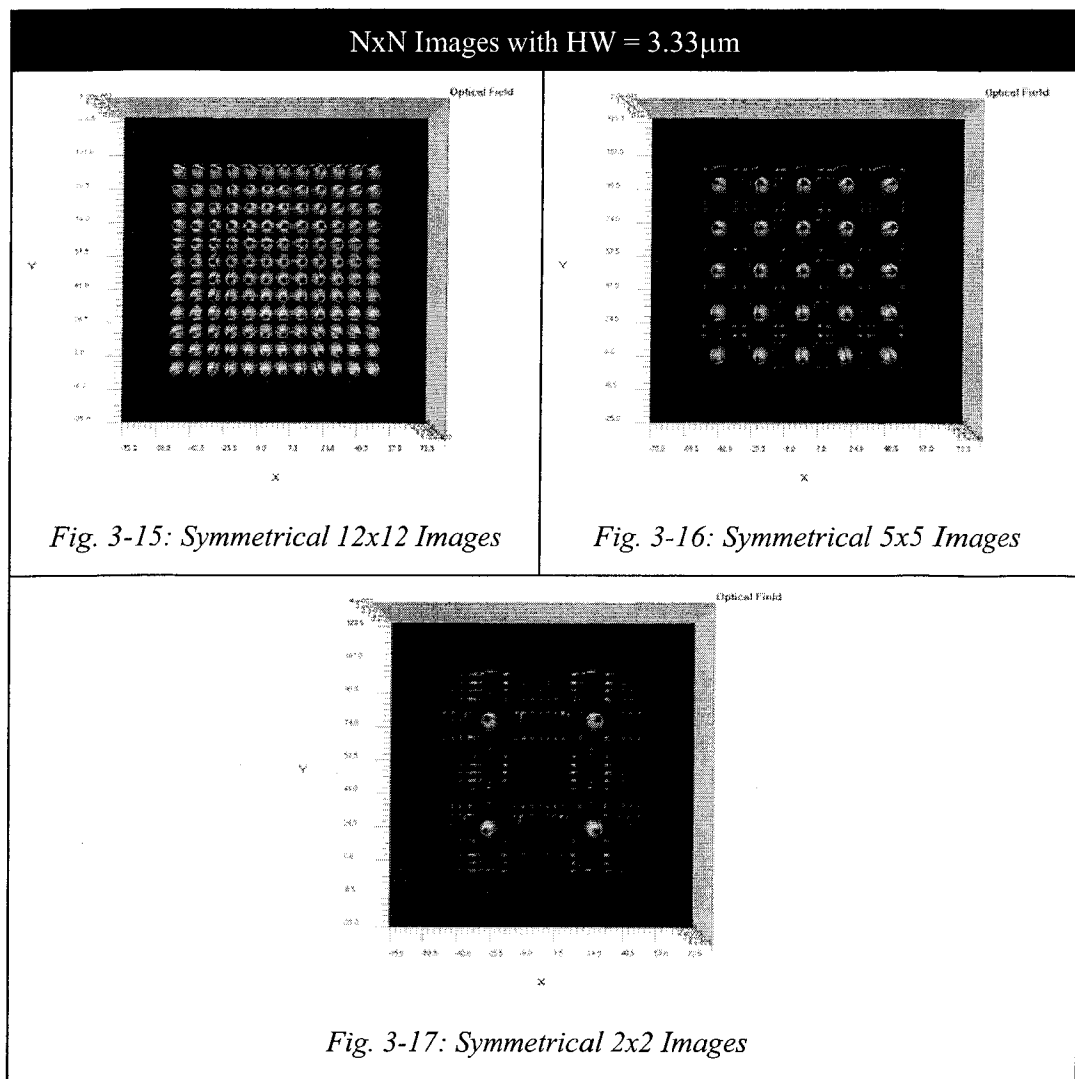


Table 3-4: MxN Symmetrical Images with HW 3.33 μ m

3.3.2 Input Location

The location on the two dimensional input field, where an input is launched, is crucial for determining the type of image. Previously in the symmetrical-XY case, an input may shift on the x- or y-axis causing a different result. It is obviously not desirable to shift the input too far from the desirable location since small shifts may distort the image shape but are most influential to the imbalance of multiple images. Imbalance for multiple images is simply defined as the power difference between the

highest and the lowest image peaks. Consider the small deviation of a symmetrical-XY input at the center with $x = 0 \mu\text{m}$ and $y = 0 \mu\text{m}$, according to the defined axes. Shift the x position of the input to $1 \mu\text{m}$ and $2 \mu\text{m}$ while keeping the y at $0 \mu\text{m}$, then shift the input to $x = 2 \mu\text{m}$ and $y = 2 \mu\text{m}$. The following table illustrates imbalance changes due to the input within a $30 \times 30 \mu\text{m}^2$ guide:

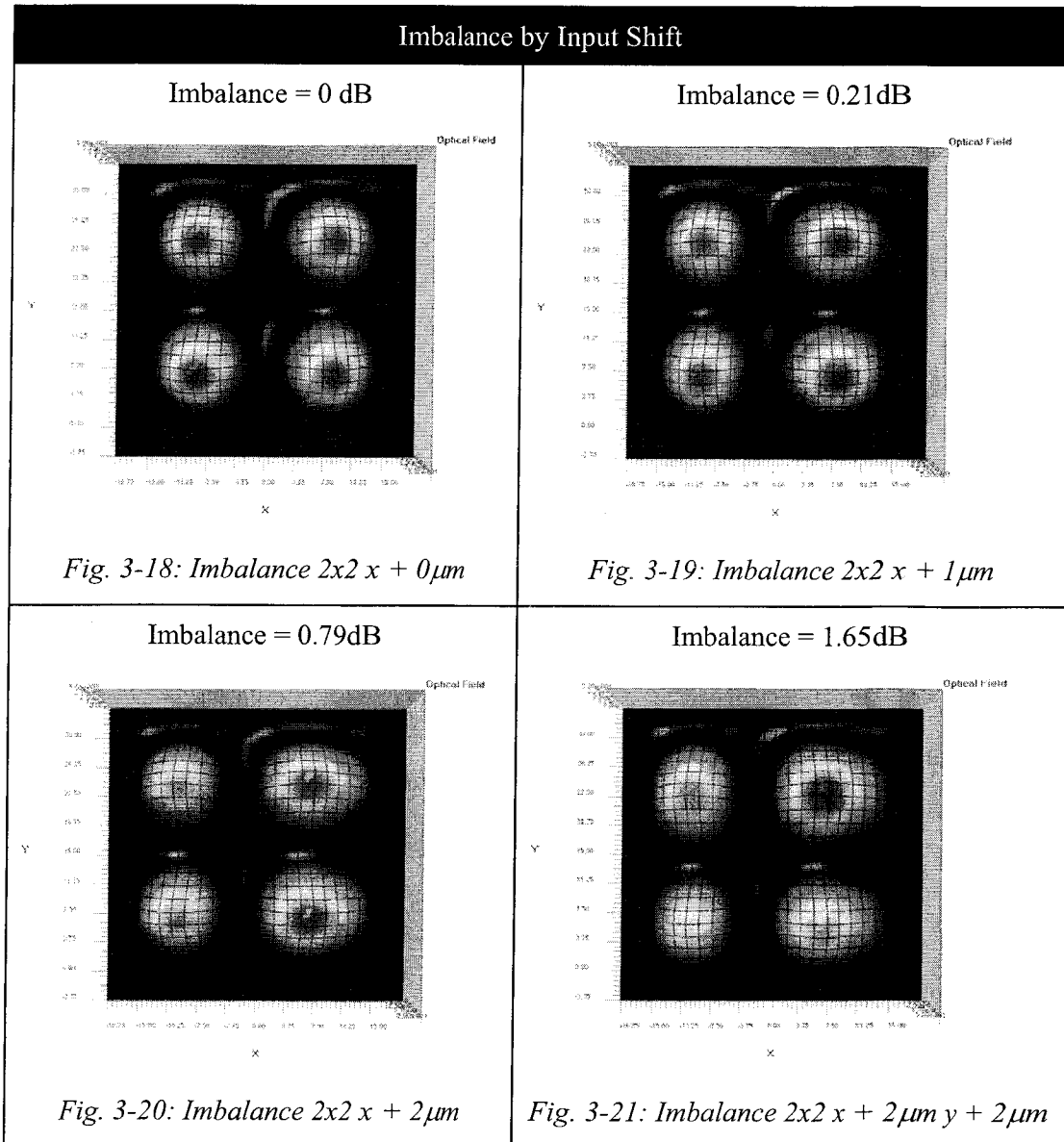


Table 3-5: Imbalance by Input Shifts

The above images were captured at the same image location along z. From Fig. 3-19, the 0.21 dB imbalance due to a $1 \mu\text{m}$ input shift still produces an acceptable symmetrical image. As input center shifts, its power also shifts in the same direction.

As the center input shifts in x , more power or image field is shifted to the positive x side. In addition, when the input shifts towards the top-right quadrant, the power and image field also follow in the same direction shown in Fig. 3-21. In this case, the imbalance is as high as 1.65 dB. Since symmetrical images require a strict input location, tolerance is low in terms of input shift. Thus, in practical devices, a higher tolerance of imbalance may be required.

3.3.3 Input Wavelength

Since the beat length is inversely proportional to wavelength, the imaging length of 3DMMI devices is longer with shorter operating wavelengths. Thus, images with a wavelength of 670 nm, for example, will appear at longer device lengths compared to a longer wavelength of 1550 nm. However, the resulting images will be identical. In the case of symmetric-XY, as the number of $M \times N$ ($M=N$ for symmetric-XY) increases, the dependence on wavelength minimizes due to a dramatic decrease in the device length. If we consider a band of wavelengths around 670 nm, the dependence of the image length on wavelength is greater than if the band is around 1550 nm. This characteristic can be shown with Fig. 3-22 with a range of ± 20 nm around these nominal wavelengths. The image distance difference is between the image length at the nominal wavelength $+20$ nm and -20 nm. The value of ± 20 nm was chosen to represent a typical range of Dense Wavelength Division Multiplexing (DWDM) channel around the nominal wavelength with a channel spacing of 0.8 or 1.6 nm. In addition, a mid-range nominal wavelength of 980 nm is also included. For 1550 nm and higher wavelength applications, this distance deviation is negligible ($<1\%$) compared to the nominal image distance. The wavelength deviation of ± 20 nm is considered large since in practical applications with a fixed wavelength source, wavelength drift is usually in the range of ± 1 nm. If this realistic range of wavelength drift is considered, then the image distance difference is only 6 μm with a 2200 μm nominal image distance. For a nominal image distance of 198 μm , the distance

difference is only 0.25 μm . Thus, it can be concluded that image distance difference is insignificant with small deviations around the nominal wavelength.

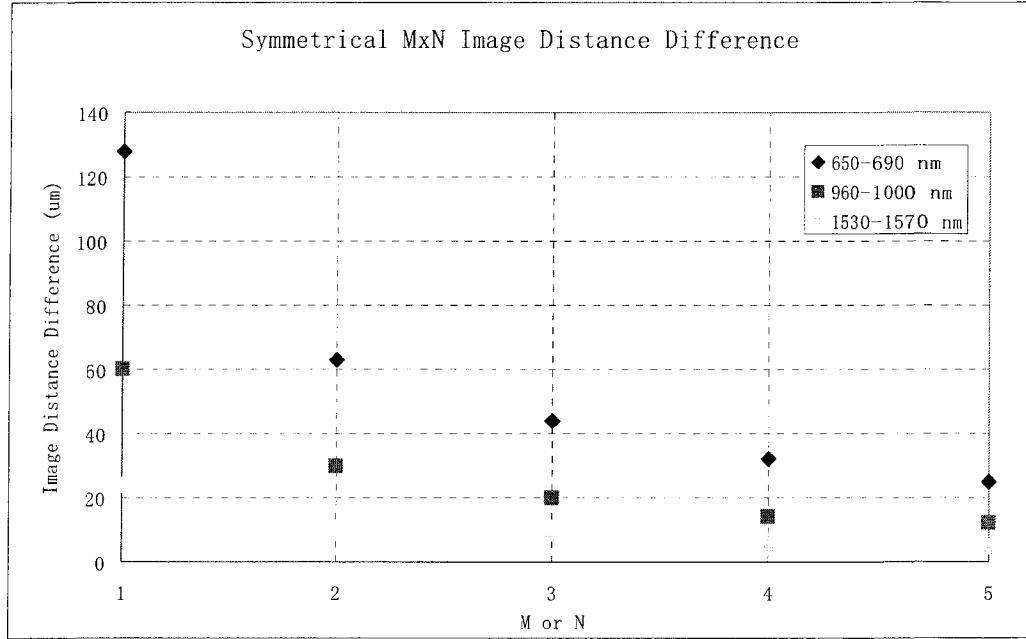


Fig. 3-22: Symmetrical MxN Image Distance Difference

3.3.4 Input Polarization

So far, all simulation and theoretical studies have been completed based on the TE polarization. Now consider TM polarization and its affect on the effective width and consequently the image length. Polarization dependence appears in the effective width from Eq. 2.3.5 and 2.4.5. The ε factor now becomes unity, which introduces the

$\left(\frac{n_c}{n_g}\right)^2$ index factor in the second term. If the two indices were similar, this term

would be insignificant; otherwise, the square root term would greatly differentiate the effective the physical width. Strictly speaking, if the linear input electric field is polarized in the x direction (TE polarization), then W_{yeff} should contain the above index factor since it hosts the TM field. If the linear input electric field is polarized in the y direction (TM polarization), then W_{xeff} should contain the index factor since it now hosts the TM field. Assume W_{xeff} is unaffected by the index factor, then it can be

compared with $W_{y\text{eff}}$ affected by the index factor in Fig. 3-23 with different ratios of n_c/n_g assuming $W_x=W_y=30\ \mu\text{m}$:

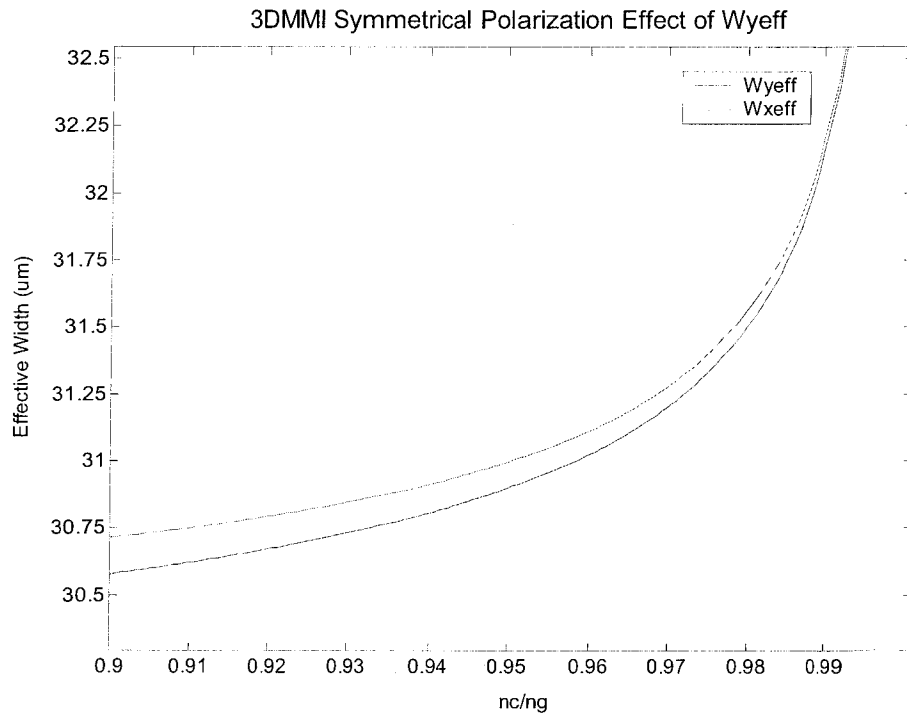


Fig. 3-23: Polarization Effect on Effective Width

As the n_c/n_g ratio reaches unity, the effective width reaches infinity. In prior simulations, the n_c/n_g ratio was 0.959, which produces an effective width difference of only $0.09\ \mu\text{m}$ according to Fig. 3-23. As the n_c/n_g ratio increases, the effect of polarization becomes insignificant. However, in large index difference applications, this effect increases in importance. If the cladding is now considered to be air while the index of the guide is still 1.585, then $n_c/n_g=0.63$. With this index ratio, the effective width difference becomes $0.25\ \mu\text{m}$. In practical applications, a large effective width difference due to polarization will deteriorate the desired output in terms of image length and power distribution. Image distances can be compared between the nominal and polarization-affected images for $n_c/n_g = 0.96$ and $n_c/n_g = 0.63$ with a number of $M=N$ symmetrical images in Fig. 3-24. The effect of polarization is threefold as much with an n_c/n_g ratio of 0.63 as compared to an n_c/n_g ratio of 0.96 for self-images. However, a $15\ \mu\text{m}$ difference in the image distance is

still a relatively small value ($\sim 0.5\%$) compared to the actual image length.

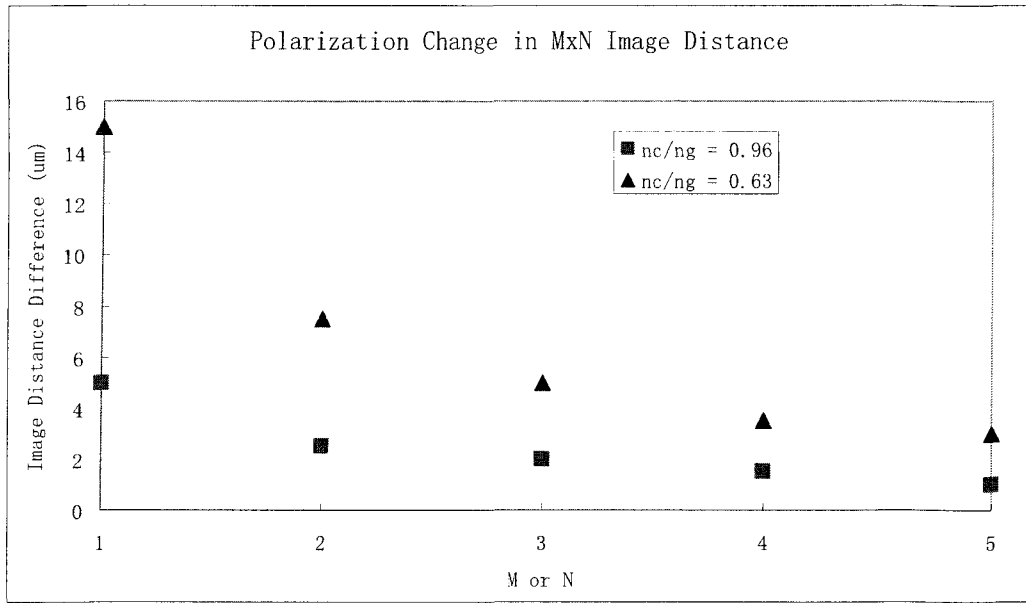


Fig. 3-24: Polarization Effect on Image Distance

Using the BPM simulation tool, a TM input field produced the same image compared to the TE case. The difference between TE and TM polarized inputs is considered negligible for imaging and this is an important advantage for 3DMMI devices.

3.4 Waveguide Characteristics

3.4.1 Refractive Index

Effect of Image Distance by n_c

Assume $n_g = 1.585$ is kept constant, the wavelength is 1550 nm, and the guide dimension is $30 \times 30 \mu\text{m}^2$. The image distance difference between $n_c = 1.55$ to 1.00 is $69 \mu\text{m}$ for the self-image case and is only $14 \mu\text{m}$ for the 5×5 images case. This analysis is, of course, over a large range of cladding indices. In this case, the cladding material changes completely in reality such as from a polymer to air. Nonetheless, this change in image length is small compared to the actual length.

Effect of Image Distance by n_g

Assume $n_c = 1.52$ is kept constant, the wavelength is 1550 nm, and the guide dimension is $30 \times 30 \mu\text{m}^2$. Suppose the guide index changes from $n_g = 1.59$ to 1.56, then the image distance difference is $3.2 \mu\text{m}$ for self-images and is merely $0.64 \mu\text{m}$ for 5×5 images. Again, this amount of change in n_g can be concluded to be insignificant compared to actual image distances.

In a practical device, cladding and guide index may deviate by only a small amount from nominal values due to fabrication. Assume an index shift of ± 0.01 , the image distance differences between $n_c = 1.53$ and 1.51 with $n_g = 1.575$ and 1.595 are independently compared in Fig. 3-25. The effect of n_c is more significant than n_g , which can be neglected. Even though the effect of n_c can reach $11 \mu\text{m}$ for single images, this value is still only about 0.4% of the actual image distance. Small shift in refractive indices can be concluded to have negligible effects on the image length.

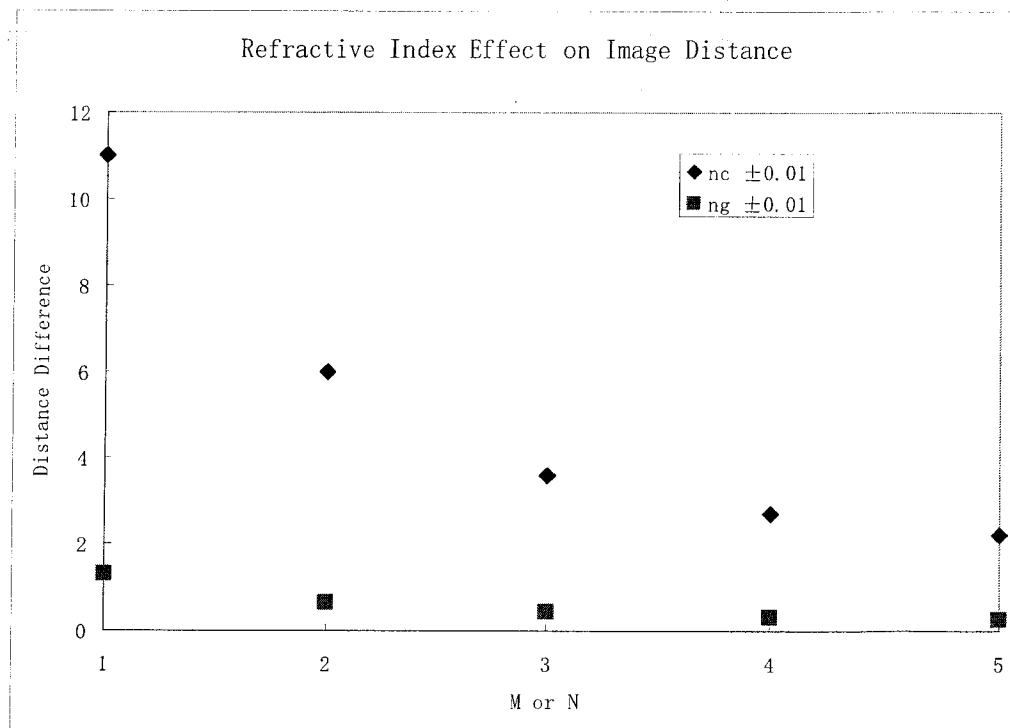


Fig. 3-25: Refractive Index Effect on Image Distance (n_g and n_c)

3.4.2 Waveguide Width

The physical width and deviation of the width from nominal is the most crucial and the most influential parameter for 3DMMI. For fabrication, it is impossible to create a structure that corresponds to exact design. The image distance dependence on transverse dimensions is quadratic shown in Fig. 3-26. The wavelength is 1550 nm and the guide and cladding indices are 1.585 and 1.52 respectively. An increase of merely 13 μm in width from 30 μm produces a doubled image length compared to the original length for self-images. This effect is much less for higher $M \times N$ images or with smaller 3DMMI dimensions. In order to utilize larger dimension 3DMMI, it is vital to optimize fabrication for small width deviations and acceptable tolerances.

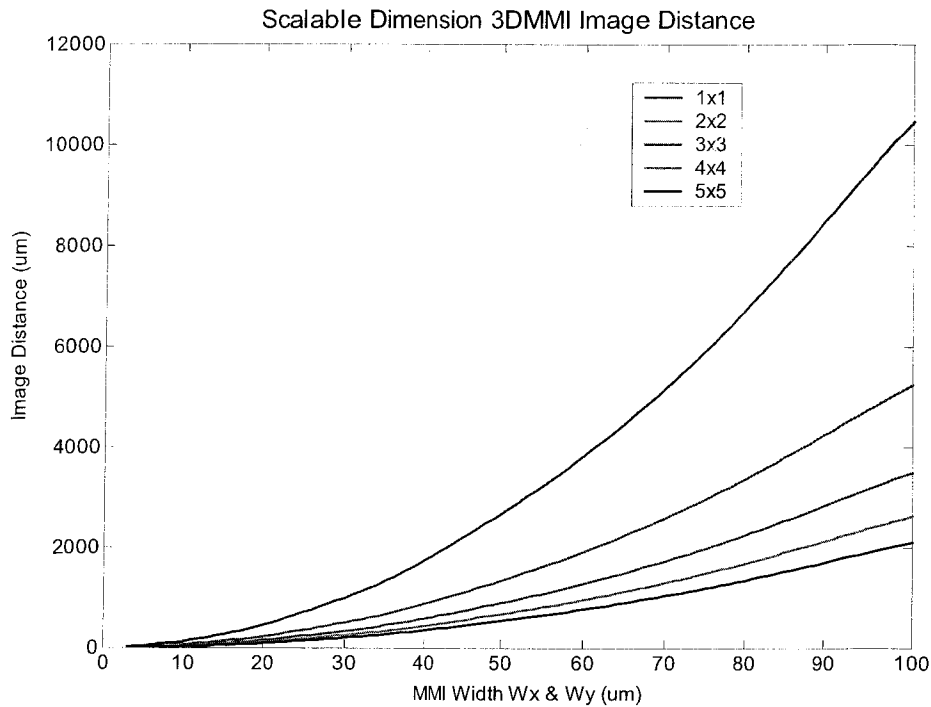
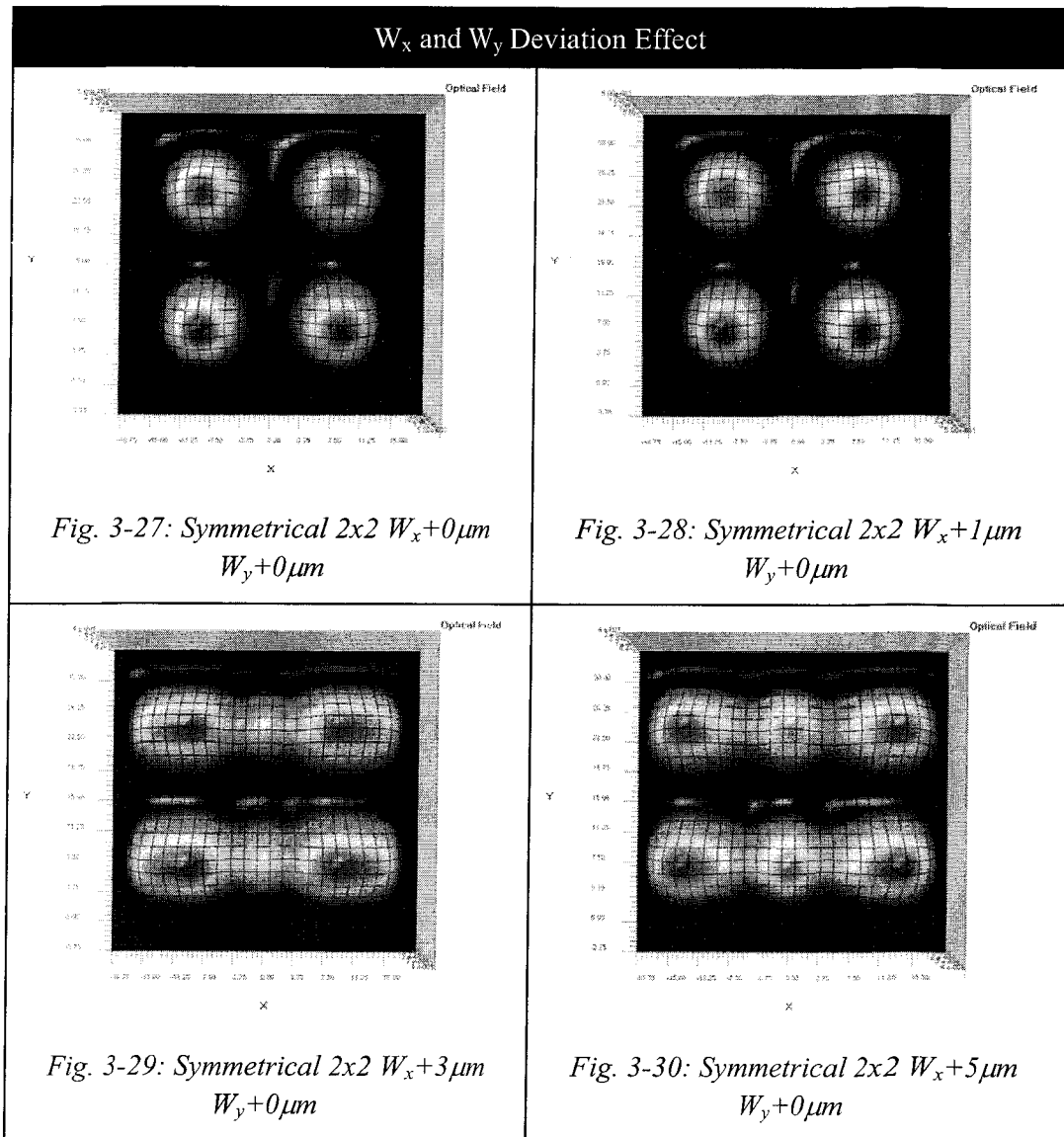


Fig. 3-26: Scalable 3DMMI Image Distances

In practice, waveguide dimensions can deviate in both the x and y directions. For a symmetrical-XY input, these dimensional imperfections disrupt the symmetrical nature of imaging. In addition, an analytical solution to the exact location of the most desirable image is difficult to obtain due to large Δ_x and Δ_y factors. However,

dimensional deviation can be investigated using simulation. Table 3-6 illustrates the result of width changes in one or both directions at the same image distance. By assuming a $30 \times 30 \mu\text{m}^2$ nominal guide, the addition of $1 \mu\text{m}$ to W_x in Fig. 3-28 shows little effect from the nominal image of Fig. 3-27. However, the addition of 3 and $5 \mu\text{m}$ seems to stretch the field images since W_x has been stretched. A third image in the x direction begins to form. In practical devices, a width increase of $5 \mu\text{m}$ in the x direction may be an overestimate. In Fig. 3-31 where both W_x and W_y are increased, the resulting image resembles that of Fig. 3-29 since both W_x values have the same deviation. The only difference is that the image also stretches slightly in the y direction.



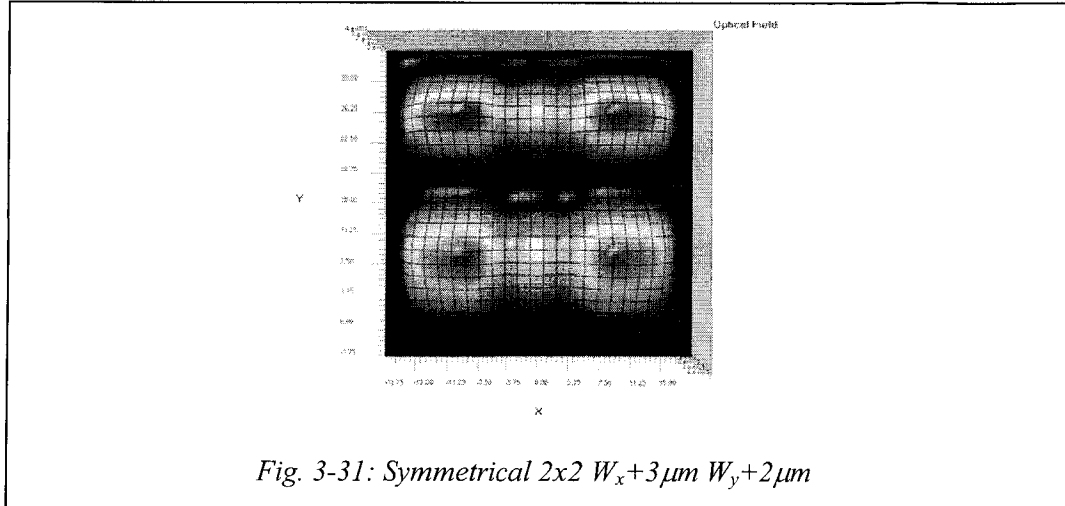


Fig. 3-31: Symmetrical 2x2 $W_x+3\mu\text{m}$ $W_y+2\mu\text{m}$

Table 3-6: W_x and W_y Deviation Effect on Symmetrical Images

3.5 Additional Analysis

3.5.1 Fabrication Tolerances

The fabrication tolerances of a 3DMMI can be further studied by directly investigating the basic beat length equations based on the parameters L , W_{eff} ($W_{x\text{eff}}$ or $W_{y\text{eff}}$), W (W_x or W_y), λ_0 , and n_g . Consider a square waveguide under the conditions of general interference, symmetrical interference, and paired interference where their image lengths differ by factors of 3, 3/4, and 1 respectively. Symmetrical interference offers the shortest length for imaging since it requires fewer modes for interference. Performing an implicit derivative of the basic beat length equations will determine the relationship of fabrication tolerances:

$$\frac{|\delta L|}{L} = 2 \frac{|\delta W_{\text{eff}}|}{W_{\text{eff}}} = \frac{|\delta \lambda|}{\lambda_0} = \frac{|\delta n_g|}{n_g} = 2 \frac{|\delta W|}{W}, \quad (3.5.1)$$

where δL , δW_{eff} , δW , and δn_g factors are fabrication tolerance determinants. Take a Gaussian beam diverging in x while maintaining its profile in the y direction and calculate its normalized power transmission at a deviation distance δL from the original image distance, say $z=0$. It can be shown that the transmission (T) becomes

the following:

$$T = \frac{1}{\sqrt{1+Z^2}}, \quad (3.5.2)$$

where Z is $(2\lambda_0\delta L)/(\pi n_g w_0^2)$ with w_0 as the beam waist, which is the $1/e$ width of a Gaussian beam [45]. In terms of 3DMMI, both x and y directional conditions must be satisfied for imaging; thus, the transmission of the optical field becomes a double integral of x and y components. Since we assume approximate separation of variables for x and y components, transmission for 3DMMI can be a direct extension of Eq. 3.5.2 by introducing both Z_x and Z_y independent factors:

$$T = \frac{1}{\sqrt{1+Z_x^2}} \frac{1}{\sqrt{1+Z_y^2}}. \quad (3.5.3)$$

The only difference between Z_x and Z_y is their respective δL_x and δL_y factors, which are respective changes to the overall image distance due to x and y directional conditions. An excess loss value (EL) is required to analyze the transmission loss (Loss = 0 dB at $T=1$) represented by a decibel value of T .

Fabrication tolerances can be analyzed as the effect on EL due to fabrication parameters (controllable/uncontrollable) L , W_x or W_y , and n_g . Both factors δL_x and δL_y may be different due to different beat lengths [30]; thus, with a matrix of δL_x and δL_y due to the three types of interference imaging, the fabrication tolerance of W_x or W_y , and n_g can be determined using Eq. 3.5.1. Three-dimensional mesh plots can be generated using previous simulation parameters and a beam waist of $6.66 \mu\text{m}$, which approximately corresponds to a $3.33 \mu\text{m}$ HW in BPM. The general behavior of fabrication tolerance is illustrated in Fig. 3-32 by a three-dimensional mesh plot for excess loss with changed in δL_x and δL_y . The result is a quadratic relationship between excess loss and the change in lengths. As δL_y increases, the excess loss increases even with δL_x maintained at $0 \mu\text{m}$. The loss difference between $\delta L_y = 0 \mu\text{m}$ at the top of the band and $\delta L_y = 100 \mu\text{m}$ at the bottom of the band with $\delta L_x = 0 \mu\text{m}$ is roughly -2.4 dB for the general interference case. For the purpose of Fig. 3-32, $dL = \delta L$. Similar plots of Fig. 3-32 can be generated with changes in n_g and W . To simplify the analysis, set $\delta L_y=0$ to generate single curves. Fabrication tolerances from general,

symmetric, and paired multi-image interferences are illustrated in table 3-7 of three figures.

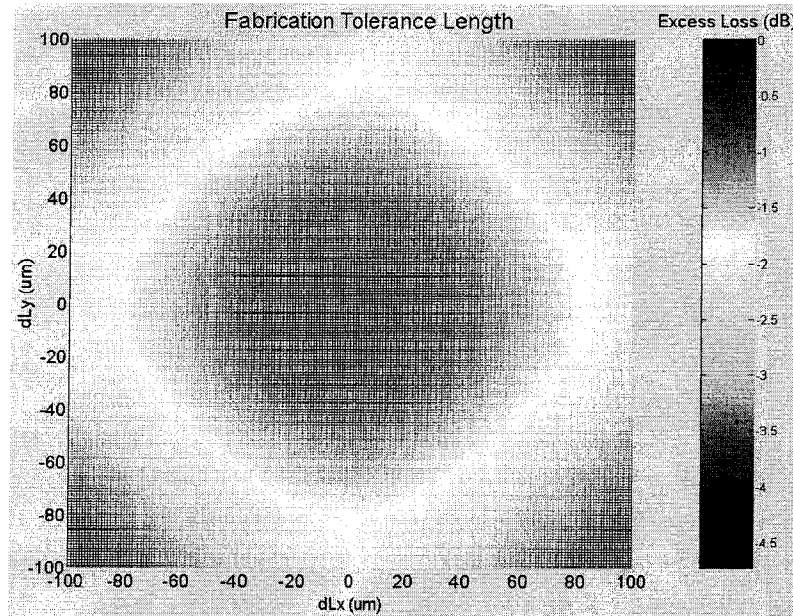


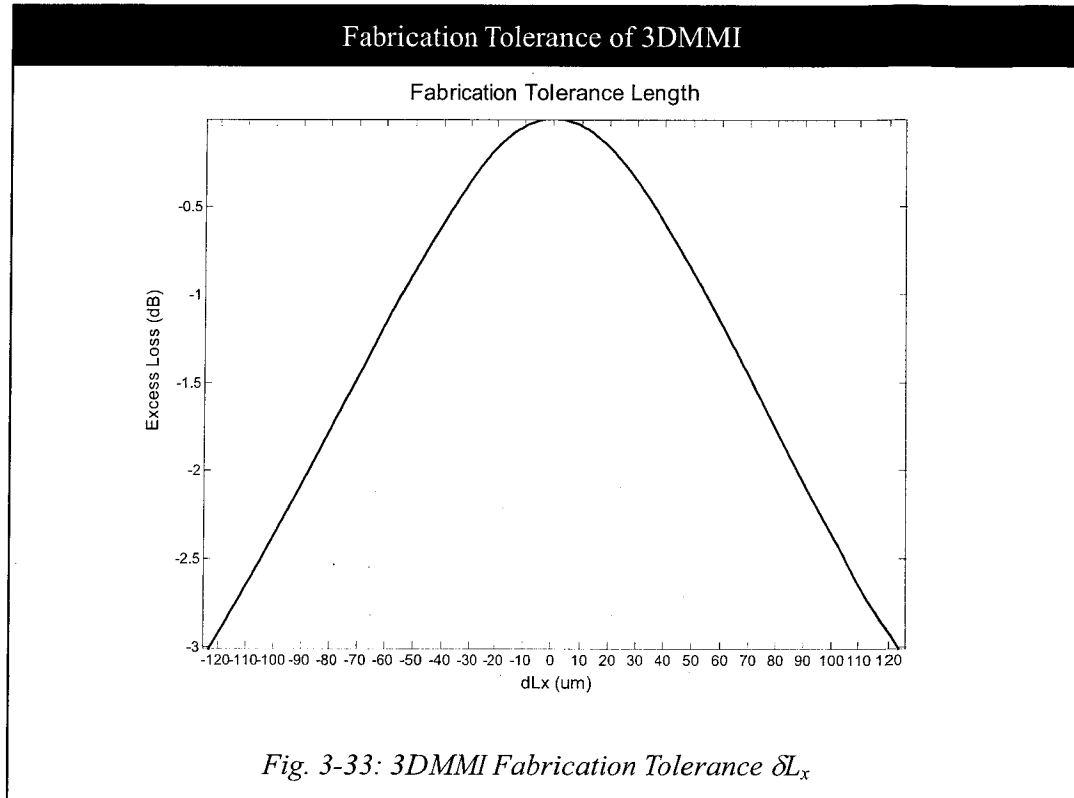
Fig. 3-32: 3DMMI Fabrication Tolerance 3D-Mesh Plot Top View

Fig. 3-33 shows excess loss with the fabrication tolerance of δL_x and its behavior is independent of the type of imaging. For a -0.5 dB loss tolerance ($\sim 90\%$ transmission), δL_x can be as large as $35 \mu\text{m}$ while a half-power -3.0 dB tolerance allows δL_x as large as $123 \mu\text{m}$. This result is, of course, obtained when $\delta L_y=0$; in the radial sense from Fig. 3-32, δL_y can increase to less than $35 \mu\text{m}$ to maintain the same -0.5 dB tolerance.

For deviation in width (nominal = $30 \mu\text{m}$) shown in Fig. 3-34, symmetrical imaging has greater width tolerance than paired or general imaging. At 5×5 images, -0.5 dB symmetrical imaging loss tolerance is nearly $3.0 \mu\text{m}$ while general imaging tolerance is only about $0.70 \mu\text{m}$. The symmetrical single image -0.5 dB loss tolerance is $0.57 \mu\text{m}$ while it is only $0.14 \mu\text{m}$ for the general imaging case. Thus, as the number of images decreases, width tolerance also decreases. For -3.0 dB loss, the case of symmetrical 5×5 images produces a more relaxed width tolerance about $10 \mu\text{m}$ compared to general self-image with only $0.5 \mu\text{m}$. Symmetrical images not only offer short image distances, they also offer higher fabrication tolerances.

For the change in guide index (nominal = 1.585) shown in Fig. 3-35, symmetrical

5x5 imaging at -0.5 dB loss has an index tolerance of 0.29 while the same tolerance is 0.015 for general single images. Even at 5x5 images, general imaging allows for only a 0.05 index tolerance at -3.0 dB loss. Thus, these large guide index changes in a practical system can be neglected since they should not occur under normal conditions.



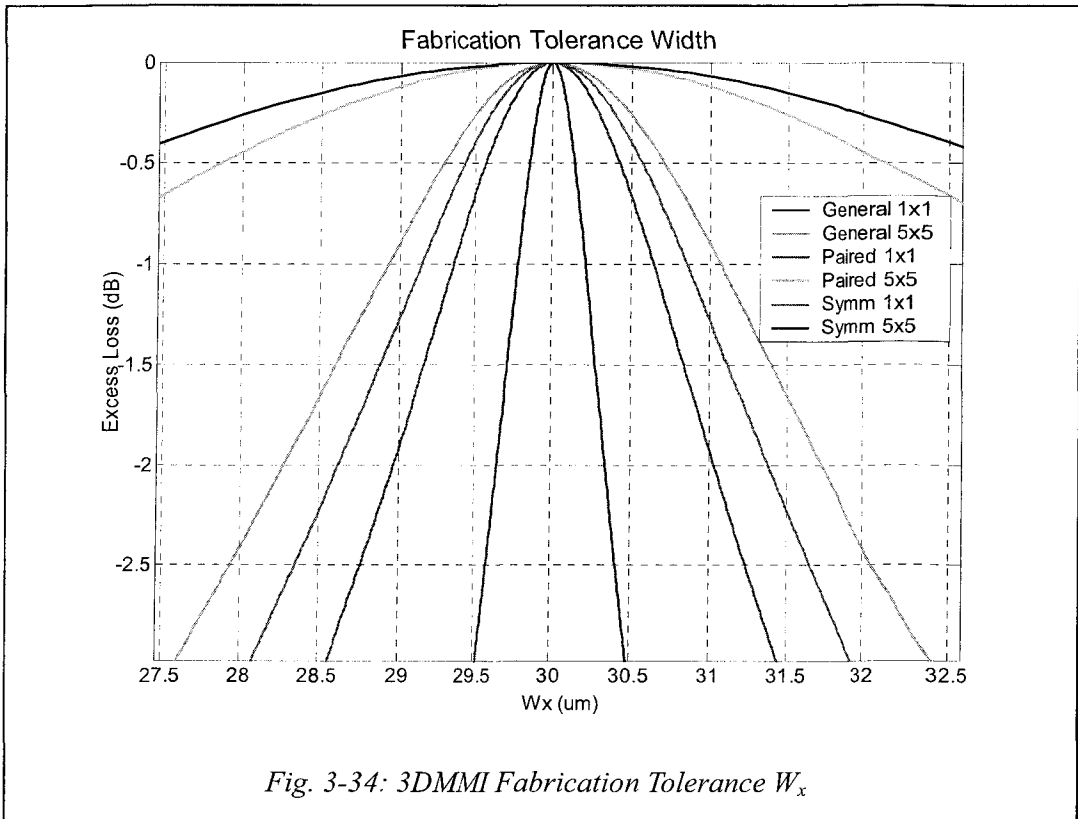


Fig. 3-34: 3DMMI Fabrication Tolerance W_x

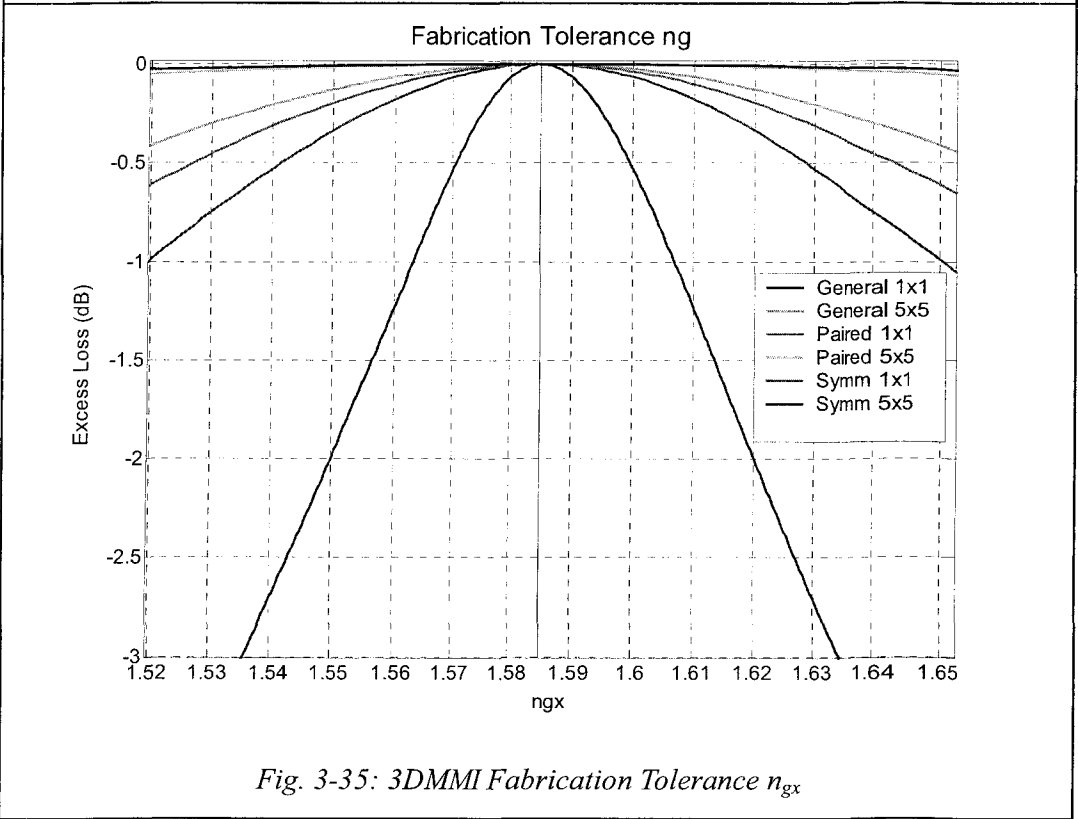


Fig. 3-35: 3DMMI Fabrication Tolerance n_{gx}

Table 3-7: Fabrication Tolerance of 3DMMI ($w_0 = 6.66 \mu\text{m}$)

3.5.2 Optical Bandwidth

Optical bandwidth represents a band of transmittable wavelength under a tolerance of EL and is simply 2 times the tolerance of $|\delta\lambda|$. This value can also be obtained with the relationship in Eq. 3.5.1. Thus, a similar plot can be generated with the three types of multiple imaging shown in Fig. 3-36. For a realistic transmission tolerance of 90% or -0.5 dB loss, symmetrical 5x5 images produces a large bandwidth of 0.57 μm around the nominal value of 1.55 μm while it is 0.14 μm for general single images. For single images, the bandwidth for symmetrical imaging is 0.11 μm and 0.03 μm for the general imaging case. For DWDM applications where channels are generally 0.8 or 1.6 nm apart, it can be concluded from these results that 3DMMI is capable of hosting a large bandwidth of transmission channels with relatively low EL.

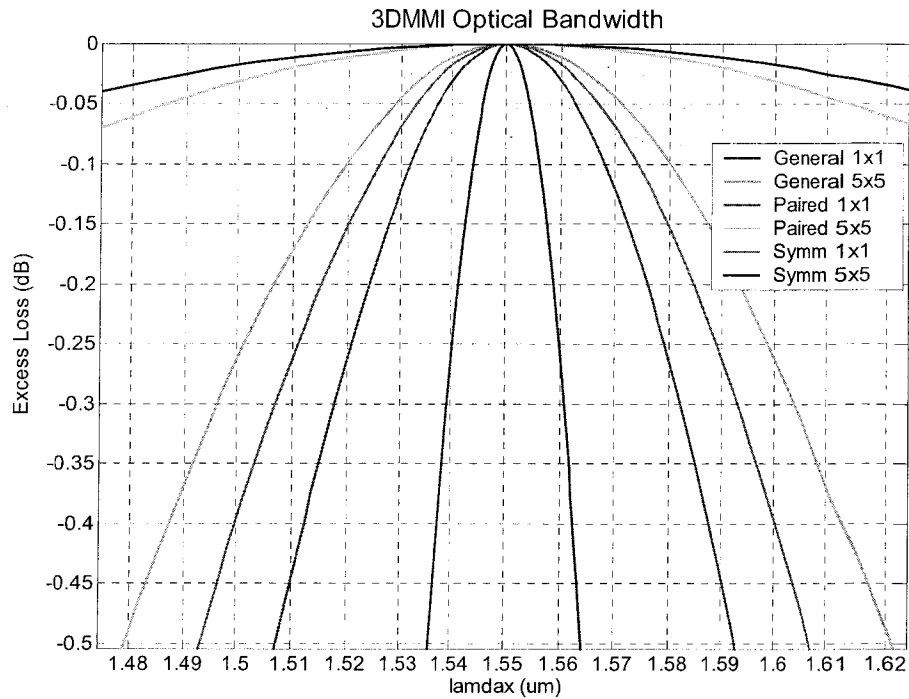


Fig. 3-36: 3DMMI Optical Bandwidth ($w_0 = 6.66\mu\text{m}$)

[4] 3DMMI Application and Design

4.1 3DMMI Applications

4.1.1 The Advantage of 3DMMI

Following the success of general MMI devices, 3DMMI analysis has shown many similar results. Mutual advantages include low image splitting imbalance, compact size, good fabrication tolerance, low polarization dependence, and great design flexibility. MMI devices generally are more efficient compared to weak synchronous couplers based on parallel waveguides and two-mode interference devices [9], [12]. These devices, including directional couplers and ring couplers, rely on the crosstalk of evanescent fields in which the power is proportional to squared sinusoids of the z distance and the beat length. Thus, power coupling efficiencies are low with high power sensitivities at length variations near the 3 dB power level. Low loss and sensitivity is an important advantage of MMI or 3DMMI devices since all available power within the guide will transfer to form images. Preferably, a 3DMMI device is fabricated for high modal confinement with high index-contrasts to reduce cladding radiation losses. The fundamental difference between MMI and 3DMMI is the extension to the third physical dimension, y . 3DMMI devices are easy to produce without complicated fabrication methods such as masking techniques, and they offer high fabrication tolerances. Not only do 3DMMI devices greatly increase the integration density, they offer additional reliability and structural stability to support guided waves [46]. The ultimate goal of 3DMMI is for light signals to route to a different stacked planar layer for two-dimensional inputs and outputs.

4.1.2 Two-Layer Devices

3DMMI offer the ability to connect between other two-layer integrated devices

with two dimensional cross-sectional signal fields. One such application of 3DMMI is for a two-dimensional input array of wavelengths for multiplexing/de-multiplexing [47]. This proposed device offers lower insertion loss and higher bandwidth for DWDM applications. Potentially, a two-dimensional array of DWDM inputs and be combined to form Very DWDM (VDWDM) outputs. There are also other types of two-layer devices such as 3DMMI switches based on partial index variations. In addition, interferometers and two-dimensional laser outputs are also desirable applications.

Two-layer routing of optical signals is the first step towards two-layer devices. Potential multilayer wiring can be achieved using 3DMMI. Vertical real estate will be important for future applications as the demand for density and bandwidth increases. Two-layer routing can also be applied to bio-applications such as micro-fluidics [48] where light can be utilized to excite biological samples. By introducing 3DMMI two-layer routing, layers of micro-channels can potentially be realized in a stacked structure. Vertical real estate is thus utilized more efficiently with higher throughput and density. By utilizing the vertical direction for imaging, two-layer signal routing promises the evolution of current planar integrated devices.

4.2 3DMMI 2-Layer Routing

Rectangular 3DMMI devices that demonstrate general, symmetrical, and paired interference imaging can be easily designed based on the analysis of Chapter 3. A novel feature for 3DMMI is the ability to route optical signals to another vertical layer of channels. This idea can be defined as 3DMMI 2-Layer Routing (3DMMI-2LR) where the input signal is mirrored to the output layer. Generally, there is an input and an output waveguide prior and after a main 3DMMI routing section illustrated by Fig. 4-1. The transverse cross-sectional heights or widths of the input and output waveguides do not have to be the same. In addition, the ratio of the 3DMMI routing section height with the input and output waveguide heights may also be different.

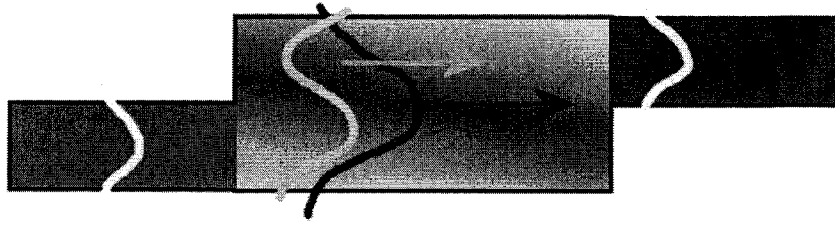


Fig. 4-1: Schematic of 3DMMI-2LR

Two ranges of 3DMMI-2LR dimensions are covered in this thesis, one being of the 50 μm range, and one being in the 3 μm range. Surrounding the waveguides and the main 3DMMI section in Fig. 4-1 is the cladding material and that the guide index is kept the same. Let us assume that the width of the 3DMMI section is the same as the widths of the input and the output waveguides for simplicity.

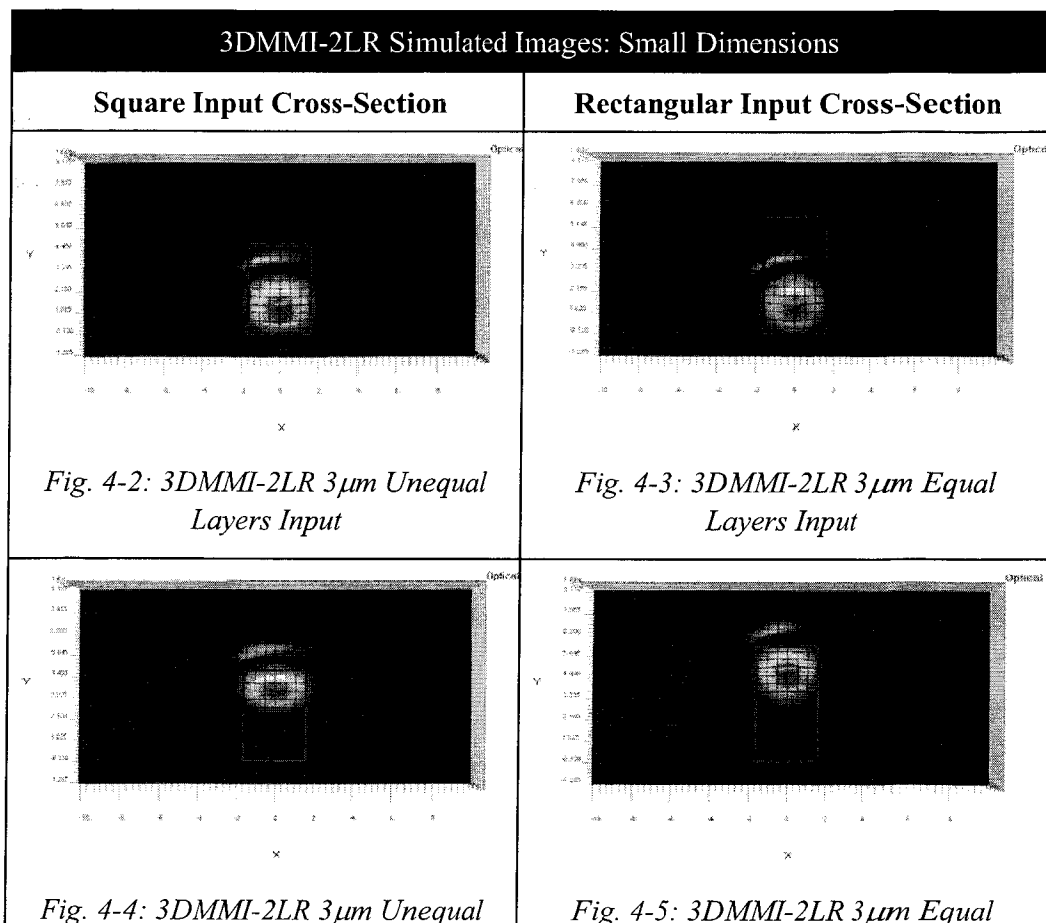
Small Dimensions: 3 μm

Two-layer routing in a 3DMMI section reflects the idea of mirroring across the x-axis. For general interference, only when $\Delta_x = \Delta_y = 1$ will mirroring occur with a constant device width. One possibility for general interference is to have a square input waveguide for improved symmetry. The disadvantage of such a design limits the top layer to a different height compared to the bottom layer. The other possibility for general interference is to have equal top and bottom layer heights. In this case, the top and bottom layers can be fabricated with the same process procedure. Using $\lambda_0 = 1.55 \mu\text{m}$, $\text{HW} = 3.33 \mu\text{m}$, $n_g = 1.585$, $n_c = 1.52$, general mirroring 3DMMI structures are simulated with the calculated dimensions from Table 4-1. The input and output waveguides are two-dimensional waveguides, so symmetrical self-imaging still holds. Generally, the distance between two consecutive self-images is much lower compared to larger guides. If the input MFD is wider than these waveguides, images other than self-images will not appear. Thus, the length of the input and output waveguides can be chosen in a wide range of possibilities. For the unequal layers case, the input waveguide length was chosen at 58 multiple of the beat length of 17.175 μm .

3DMMI-2LR Small Dimensions Design		
	Unequal Layers	Equal Layers
Input cross-section ($\mu\text{m} \times \mu\text{m}$)	3 x 3	3.921 x 3
Input length (μm)	996	17.175
Mirroring cross-section ($\mu\text{m} \times \mu\text{m}$)	3 x 4.7	3.921 x 6
Mirroring length (μm)	137.4	206.1
Output cross-section ($\mu\text{m} \times \mu\text{m}$)	3 x 1.7	3.921 x 3
Output length (μm)	996	17.175

Table 4-1: 3DMMI-2LR Small Dimensions Design

This magnitude was chosen to obtain an input waveguide length of about 1000 μm for practical applications and to see the effect of long lengths. For equal layers, only one multiple of the beat length was chosen for the input and output wavelengths. Table 4-2 shows the simulated images of 2-layer routing with small dimensions.



<i>Layers Output</i>	<i>Layers Output</i>
----------------------	----------------------

Table 4-2: 3DMMI-2LR Simulated Images-Small Dimensions

From the above figures, 2-layer routing is successful in both cases. For the equal layers case, the shape of the original image is maintained in contrast to the y-compressed output from the unequal layers case. An important observation is that the peaks of the output mirrored images lie at exactly the designed cross-sectional output location. Table 4-3 summarizes the power loss compared to the original input for the two designs.

Power Loss of 3DMMI-2LR Small Dimensions		
End of...	Square Input Cross-Section	Rectangular Input Cross-Section
Input waveguide	-1.82dB	-0.04dB
3DMMI section	-1.82dB	-0.59dB
Output waveguide	-2.46dB	-0.63dB

Table 4-3: Power Loss of 3DMMI-2LR for Small Dimensions

Table 4-3 indicates that major power loss occurs from the large $HW=3.33 \mu\text{m}$ input coupling into the input waveguide. Negligible loss occurs in the 3DMMI section itself and the extra loss at the end of the device is due to coupling to the output waveguide, which only covers about 60% of the field from the end of the 3DMMI. In addition, rectangular input cross-section or the equal layers design showed the lowest loss. For one thing, the input waveguide's length is reduced. The considerable loss in the 3DMMI section indicates that the mirrored image does not hold all of the power. Intuitively, since the transverse dimensions of the device is small, a $HW=3.33 \mu\text{m}$ initial Gaussian field has considerable power spanning in both layers in the 3DMMI routing section. In addition, the GH shift generates a large ratio of width deviations compared to the physical width causing deeper cladding penetration. Hence, power loss is evident. Nonetheless, the rectangular equal layers two-layer router is a good design.

Large Dimensions: 50 μm

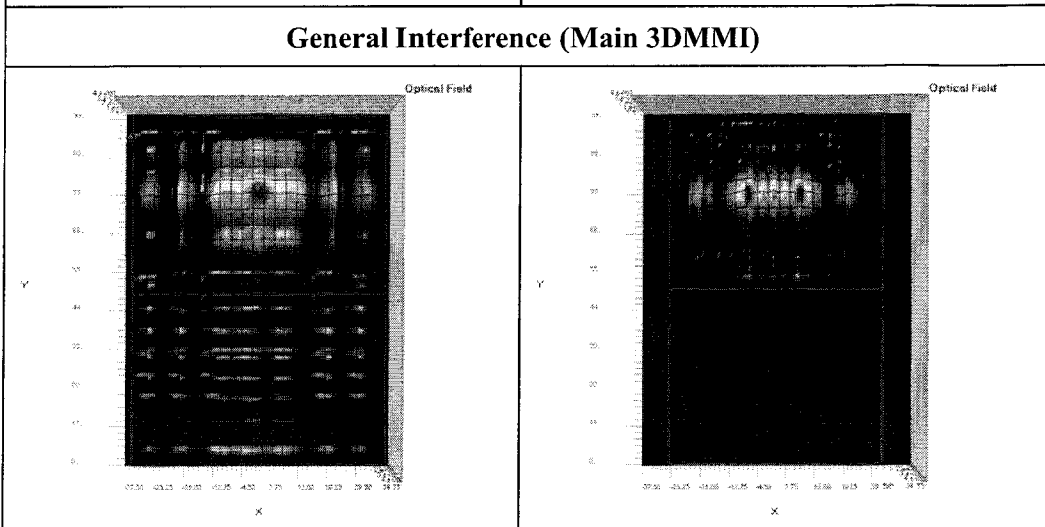
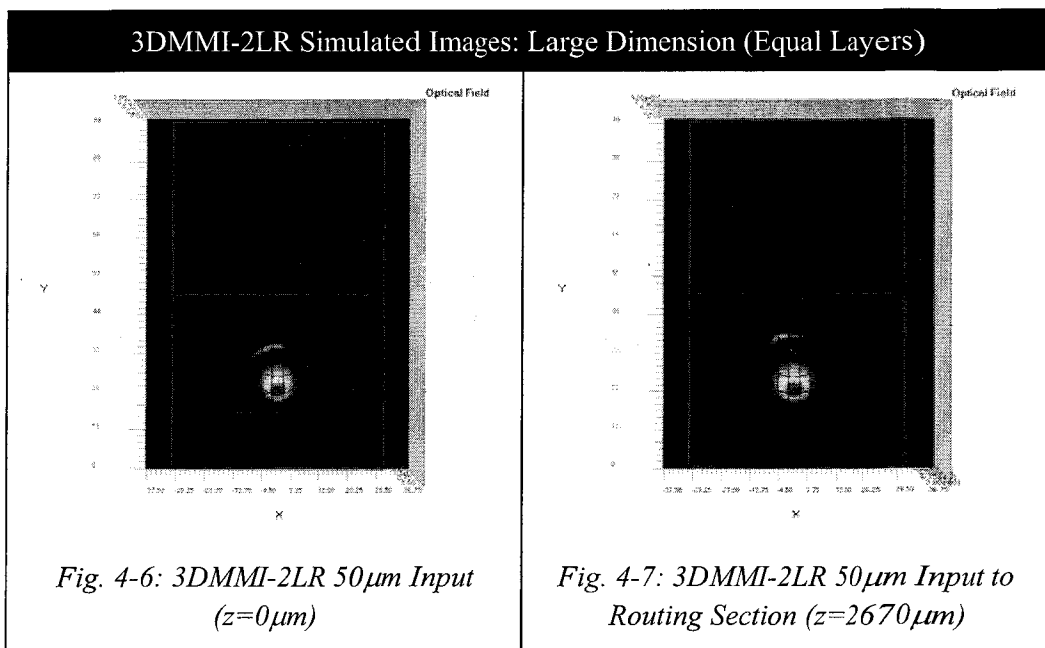
In large dimensions, 2-layer routing methods are slightly different from devices in smaller dimensions. In terms of fabrication, large dimensions are also easier to manage. Input and output waveguide cross-sections are now dramatically increased in size causing very large distances between consecutive self-images. Input and output waveguide lengths are now crucial for proper device behavior. If the self-images in the input and output waveguides are achieved with general interference, the lengths would easily exceed 2 cm, which are not desirable. In addition, the main 3DMMI routing section would exceed over 4 cm. Thus, self-imaging should be achieved using symmetrical-XY inference, meaning that all input and output waveguides should have a square cross-section. In terms of the main 3DMMI section, symmetric-X interference can also be adopted for mirroring with shorter lengths compared to general interference. The two cases of routing are still equal and unequal heights of the bottom and the top layers. Using $\lambda_0 = 1.55 \mu\text{m}$, $\text{HW}=3.33 \mu\text{m}$, $n_g=1.585$, and $n_c=1.52$, general and symmetric-X mirroring 3DMMI structures are simulated with the parameters from Table 4-4.

3DMMI-2LR Large Dimensions Design			
	Unequal Layers	Equal Layers (General)	Equal Layers (Symmetric-X)
Input cross-section ($\mu\text{m} \times \mu\text{m}$)	50 x 50	50 x 50	50 x 50
Input length (μm)	2670	2670	2670
Mirroring cross-section ($\mu\text{m} \times \mu\text{m}$)	50 x 71.166	70.389 x 100	70.389 x 100
Mirroring length (μm)	21360	41806.8	10451.7
Output cross-section ($\mu\text{m} \times \mu\text{m}$)	21.166 x 21.166	50 x 50	50 x 50
Output length (μm)	506.89	2670	2670

Table 4-4: 3DMMI-2LR Large Dimensions Design

In the unequal layers case, the problem is how much of the mirrored image power couples into the output waveguide. Calculation shows that the mirrored image will

center at $y = 46.166\mu\text{m}$. This indicates that the peak of the mirrored image does not lie in the cross-sectional area of the output waveguide. Less than 30% of the power will couple into the output waveguide with a distorted self-image at the output. This result suggests that 2-layer routing using equal layers is the better design. In that case, images are maintained at the symmetrical center of the top or bottom layers. The only disadvantages are increased general interference mirroring lengths and increased widths at the central region. Table 4-5 shows the simulated images of 2-layer routing with equal layer heights. The main 3DMMI routing section is simulated with general interference and symmetric-X interference.



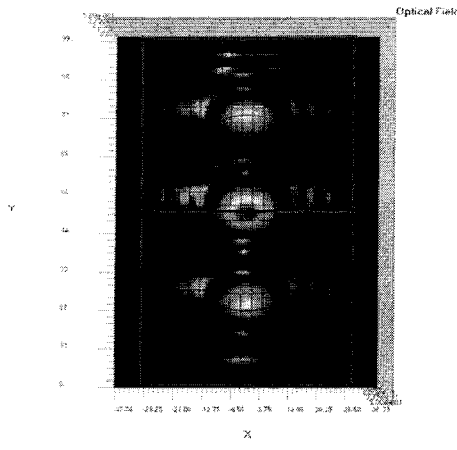
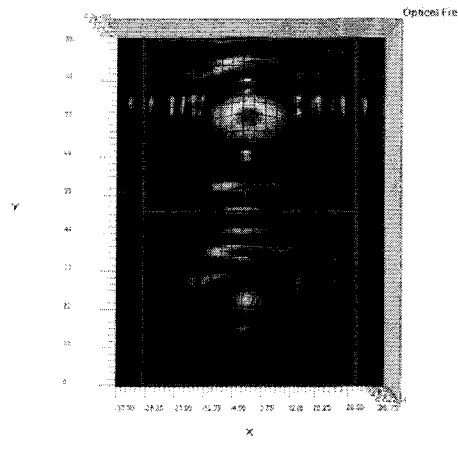
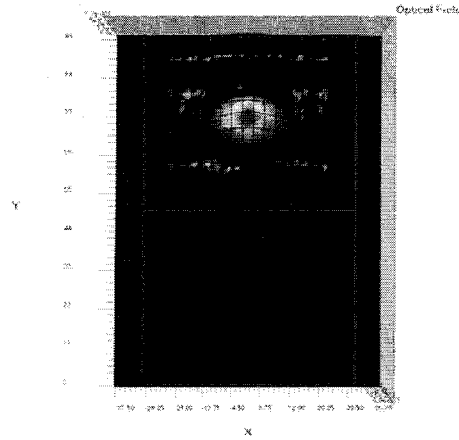
<p><i>Fig. 4-8: 3DMMI-2LR 50μm General Interference Routed Field ($z=44476.8\mu$m)</i></p>	<p><i>Fig. 4-9: 3DMMI-2LR 50μm General Interference Output from Waveguide ($z=47146.8\mu$m)</i></p>
<p>Symmetric Interference (Main 3DMMI)</p>	
 <p><i>Fig. 4-10: 3DMMI-2LR 50μm Symmetric-X Interference Routed Field ($z=7895.85\mu$m, $\Delta_x=1$)</i></p>	 <p><i>Fig. 4-11: 3DMMI-2LR 50μm Symmetric-X Interference Routed Field ($z=13121.7\mu$m, $\Delta_x=2$)</i></p>
 <p><i>Fig. 4-12: 3DMMI-2LR 50μm Symmetric-X Interference Output from Waveguide ($z=15791.7\mu$m)</i></p>	

Table 4-5: 3DMMI-2LR Simulated Images-Large Dimensions

The behavior of the input and self-image prior to the main 3DMMI section is the same for the above two simulated cases. For general interference, mirroring occurs at over 4 cm and Fig. 4-8 shows poor image reconstruction. Thus, the self-image at the output of the waveguide in Fig. 4-9 cannot be an improved image of Fig. 4-8. That is

to say, the output self-image becomes more unlike the original input. Surprisingly, there is no power loss in this device. It can be concluded that this device exhibits high performance power confinement and mirroring. Despite this advantage, the image is distorted and the device length is very long. As shown in Chapter 2, symmetric-X interference allows mirroring with reduced length but with incomplete transfer of power shown in Fig. 2-20. In the case of large dimensions 3DMMI-2LR, symmetric-X interference actually becomes the best design with minimal power reduction. Fig. 4-10 illustrates the routed field when $\Delta_x = 1$ and Fig. 4-11 illustrates the routed field at $\Delta_x = 2$. The majority of the power can be routed to the upper layer when $\Delta_x=2$ with a small residue field in the lower layer. However, a very well constructed self-image in Fig. 4-12 is then achieved at the end of the output waveguide with a -0.40 dB power loss from the original input. That is to say, the residual field left in the lower layer has approximately 0.40 dB of power. Because we have about 91% power transmission from the input, large dimension and short distance 3DMMI-2LR has been realized successfully.

[5] 3DMMI Fabrication

5.1 Introduction

The fabrication of 3DMMI was completed with planar processes. For the demonstration of 3DMMI behaviors, general and symmetrical interferences were studied with thick (50 μm range) rectangular waveguides. In terms of the core of the waveguide, SU-8 negative tone photoresist was chosen. The type of substrate was glass and the cladding layer was air or the UV-15 optical adhesive.

5.2 The SU-8 Polymer

5.2.1 Optical Polymers

Synthetic polymers have a number of useful properties for optical waveguides including low optical losses (<1.0 dB/cm), high thermal stability after curing, low polarization dependence, high mechanical flexibility, high physical stability, ease of fabrication and processing, and low costs [49] [32]. Some of these polymers are used mainly as photoresists for patterning integrated structures. In general, these polymers can be exposed to actinic radiation such as Ultraviolet (UV) or electron-beam to crosslink the monomers. By blending and copolymerizing selected monomers with additives, these synthetic materials can be tailored with a broad range of refractive indices from 1.3-1.6 [32]. Based on carbon bonds with H, F, O, and other elements, absorption loss can also be tailored at specific resonance wavelengths.

5.2.2 Properties of SU-8

The polymer chosen for the core of the waveguide in this thesis is the SU-8 epoxy

resist. This photoresist is a negative tone photoresist initially formulated for micromachining and microelectronics applications. It is a thick (generally 1 to 200 μm), high contrast, thermally stable, and chemically stable material after processing [50-51]. Because of its high optical transparency above the wavelength of 360nm, high aspect ratio vertical sidewalls can be achieved with UV excitation mainly at the I-Line (365nm). SU-8 was originally developed and patented by IBM-Watson Research Centre in 1989. After 1996, this material was adopted for Micro-Electro-Mechanical Systems (MEMS) applications [50]. Since then, SU-8 has been applied for the realization of integrated optical waveguides with many property improvements such as decreased drying time, improved coating, various thicknesses [52], higher aspect ratio, and increased stability [53]. Important properties of the SU-8 polymer are given below:

SU-8 Physical Properties	
Glass Transition Temp. [51]	$T_g \sim 200^\circ\text{C}$ (fully crosslinked film or hard baked) $T_g \sim 50^\circ\text{C}$ (unexposed film or not polymerized)
Degradation Temp. [51]	$T_d \sim 380^\circ\text{C}$ (fully crosslinked film or hard baked)
SU-8 Optical Properties	
Index of Refraction [51]	1.575 (1550nm) 1.580 (840nm) 1.596 (633nm, crosslinked) 1.67 (408nm, not crosslinked)
Propagation Loss [54]	3.00dB/cm (1550nm) 5.00dB/cm (1450nm) 0.75dB/cm (1310nm) 3.25dB/cm (1200nm) 0.50dB/cm (980nm) 2.00dB/cm (670nm)

Table 5-1: Physical and Optical Properties of SU-8 Photoresist

From Table 5-1, high T_g after crosslinking indicates that SU-8 is thermally stable and is in glass stage below 200°C . This temperature gives SU-8 a large temperature range for normal operations. Its thermal stability property is reinforced with T_d of greater than 380°C . The SU-8 transmission index of refraction varies from 1.575 at 1550 nm near infrared to about 1.6 at the visible wavelength of 633nm. SU-8 exhibits high

propagation losses at 600 nm, around 1200 nm, and from 1400–1600 nm [54]. Since the SU-8 polymer contains C-O, C-H, C-C, and C=C bonds [50], characteristic infrared absorption can be used to verify this behavior [55]. High losses at 600 nm are mainly due to the strong harmonic absorption of the C-H alkane. The high losses at around 1200 nm is mainly due to the aromatic ring bonds of C=C. Between 1400–1600 nm, the behavior is due to the mixed strong harmonic absorption of C=C and C-H bonds.

Crosslinking for SU-8 begins with the exposure of SU-8 to radiation. SU-8 structures can be fabricated using methods such as direct laser writing [56], ion beam etching [57], plasma etching [58], x-ray lithography [59], and conventional UV lamp lithography. Structures with direct laser writing are usually not smooth; depending on the speed of the laser write, crosslinking is weakened if baking is not performed immediately after. Ion beam and plasma etching involve elaborate gases, material, and tools to pattern and remove fully crosslinked SU-8 films. So far, these two processes are relatively expensive and are only capable of producing structural heights of only a few microns. In addition, sidewalls are usually slightly off 90°. X-ray lithography is also an elaborate method of patterning SU-8 such as with synchrotron x-rays and they usually require relatively higher exposure energies. The most simple, inexpensive, and relatively uniform method for the patterning of SU-8 is a conventional UV lamp. In this case, the preferred exposure wavelength is the I-line at 365 nm.

5.2.3 Existing SU-8 Optical Waveguides and Structures

SU-8 waveguides have been around for a decade and they have been chosen for their ease of fabrication, excellent properties, and design flexibilities. Single mode SU-8 waveguides can be used to transmit a wavelength of 800 nm with a very low propagation loss of 0.25 dB/cm [60]. These low losses suggest the possibility for SU-8 to be applied to sensors and optical backplane applications. The width and height of the SU-8 waveguide were 4 μm and 2 μm respectively. SU-8 waveguides

can also be utilized as cores for active and passive micro-ring resonators [61]. In this case, filters, modulators, and lasers can be realized. In fact, regions of SU-8 waveguides can also be doped with laser dyes such as Rhodamine 6G to produce possible gratings and filters for internal resonance [62]. The refractive index of SU-8 can be changed by 0.002 with a concentration of only 4 $\mu\text{mol/g}$ of this dye.

Due to the smooth, high contrast, and high aspect ratio profile of SU-8 structures, it is an excellent material for MEMS, microfluidics, and as an optical cladding. In terms of MEMS, SU-8 was originally developed for this type of application. SU-8 is a good material for realizing high pillars [63, 64] and deep trenches [65]. In terms of microfluidics, SU-8 can be fabricated to guide light into microchannels [66] or act as the structure surrounding these channels [67]. Structurally, SU-8 is a good cladding material that can surround a variety of cores. For example, large circular trenches of SU-8 can support circular Polymer Optical Fiber (POF) to capture vertical light emissions from VCSEL arrays [68].

For the purpose of this thesis, large dimension (50 μm range) SU-8 waveguides are the focus. These types of waveguides have already been demonstrated to transmit multimode optical signals. SU-8 can be fabricated on borosilicate with PMMA (polymethyl-methacrylate) as the surrounding cladding material. Large structures (40x40 μm^2) can be realized to transmit multimode light for 1xN power splitters and NxN star couples [54]. The excess loss is relatively high for these devices because three-dimensional multimode interference was not considered in the design. Recently, 50x50 μm^2 SU-8 waveguides have been fabricated with relatively low propagation loss of less than 0.4 dB/cm at a wavelength of 830 nm [69]. Large size SU-8 waveguides are also being considered for the application for three-color-mixing (red, green, blue) in projection display techniques [70]. SU-8 waveguides may be easily fabricated on glass substrates since its refractive index is already lower than that of SU-8. Glass substrates eliminate the need to have cladding layers or oxide layers between SU-8 and traditional silicon substrates. SU-8 structures adhere better on glass with an initial adhesion promoter [71] such as Omnicoat [72] produced by MicroChem. For SU-8 structures, exposure dose, diffraction, reflection, and air gaps

are significant factors affecting their vertical profiles [73]. In most cases, it is important to reduce tapering from the top to the bottom of SU-8 structures. In practice, significant effects from the above factors can be reduced by placing an index matching material between the patterning mask and the unexposed SU-8 film such as glycerol [74]. Usually, the exposure of SU-8 films with UV lamps contains wavelengths below 365 nm. SU-8 strongly absorbs wavelengths shorter than 350 nm at the surface of the film; thus, a lateral diffusion of the generated acids will cause T-topping, or the tapering of the SU-8 structure from the top to the bottom [75]. To minimize this problem, a UV filter can be placed between the radiation source and the SU-8 film to reduce wavelengths below 350 nm. This method is part of the general process of fabricating SU-8 waveguides.

5.3 3DMMI Fabrication Process and Results

5.3.1 General Fabrication Process

The general fabrication process is schematically illustrated below in Fig. 5-1. The formula of SU-8 used for large size structures is SU-8 2050 developed by MicroChem [76]. The cladding material chosen is UV-15 optical adhesive developed by Masterbond [77]. First, glass wafers can be cleaned using the piranha ($\text{H}_2\text{SO}_4 : \text{H}_2\text{O}_2$) acidic etch/clean solution. Prior to applying uncured SU-8, a thin layer of Omnicoat must be spun-on to improve adhesion to glass.

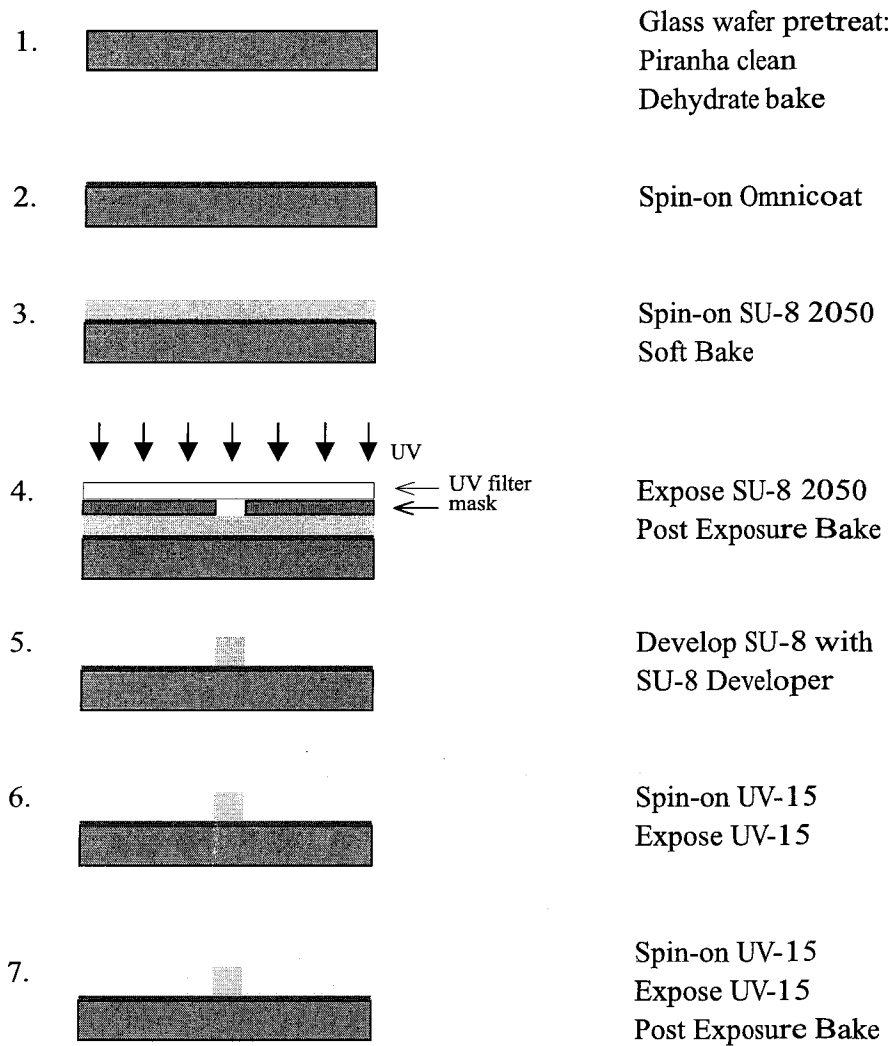


Fig. 5-1: Generalized 3DMMI Fabrication Process Procedures

A hotplate Soft Bake (SB) is then performed to evaporate the SU-8 solvent material known as cyclopentanone (c.p.). Since SU-8 is sensitive to thermal stress prior to crosslink [50], a lower temperature of 65°C is required to expel the solvents while a temperature of 95°C for crosslinking must be reached with a slow ramp. With a two-temperature SB process, the evaporation of the SU-8 solvent occurs at a more controlled rate. This method increases the coating fidelity, reduces edge bead, and improves adhesion to the substrate [76].

As mentioned before, SU-8 strongly absorbs energies of wavelengths below 350

nm. This is demonstrated by MicroChem in the wavelength absorbance analysis of Fig. 5-2(a). The exposure energy requirement for varying film thickness is given by Fig. 5-2(b).

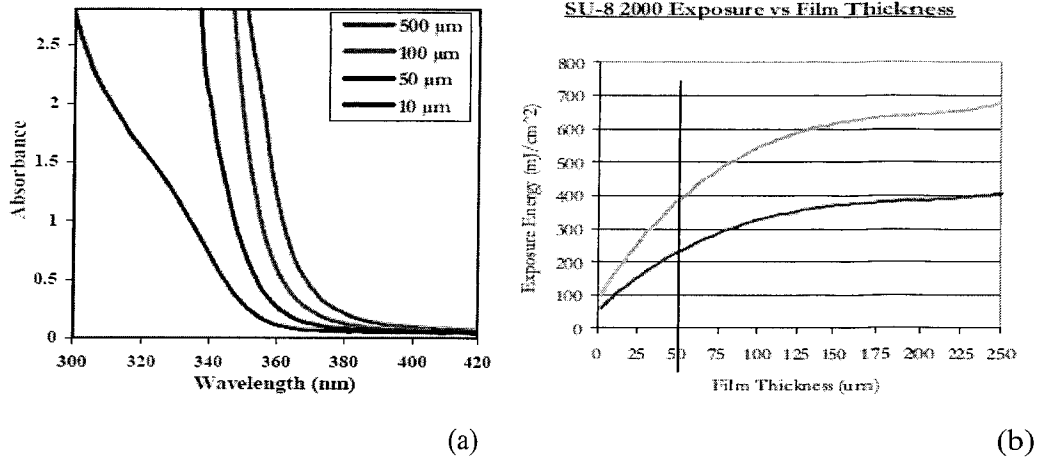


Fig. 5-2: (a) Wavelength Absorbance of SU-8 with Given Thickness, (b) SU-8 Film Exposure Energy Requirements [Ref. 76: MicroChem SU-8 2000 Reference Sheet]

For 50 μm SU-8 thickness, the absorbance is increased drastically below the wavelength of 350 nm from Fig. 5-2(a). The two colored lines from Fig. 5-2(b) are from measurements of the I-line radiometer and probe. Typically, with a broad spectral output source, as in the case of most UV-lamps, adhesion can be improved with 25% or more dosage. Because of the reduced reflective property of glass as compared to silicon substrates, 30-40% higher dosage is required for glass as indicated by MicroChem. During the exposure, UV filtering is achieved using the Kopp 7380 glass [78], which has the following UV transmission characteristics:

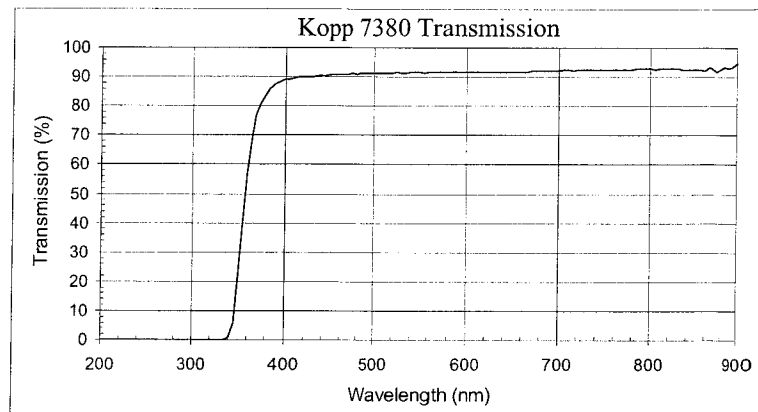


Fig. 5-3: Kopp 7380 UV Filter Wavelength Transmission [Ref. 78: Kopp Glass]

From Fig. 5-3, the transmission at 365 nm is about 70% while it is less than 20% at 350 nm, and less than 1% at wavelengths less than 340 nm. Thus, SU-8 dosage must again be increased by about 40%. The final required radiation dosage for SU-8 is calculated to be at least 1000 mJ/cm².

After exposure, a Post Exposure Bake (PEB) is required immediately to avoid relaxation of the crosslink initiated by the radiation. Similar to SB, PEB must also be completed with the two-temperature ramp process. In this case, the time required at 65°C is less than SB, but an increased time will improve crosslink and adhesion. After PEB and a relaxation time, SU-8 can be developed using MicroChem's SU-8 Developer [79] with a medium-to-strong agitation rate. From experimentation, overly strong agitation will lift the SU-8 structures and weak agitation will not allow for a clean develop. Thus, agitation rate is a strong factor for well-developed SU-8 structures. After isopropyl alcohol rinsing and nitrogen drying of the SU-8 developer, a hard bake can be performed optionally to reduce moisture and further crosslinking. The detailed SU-8 processing procedure is included in Appendix B with some process detailed attained from MicroChem representatives and in the MEMS Exchange Forum [80].

The Master Bond UV-15 optical adhesive is the cladding material applied around the SU-8 core because of its ease of processing, and lower index of refraction. UV-15 is difficult to spin to a thickness of greater than 35 μm [81], but the planarization of SU-8 from process procedure 6 of Fig. 5-1 can be realized experimentally with a very slow spin rate of 500 rpm. UV-15 can be easily cured by the I-line without the need for baking. A baking process can be completed to increase its service temperature to 150°C. Glass substrates should be at a dehydration temperature of 100°C for improved UV-15 adhesion. Generally, UV-15 can be spun on before the glass substrate reaches room temperature. Further adhesion can also be achieved with the application of adhesion promoters or silicone primers [77].

5.3.2 Fabrication Process Results

Generally, SU-8 spin-speed, baking time, exposure intensity, UV-filtering, develop rate, and cladding planarization are a few of the most important factors that determine the successful fabrication of these 3DMMI devices. The following sections will illustrate the fabricated results from varying some of these factors.

SU-8 Waveguide Width and T-Topping

T-topping can be easily observed for SU-8 structure cross-sections where the width is varied from 10-50 μm with a set height of $\sim 50 \mu\text{m}$. Fig. 5-4 illustrates this observation due to the broadband nature of the I-line UV lamp.

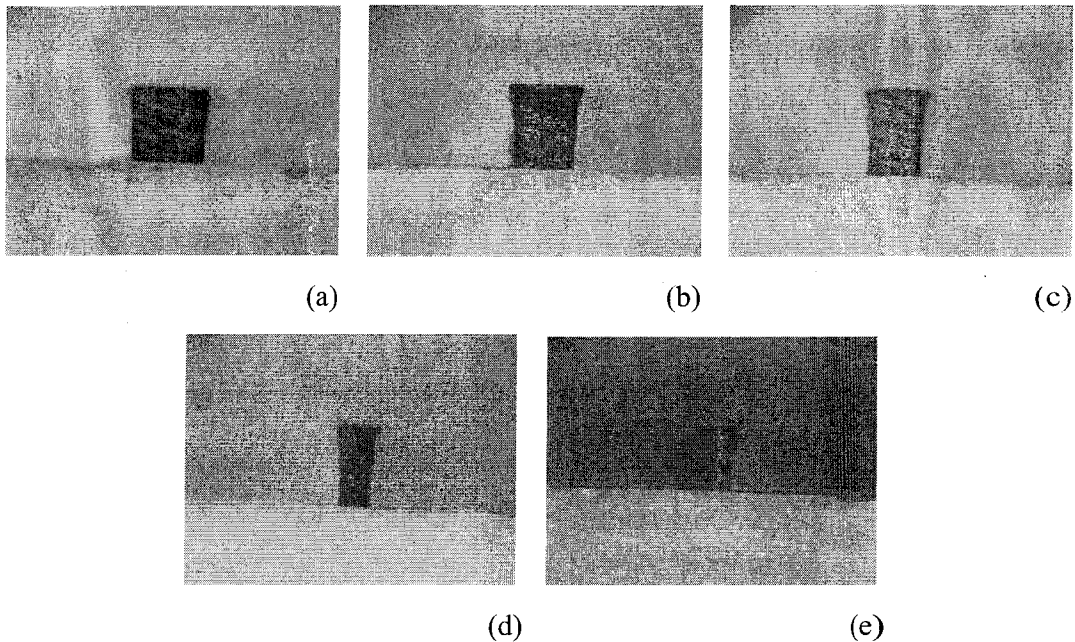


Fig. 5-4: SU-8 T-Topping with Widths (a) 50 μm , (b) 40 μm , (c) 30 μm , (d) 20 μm , (e) 10 μm

From Fig. 5-4, T-topping is more apparent and more significant as the width/height ratio decreases. Since actual devices are 50 μm in width, this effect is not as apparent in Fig. 5-4(a). However, under the Scanning Electron Microscope (SEM), T-topping is actually very noticeable with the 50x50 μm^2 cross sectional structure depicted in Fig. 5-5.

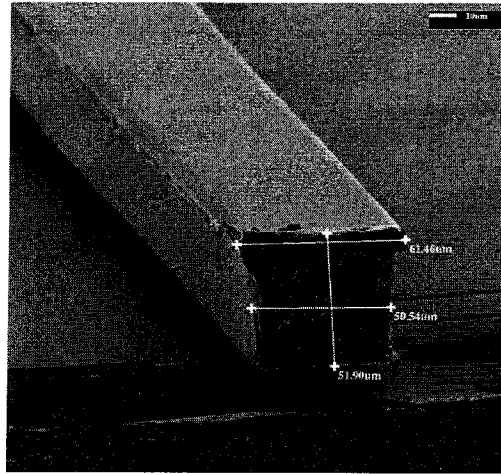


Fig. 5-5: SEM End View of SU-8 50x50 μm^2 Cross-Section

Because of the T-topping result, UV-filtering becomes crucial. As mentioned previously, glycerol can be used as an index matching material to reduce the gap between the mask and the sample during exposure. This material can be replaced by a similar material, ethylene glycol, to help reduce T-topping [75]. Fig. 5-6 shows the resulting waveguides exposed with (b) and without (a) ethylene glycol where the square borders represent the ideal shape.

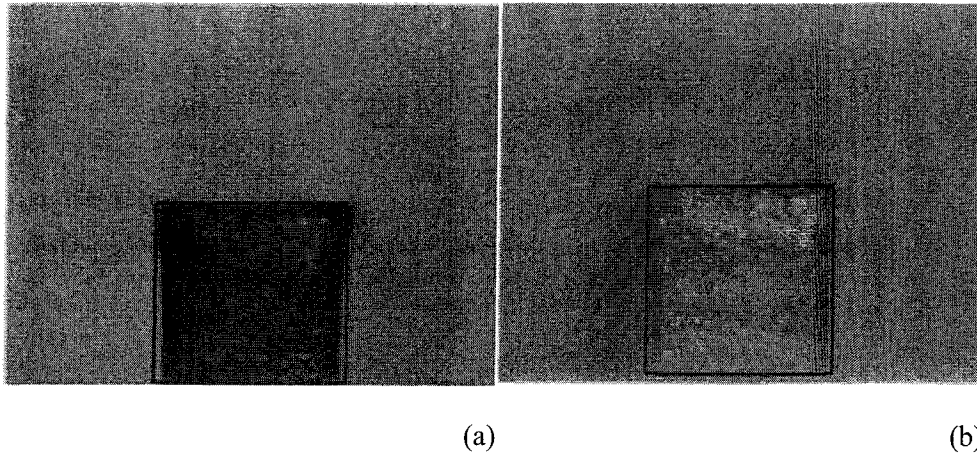


Fig. 5-6: The Effects of T-Topping on 50x50 μm^2 Waveguides (a) Without Ethylene Glycol, (b) With Ethylene Glycol

In both cases, the undercut is approximately 5% of the ideal width measured at the bottom of the waveguides. This means that the bottom gap is approximately 2-2.5 μm on both sides of the waveguide. Some fabricated end views have even higher gap

sizes due to greater top surface acidic flow during the exposure. No appreciable difference in gap occurs in the case with or without ethylene glycol. In fact, this result indicates that the effects of T-topping rely more on the inability to reduce low exposure wavelengths than air gap between the mask and the sample. In addition, the low effect of applying ethylene glycol indicates that the small air gap between the sample and the mask is tolerable.

UV-15 Cladding Material

The Master Bond UV-15 optical adhesive is easy to process with simply a spin-on step and crosslinking with UV radiation and some post-baking. UV-15 was chosen mainly because of its excellent refractive index contrast ($n_c = 1.51 @ \lambda_0 = 1550 \text{ nm}$) compared to SU-8. In addition, UV-15 has operation temperatures up to 150°C with water-resistance and chemical stability. Unlike a similar product, Norland Optical Adhesive NOA-65 [82], UV-15 can withstand a water-cooled diamond saw for dicing substrates. Another advantage of UV-15 is that structural planarization and overfill can be achieved. For 3DMMI structures, UV-15 can be tailored to fill over the SU-8 waveguide. UV-15 could also be applied on to the substrate prior to SU-8 to form a total enclosure. However, since the change in the glass substrate index compared to UV-15 can be neglected for 3DMMI imaging, an initial layer is not required. UV-15 fill is shown in Fig. 5-7 with the square waveguide cores.

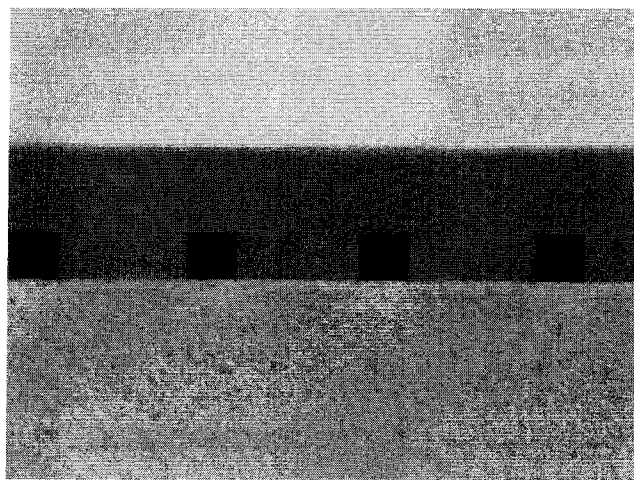


Fig. 5-7: Filled UV-15 Cladding with $50 \times 50 \mu\text{m}^2$ SU-8 Waveguides

One-Layer 3DMMI Structures

Following the steps from Fig. 5-1, one-layer 3DMMI can be realized with device end dicing at correct lengths. SU-8 is not physically stable under the pressure of water and a spinning blade; thus, a protection layer is required on top of the SU-8 such as UV-15 or a removable photoresist. The square end-view shape of these SU-8 waveguides can be seen in Fig. 5-7 with a $\pm 1 \mu\text{m}$ and $\pm 2 \mu\text{m}$ deviation from $50 \mu\text{m}$ in the width and the height respectively. The final waveguides were fabricated with UV exposure through the Kopp 7380 low wavelength optical filter such that the bottom gap of T-topping was less than 1% according to the previous method. The SU-8 and UV-15 indices of refraction change with wavelength. At 1550 nm, the indices are 1.577 and 1.502 for SU-8 and UV-15 respectively. At 980 nm, these values are 1.595 and 1.513 respectively. Although small variations in the indices have little effect on the image length, these different indices were considered in the actual design. Fig. 5-8 shows the resulting cut features of similar $50 \times 50 \mu\text{m}^2$ SU-8 waveguides.

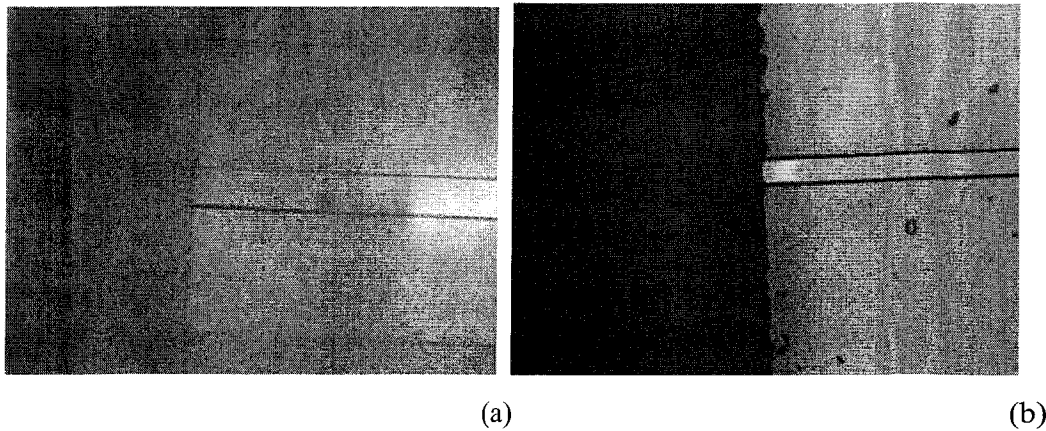


Fig. 5-8: Top-view of SU-8 cuts (a) with UV-15 fill (b) with removable photoresist

Fabricated 3DMMI structures have good end-view cut features, good vertical smooth sidewalls, and good dimensions within $\pm 5 \mu\text{m}$ of width and height. The cut lengths were designed and written onto the mask from theoretical values.

Two-Layer 3DMMI Structures

Following up to step 6 in Fig. 5-1, a second layer of SU-8 can be directly spun on

the planarized lower SU-8 layer. Thus, steps 3-5 can be repeated with the second layer SU-8 crosslinked by aligning the mask-shifted features on to the first layer SU-8 as shown in Fig. 5-9. The resulting two-layer structure is illustrated in Fig. 5-10. After the second layer of SU-8 is aligned and exposed, UV-15 is again filled on top to cover the entire second layer. Cutting of this structure is identical to that of one-layer 3DMMI. The only fabrication issue for 3DMMI-2LR is the ability to align the top layer SU-8 to the bottom layer. Manual alignment has been completed so far, but it may be improved using advanced computer alignment technology unavailable to this research.

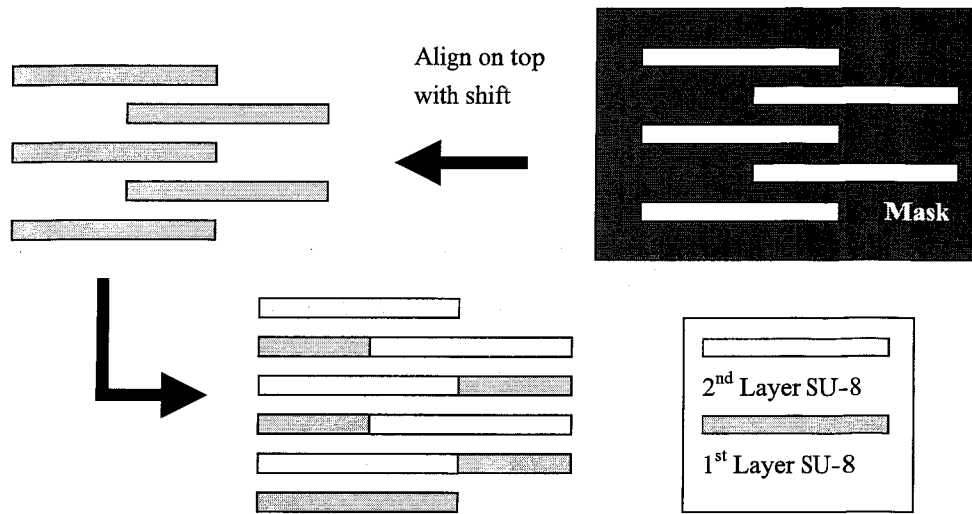


Fig. 5-9: 3DMMI-2LR Mask Lithography Technique

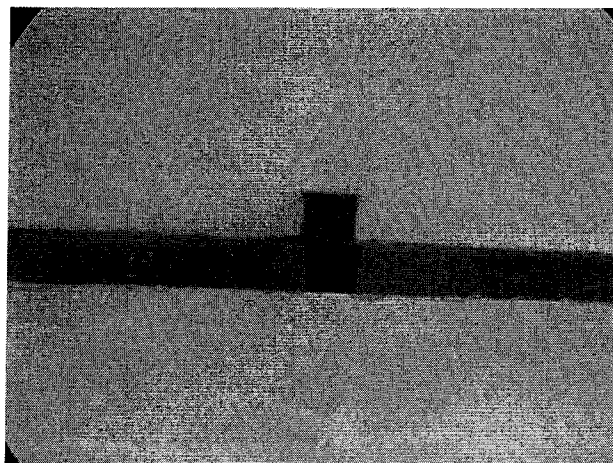


Fig. 5-10: 2DMMI-2LR Section End-View ($50 \times 100 \mu\text{m}^2$)

Summary of Fabricated Devices

To demonstrate 3DMMI imaging, the following final devices were diced:

- 1x1 Symmetric @ 1550 nm
- 2x2 Symmetric @ 980 nm
- 2x2 General @ 980 nm
- 3x3 Symmetric @ 1550 nm
- 2-Layer 100 μm height device

Due to the large number of possible interference effects, only the symmetric and general imaging devices were characterized. Since the focus was on symmetric MxN images and due to time and resource limitations, credible mirror imaging devices were not fabricated. As previously mentioned, the two-layer device was difficult to produce due to the alignment issue since the amount of offset between the top and the bottom 50 μm layers made this device unreliable for characterization.

[6] 3DMMI Characterization

6.1 Introduction

Characterization of the fabricated SU-8 3DMMI waveguides is discussed in this chapter. Optical coupling and propagation loss data are included to demonstrate the power performance of these multimode waveguides. Successful images of 3DMMI are included along with imbalance results. Due to fabrication limitations, a quality 3DMMI-2LR device was difficult to fabricate for characterization.

6.2 Test Setup

All laser sources used for characterization were assembled by TRILabs. Light was coupled into SU-8 waveguides by a Single-Mode Fiber with a uniform core index. Optical imaging was captured using a visible to infrared camera. Optical output power from the multimode SU-8 square waveguide was captured by a Multi-Mode Fiber (MMF) and measured using an optical power meter. The optical signal is coupled into and out of the SU-8 waveguide by coating-stripped fibers. The general test setup is illustrated with Fig. 6-1.

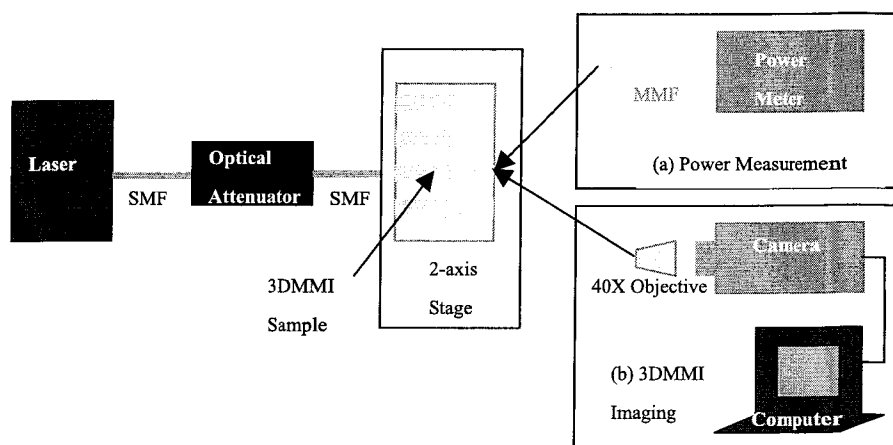


Fig. 6-1: 3DMMI Test Equipment Layout

The output at the end of the waveguide is directed to a power meter via a MMF (50 μm core) or to the image camera via a 40X objective lens separately shown in Fig. 6-1.

6.3 Power Loss Measurements

There are mainly two measurements of power loss, coupling loss from the input fiber to and propagation loss through the SU-8 material. Assume that the losses in the fibers, fiber-to-air, and coupling into the optical power meter are negligible. Define the input power to be the power at the output of the fiber after the optical attenuator. The total loss is approximately the sum of the propagation loss within the waveguide and two coupling losses from the two air-to-SU-8 interfaces. Two waveguide lengths were characterized, one at approximately 8293 μm (980nm 2x2 general imaging), and one at 883 μm (1550 3x3 symmetric-XY imaging). The two operating input wavelengths include the SU-8 low loss wavelength of 980 nm and the SU-8 high loss wavelength of 1550 nm. Since 3DMMI imaging can only be visually detected at low intensities, the input power range for characterization was chosen below -20 dBm.

6.3.1 Insertion Loss

Insertion loss can be defined as the decibel power difference between the output optical power meter power and the input power. The insertion loss behavior for two 3DMMI waveguides at two input wavelengths is illustrated by Fig. 6-2. The precision of this measurement is within ± 0.1 dB. The behavior of insertion loss, as predicted, is independent of the input power. For the wavelength of 1550 nm, insertion loss is ~ 8.4 dB for the longer waveguide and is ~ 4.5 dB for the shorter waveguide. At the 980 nm wavelength, insertion loss is the same for both waveguide lengths at ~ 5.1 dB. Thus, the length of waveguides has a more significant contribution to the total loss for the wavelength of 1550 nm. This phenomenon can be explained by the propagation loss

of SU-8 at different wavelengths as discussed in the next section. Since the insertion loss at 980 nm for both waveguides are similar, this result indicates a relatively high total coupling loss from the two SU-8-to-air interfaces.

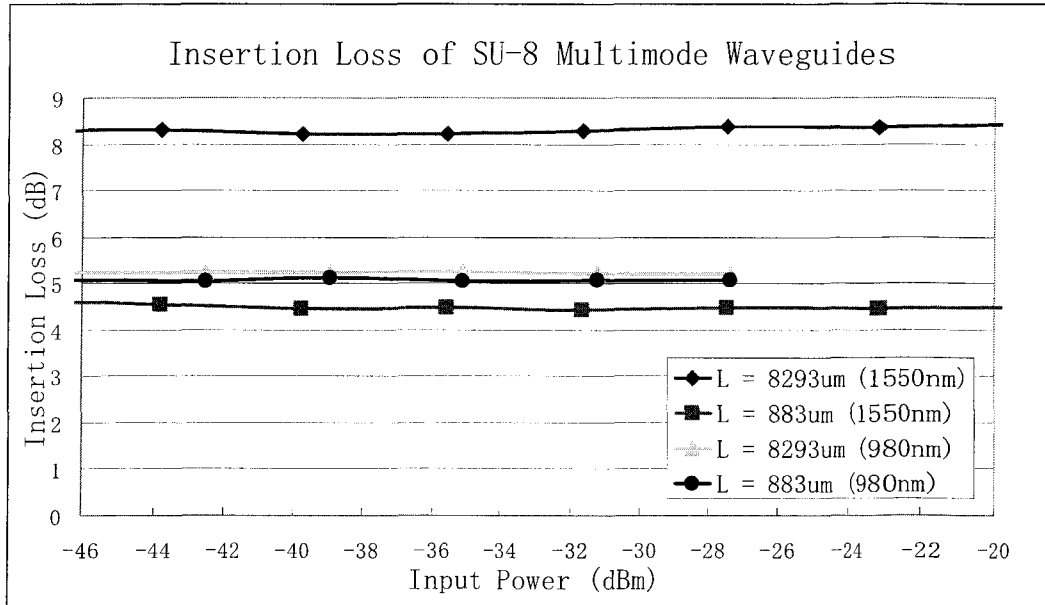


Fig. 6-2: Insertion Loss of SU-8 Multimode Waveguides

6.3.2 Propagation and Coupling Loss

The measured insertion loss is the sum of the propagation loss and the total coupling loss at each wavelength. This insertion loss can be expressed as a function of two waveguide lengths, 883 μm and 8293 μm in Eqs. 6.3.1a and 6.3.1b respectively. At given wavelengths with averaged insertion loss values from Fig. 6-2, the total coupling loss and the propagation loss, α (dB/cm), can be determined with the results shown in Table 6-1.

$$\text{AverageInsertionLoss}(883\mu\text{m}) = \text{TotalCouplingLoss} + 0.0883\text{cm} * \alpha \quad (6.3.1a)$$

$$\text{AverageInsertionLoss}(8293\mu\text{m}) = \text{TotalCouplingLoss} + 0.8293\text{cm} * \alpha \quad (6.3.1b)$$

The propagation loss of SU-8 waveguides is mainly due to the inherent absorption loss of SU-8 by omitting the apparent negligible scattering loss.

	$\lambda_0=980\text{nm}$	$\lambda_0=1550\text{nm}$
Average Insertion Loss (883 μm)	5.1dB	4.5dB
Average Insertion Loss (8293 μm)	5.3dB	8.3dB
Propagation Loss	0.25dB/cm	5.2dB/cm
Total Coupling Loss	5.0dB	4.0dB

Table 6-1: SU-8 Waveguide Propagation and Total Coupling Loss

A low propagation loss at the wavelength of 980 nm is the explanation for similar insertion losses for the two different waveguide lengths. For the wavelength of 1550 nm and at a long waveguide length of 0.83 cm, propagation loss contributes more significantly to the insertion loss. From a previous study shown in Table 5-1, the propagation loss of SU-8 waveguides was reported to be ~ 0.5 dB/cm and ~ 3.0 dB/cm for 980 nm and 1550 nm respectively. The loss at 1550 nm is slightly higher in this study, but different experiments with different conditions will produce slightly different results. These values will vary to a certain degree for all experiments.

The total coupling loss is the sum of the input fiber coupling loss to the waveguide and the output fiber coupling loss. It is important to note that the 50 μm core MMF was only able to capture a certain area of the diffracting power from the end of the waveguides. Even with a larger core diameter (62.5 μm) MMF fiber, the radius of the core is still smaller than the length from the center to a corner of the square waveguide. Thus, we can assume that a large fraction of the total coupling loss will occur at the output end of the waveguide. In conclusion, a large dimension 3DMMI device should not be part of a fiber optics system requiring very low coupling losses. Smaller 3DMMI dimensional designs will greatly reduce the coupling loss due to the end fiber coupling.

6.4 3DMMI Imaging

For short length and loss considerations, symmetrical image distance waveguides were cut and imaged. Symmetric-XY self, 2x2, and 3x3 images were obtained with an

input signal at the 1550 nm wavelength. In addition, general interference 2x2 output images were also measured. The images were obtained using either 4.8 μm or 9 μm MFD (values conforming to good image resolution) SMF fiber inputs. The input was adjusted on the 2-axis stage to position at an assumed central position using quantified controls. The two dimensional alignment of the input can be maximized by viewing the image at the end of the waveguides. These 3DMMI devices cannot be visually imaged by the eye with high optical powers due to high imaging intensities. Thus, optical input power must be brought down to around the range of -47 dBm for visual detection. Optical power is well confined in the SU-8 waveguide through the end-view shown in Fig. 6-3(a). In this figure, the dark background includes the cladding material and the glass substrate. When the ambient light is turned on, the cladding and substrate can be clearly identified in Fig. 6-3(b).

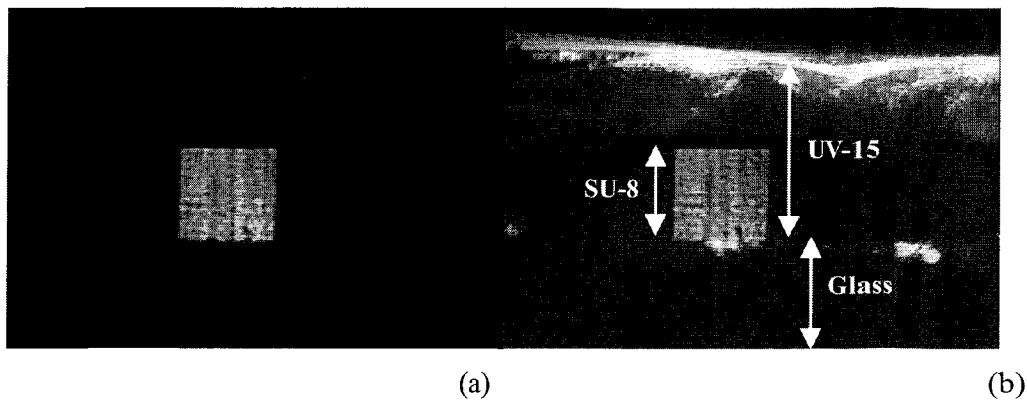


Fig. 6-3: Optical Confinement of SU-8 3DMMI 50x50 μm^2 Structures

Self-Image

The optical attenuator was set at 34.2dB with an approximate output of -53 dBm. With a MFD = 9 μm input, the symmetric-XY self-image from an $L \sim 2650 \mu\text{m}$ device is illustrated in Fig. 6-4. The mode field chosen in this test was for maximizing the field available to the center of the waveguide. The Gaussian shape of the input was not preserved, but the majority of the power remained in the center of the waveguide in contrast to a non-imaged output from Fig. 6-3 (a). As the input field propagates down the waveguide, phase errors between modes will add cumulatively to distort or eliminate its Gaussian shape.

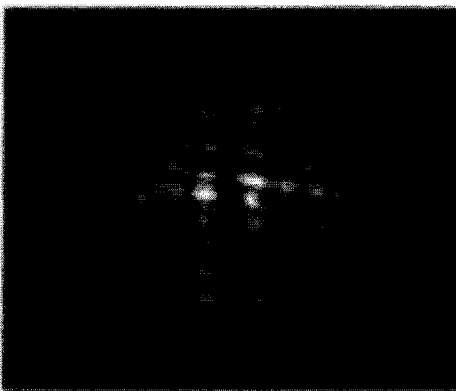


Fig. 6-4: Symmetric-XY Self-Image 50x50 μm^2

In Fig. 6-4, the two high intensity spots should merge to form a better central spot if the device length was more precise to the theoretical value. After dicing, the actual cut position was an offset from the desired cut position, and it was variable within 50-100 μm for each cut. It was thus difficult to obtain small variations for the waveguide length. Despite imperfections in input location, waveguide length, and many other small factors, the optical signal was observed to remain in the center of the waveguide.

2x2-Images

The optical attenuator was set at 29.1dB with an output of about -49 dBm. With a MFD = 4.8 μm input, the symmetric-XY 2x2 images an L ~ 1320 μm device are illustrated in Fig. 6-5.

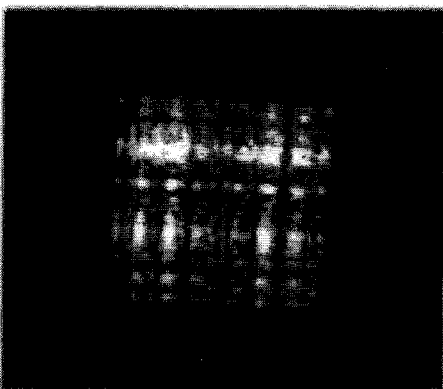


Fig. 6-5: Symmetric-XY 2x2 Images 50x50 μm^2

Again, the Gaussian shape of the input was not preserved, but the total intensity can be concluded to reside in the four sections of this waveguide. The intensity seemed to be higher for the top two images compared to the lower images; this can be explained by a small negative deviation from the 50 μm height of the waveguide. Fields in the upper half will compress in a smaller area causing higher intensities. The pixel values of Fig. 6-5 can be obtained to separate the intensity in all four quadrants. Defining imbalance as the power difference between the highest quadrant power and the lowest quadrant power, this example has a power imbalance of about -2.6 dB.

Similarly, 2x2 images can also be obtained with the general interference shown in Fig. 6-6. The input power was about -54 dBm at the wavelength of 980 nm with a device length of $L \sim 8300 \mu\text{m}$. The imbalance for these general 2x2 images is about 0.9 dB. This imbalance is an improvement from the previous symmetric-XY case, and it is mainly due the fact that the 50 μm height was more accurate. This example also demonstrates general interference imaging despite the fact that the Gaussian shape of the input was not preserved. Imbalance in an ideal system should be zero dB, but device dimensions, improper inputs, and device materials will all contribute to imbalance between the four constructive images.

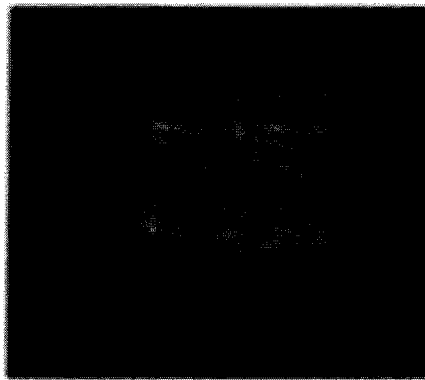


Fig. 6-6: General 2x2 Images

3x3-Images

The optical attenuator was set at 34.2dB with an output of about -52 dBm. With a $\text{MFD} = 4.8 \mu\text{m}$ input, the symmetric-XY 3x3 images for an $L \sim 883 \mu\text{m}$ device are

illustrated in Fig. 6-7(a). In this figure, localized areas of intensity can be detected for 3x3 images. Thus, nine areas of power can be extracted to determine the imbalance of about -1.3 dB. This waveguide has shown a respectable representation of 3x3 images. The simulation of a similar result is illustrated by Fig. 6-7(b). In this figure, the length is $L \sim 991 \mu\text{m}$, which is about $100 \mu\text{m}$ from the fabricated waveguide. Coincidentally, well-defined 5x5 images appear a little distance further from 3x3 images at $1070 \mu\text{m}$. As the length increases from the 3x3 images location, the 9 images separate spatially to arrive at the 5x5 images. This separation is depicted by the result of Fig. 6-7(a) and is predicted by the simulation of Fig. 6-7(b).

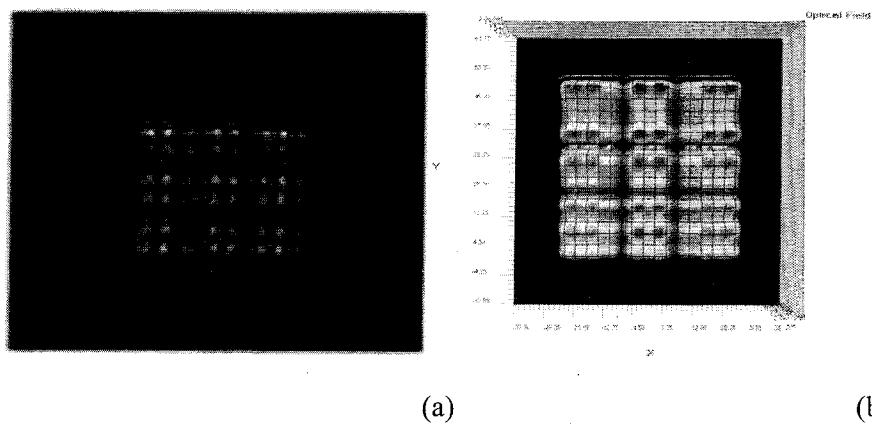


Fig. 6-7: Symmetrical 3x3 Images (a) actual image (b) simulated image

In general, the previous images from Fig. 6-4, Fig. 6-5, and Fig. 6-6 can be concluded to have a similar effect, whether at a slightly shorter or longer length relative to the actual nominal length. Precise length in a fabricated waveguide is difficult to obtain due to the poor accuracy of the dicing machine. In addition, small deviations in refractive indices and widths will also cause a deviation of the image from the proper length. In order to obtain more precise actual 3DMMI images, some equipment needs to be improved.

As for 3DMMI-2LR, alignment and impurity material between two layers are the major issue for a successful design. With technical and time constraints, two-layer routing could not be demonstrated experimentally. Thus, that will be reserved for future studies. The results included in these experiments do give promise to future

3DMMI devices. With more advanced technological facilities, 3DMMI-2LR can definitely be realized.

[7] Summary and Future Endeavors

7.1 Summary of Project

This thesis study began with the vision of routing optical signals from one layer to another as described in Chapter 1. Aside from direct three-dimensional waveguides, MMI behavior seemed to provide an alternative for transferring optical signals in additional waveguide layers. In order to implement MMI theory into more than two dimensions, the theory of 3DMMI was established in Chapter 2. 3DMMI general and restricted images result with a given dimension based on the compliance with phase conditions in both the transverse x and y directions. Various imaging can be designed such as self-image, mirror image, and MxN multiple images. Not only can 3DMMI recreate an input in three dimensions, the input can be routed to different sectors of the cross-sectional field and split into a number of identical images.

Detailed simulations of all possible images were carried out and showed that symmetrical imaging allows for not only short device length, but also better imaging results. Simulation imaging lengths were compared with theoretical values and show very small differences relative to the actual image lengths. 3DMMI was then analyzed to characterize its capabilities in Chapter 3. In order to maximize the POI of desired images, length, input half width, input location, wavelength, and other factors must be taken into consideration. 3DMMI does show negligible dependence on refractive index shifts and polarization; however, physical dimensions have the largest effects and must be tailored with good precision to maximize imaging and power.

For the realization of various applications in Chapter 4, 3DMMI must be designed to route signals to additional layers via 3DMMI-2LR, shown for the first time. Optical signals can now be routed between layers simply by introducing 3DMMI mirroring sections. The proposed 3DMMI-2LR can be designed with large or small dimensions and both showed low loss of less than 1 dB and good imaging.

In Chapter 5, 3DMMI was then considered in real devices using a polymer

known as SU-8 since this polymer is a compatible and easy to process material. These fabricated structures were then characterized and reported in Chapter 6 where loss results were analyzed. SU-8 waveguides showed low losses, especially at 980 nm (0.25 dB/cm) and they demonstrated detectable real self and multiple images at a wavelength of 1550 nm. Due to fabrication and technology limitations, 3DMMI imaging was still far from ideal. The greatest contribution for non-ideal imaging was dicing inaccuracies.

7.2 Future Endeavors

In a theoretical perspective, 3DMMI shows promising possibilities for the future. As integrated optics progresses further to assist or replace current electronic devices, stacked layers of optical information may be essential for communication. The behavior of 3DMMI is reliable and may well be established in practical devices. Future simulation can be completed for various applications such as WDM, various channel structures for microfluidics, optical bridges, optical mirroring, tapered three-dimensional structures, and three or more layers of routing. In general, any application that requires routing will benefit from 3DMMI followed with subsequent simulation.

Effective fabrication of 3DMMI will need to be studied in detail in the future. For one thing, the material for 3DMMI may be a non-polymer or another type of polymer to deal with dimensional issues. So far, SU-8 is still a good material for easy fabrication. This is, of course, important for manual device fabrication. Fabrication of 3DMMI has only been demonstrated twice to date, which includes this project and a project using silicon [42]. Study of other materials may be important for more efficient 3DMMI devices. The cladding material is also important for these devices since it must be compatible with the core material. For 3DMMI, it is still difficult to fabricate input waveguides to connect to a large transverse cross-section. Potentially, they can be fabricated layer-by-layer along with the cladding material. The substrate

material may also be another material such as silicon. In terms of device length, other cutting methods or equipment may be explored for glass or silicon to improve the precision. A 3DMMI device with more precise dimensions will definitely be advantageous for the implementation of actual devices.

For 3DMMI-2LR devices, planarization of the first layer is crucial. The UV-15 material has shown good planarization results and this can be assumed for other materials. For small dimension 3DMMI-2LR, a planarization material needs to be researched. Planarization can be achieved using spin-on or deposit methods with more complex technologies. Another issue is the alignment of the two layers and this can be more accurate with automation or using electron microscopes. Because of this alignment issue, another production method may be to fabricate the three sections of the 3DMMI-2LR separately with stress on establishing the connection on the same substrate. The same issues apply in large dimensions, but these structures are easier to manage because of their sizes. Two-layer bonding may be applied where the top layer on a clear substrate is bonded onto the bottom layer with proper alignment. When 3DMMI devices are well established, its integration with photonic crystal structures will allow for 90° bending of light and a system to guide and route signals in all three dimensions. Such systems will allow for inter-device communication and will lead the way for all-optical 3D devices.

List of References

- [1] A. Louri, "Optical interconnection networks for scalable high-performance parallel computing systems," *Optical Interconnect Workshop for High Performance Computing*, Oak Ridge, Tennessee, Nov. 8-9, 1999.
- [2] Intel Corporation Website: <http://www.intel.com>.
- [3] D. A. B. Miller and H. M. Ozaktas, "Limit to the bit-rate capacity of electrical interconnects from the aspect ratio of the system architecture," *J. Parallel and Distributed Computing*, vol. 41, no. 1, pp. 42-52, 1997.
- [4] B. E. A. Saleh, M. C. Teich, *Fundamentals of Photonics*, John Wiley & Sons, Inc., 1991.
- [5] S. E. Miller, "Integrated optics: an introduction," *The Bell System Technical Journal*, vol. 48, no. 7, Sept. 1969.
- [6] J. McCrone, "The future is bright," *New Scientist*, pp. 40-44, Oct. 25, 1997.
- [7] D. A. B. Miller, "Optical interconnects to silicon," *IEEE J. Select. Topics Quan. Elect.*, vol. 6, no. 6, 2000.
- [8] H. F. Talbot, "Facts relating to optical science no. iv," *Edinburgh Philosophical Magazine J. Sci.*, vol. 9, pp. 401-407, Dec. 1836.
- [9] L. B. Soldano, F. B. Veerman, M. K. Smit, B. H. Verbeek, A. H. Dubost, and E. C. M. Pennings, "Planar monomode optical couplers based on multimode interference effects," *J. Lightwave Technol.*, vol. 10, no. 12, pp. 1843-1850, Dec. 1992.
- [10] A. Ferreras, F. Rodríguez, E. Gómez-Salas, J. L. de Miguel, and F. Hernández-Gil, "Useful formulas for multimode interference power splitter/combiner design," *IEEE Photon. Technol. Lett.*, vol. 5, no. 10, pp. 1224-1227, Oct. 1993.
- [11] E. C. M. Pennings, R. van Roijen, M. J. N. van Stralen, P. J. de Waard, R. G. M. P. Koumans, and B. H. Verbeek, "Reflection properties of multimode

- interference devices,” *IEEE Photon. Technol. Lett.*, vol. 6, no. 6, pp. 715-718, Jun. 1994.
- [12] L. B. Soldano, E. C. M. Pennings, “Optical multi-mode interference devices based on self-imaging: principles and applications,” *J. Lightwave Technol.*, vol. 13, no. 4, pp. 615-627, Apr. 1995.
- [13] N. S. Lagali, *The Generalized Mach-Zehnder Interferometer using Multimode Interference Couplers for Optical Communication Networks*, Ph. D. Thesis, 2000.
- [14] J. M. Heaton and R. M. Jenkins, “General matrix theory of self-imaging in multimode interference (MMI) couplers,” *IEEE Photon. Technol. Lett.*, vol. 11, no. 2, pp. 212-214, Feb. 1999.
- [15] D. S. Levy, R. Scarmozzino, Y. M. Li, and R. M. Osgood, Jr., “A new design for ultracompact multimode interference-based 2 x 2 couplers,” *IEEE Photon. Technol. Lett.*, vol. 10, no. 1, pp. 96-98, Jan. 1998.
- [16] D. S. Levy, K. H. Park, R. Scarmozzino, R. M. Osgood, Jr., C. Dries, P. Studenkov, and S. Forrest, “Fabrication of ultracompact 3-dB 2 x 2 MMI power splitters,” *IEEE Photon. Technol. Lett.*, vol. 11, no. 8, pp. 1009-1011, Aug. 1999.
- [17] H. Z. Wei, J. Z. Yu, Z. L. Liu, X. F. Zhang, W. Shi, and C. S. Fang, “Fabrication of 2x2 tapered multimode interference coupler,” *Elec. Lett.*, vol. 36, no. 19, pp. 1618-1619, Sept. 2000.
- [18] H. Z. Wei, J. Z. Yu, Z. L. Liu, X. F. Zhang, W. Shi, and C. S. Fang, “Fabrication of 4x4 tapered MMI coupler with large cross section,” *IEEE Photon. Technol. Lett.*, vol. 13, no. 5, pp. 466-468, May 2001.
- [19] Z. Wu and K. Utaka, “Study on tapered multimode interference-based coherent lightwave combiners,” *IEICE Trans. Electron.*, vol. E88-C, no. 5, May 2005.
- [20] J. Leuthold and C. H. Joyner, “Multimode interference couplers with tunable power splitting ratios,” *J. Lightwave Technol.*, vol. 19, no. 5, pp. 700-707, May 2001.

- [21] S. Nagai, G. Morishima, H. Inayoshi, and K. Utaka, "Multimode Interference Photonic Switches (MIPS)," *J. Lightwave Technol.*, vol. 20, no. 4, pp. 675-681, Apr. 2002.
- [22] K. Utaka, "Semiconductor photonic switching devices for wavelength division multiplexing systems," *IPAP Books 2*, pp. 161-174, 2005.
- [23] S. El-Sabban, D. Khalil, I. Schanen, and P. Benech, "Design of an integrated optical magic T for astronomy applications," *Appl. Opt.*, vol. 39, no. 36, pp. 6781-6786, Dec. 2000.
- [24] A. Irace and G. Breglio, "All-silicon optical temperature sensor based on multi-mode interference," *Opt. Exp.*, vol. 11, no. 22, pp. 2807-2812, Nov. 2003.
- [25] Y. H. Lee and H. Y. Ryu, "Custom Crystals Control Photons," *IEEE Circ. & Dev. Mag.*, pp. 8-15, May 2002.
- [26] A. Sure, T. Dillon, J. Murakowski, C. C. Lin, D. Pustai, and D. W. Prather, "Fabrication and characterization of three-dimensional silicon tapers," *Opt. Exp.*, vol. 11, no. 26, pp. 3555-3561, Dec. 2003.
- [27] S. M. Garner, S. S. Lee, V. Chuyanov, A. T. Chen, A. Yacoubian, W. H. Steier, and L. R. Dalton, "Three-dimensional integrated optics using polymers," *IEEE J. Quan. Elect.*, vol. 35, no. 8, pp. 1146-1155, Aug. 1999.
- [28] A. Jiang, S. Y. Shi, G. Jin, and D. W. Prather, "Performance analysis of three dimensional high index contrast dielectric waveguides," *Opt. Exp.*, vol. 12, no. 4, pp. 633-643, Feb. 2004.
- [29] S. L. He, X. Y. Ao, and V. Romanov, "General properties of NxM self-images in a strongly confined rectangular waveguide," *Appl. Opt.*, vol. 42, no. 24, pp. 4855-4859, Aug. 2003.
- [30] D. Khalil and A. Yehia, "Two-dimensional multimode interference in integrated optical structures," *J. Opt. A: Pure Appl. Opt.*, vol. 6, pp. 137-145, 2004.
- [31] E. Voges and R. Ulrich, "Self-imaging by phase coincidences in rectangular dielectric waveguides," *6th European Microwave Conference Proc.*, Rome,

- Italy, Sept. 1976.
- [32] L. Eldada, and L. W. Shacklette, "Advances in polymer integrated optics," *IEEE J. Sel. Top. Quan. Elect. Lett.*, vol. 6, no. 1, pp. 54-68, Jan./Feb. 2000.
- [33] R. G. Hunsperger, *Integrated Optics: Theory and Technology*, Springer-Verlag Berlin Heidelberg, 1991.
- [34] D. K. Cheng, *Field and Wave Electromagnetics*, Addison-Wesley Publishing Company, Inc., Nov. 1992.
- [35] M. F. Iskander, *Electromagnetic Fields and Waves*, Prentice-Hall, Inc., Englewood Cliffs, New Jersey, 1992.
- [36] E. A. J. Marcatili, "Dielectric waveguide and directional coupler for integrated optics," *Bell Syst. Technol. J.*, vol. 48, no. 7, pp. 2071-2102, Sept. 1969.
- [37] J. E. Goell, "A circular-harmonic computer analysis of rectangular dielectric waveguides," *Bell Syst. Technol. J.*, vol. 48, no. 7, pp. 2133-2160, Sept. 1969.
- [38] M. K. Barnoski, *Introduction to Integrated Optics*, Plenum Press, New York, 1974.
- [39] T. Tamir, *Guided-Wave Optoelectronics*, Springer-Verlag Berlin, 1990.
- [40] N. S. Kapany and J. J. Burke, *Optical Waveguides*, Academic Press, Inc., New York, New York, 1972.
- [41] M. Bachmann, P. A. Besse, and H. Melchior, "General self-imaging properties in NxN multi-mode interference couplers including phase relations," *Appl. Opt.*, vol. 33, no. 17, pp. 3905-3911, 1994.
- [42] M. Bachmann, P. A. Besse, and H. Melchior, "Overlapping-image multimode interference couplers with a reduced number of self-images for uniform and nonuniform power splitting," *Appl. Opt.*, vol. 34, no. 30, pp. 6898-6910, 1995.
- [43] Optiwave BPM 6.0 Software Help Topics, Optiwave Corporation: <http://www.optiwave.com>.
- [44] R. Ulrich and T. Kamiya, "Resolution of self-images in planar optical waveguides," *J. O.S.A.*, vol. 68, no. 5, pp. 583-592, 1978.

- [45] P. A. Besse, M. Bachmann, H. Melchior, L. B. Soldano, and M. K. Smit, "Optical Bandwidth and Fabrication Tolerances of Multimode Interference Couplers," *J. Lightwave Technol.*, vol. 12, no. 6, Jun. 1994.
- [46] Y. L. Sun, X. Q. Jiang, J. Y. Yang, Y. Tang, and M. H. Wang, "Experimental demonstration of two-dimensional multimode-interference optical power splitter," *Chin. Phys. Lett.*, vol. 20, no. 12, pp. 2182-2184, 2003.
- [47] A. Yehia and D. Khalil, "Design of a compact three-dimensional multimode interference phased array structures (3-D MMI PHASAR) for DWDM applications," *IEEE J. Sel. Top. Quan. Elect.*, vol. 11, no. 2, Mar/Apr 2005.
- [48] X. Chen, J. N. McMullin, C. J. Haugen, and R. G. DeCorby, "Integrated diffraction grating for lab-on-a-chip microspectrometers," *SPIE Proc.*, vol. 5699, pp. 511-516, Mar. 2005.
- [49] H. Ma, A. K.-Y. Jen, L. R. Dalton, "Polymer-based optical waveguides: materials, processing, and devices," *Adv. Mater.*, vol. 14, no. 19, Oct. 2, 2002.
- [50] L. J. Guerin, "The SU8 homepage," Website: <http://www.geocities.com/guerinlj>.
- [51] "The SU-8 photo-resist for MEMS," Website: <http://aveclafaux.freeseverscom/SU-8.html>.
- [52] M. Shaw, D. Nawrocki, R. Hurditch, and D. Johnson, "Improving the process capability of SU-8," MicroChem Corp., Website: http://www.microchem.com/resources/su8_process_capability_paper_1.pdf.
- [53] D. W. Johnson, A. Jeffries, D. W. Minsek, and R. J. Hurditch, "Improving the process capability of SU-8, part II," MicroChem Corp., Website: http://www.microchem.com/resources/su8_process_capability_paper_2.pdf.
- [54] A. Borreman, S. Musa, A. A. M. Kok, M. B. J. Diemeer, and A. Driessen, "Fabrication of polymeric multimode waveguides and devices in SU-8 photoresist using selective polymerization," *Proc. Symp. IEEE/LEOS Benelux Chapter*, Amsterdam, pp. 83-86, 2002.
- [55] California State University Chemistry Department, Website:

<http://wwwchem.csustan.edu/>.

- [56] H. Yu, A. Grüntzig, Y. Zhao, A. Sharon, B. Li, and X. Zhang, "Direct writing of 3D microstructures using a scanning laser system," *Mat. Res. Soc. Symp. Proc.*, vol. 782, A11.5.1-A11.5.6, 2004.
- [57] L. Pang, W. Nakagawa, and Y. Fainman, "Fabrication of optical structures using SU-8 photoresist and chemically assisted ion beam etching," *Opt. Eng.*, vol. 42, no. 10, pp. 2912-2917, Oct. 2003.
- [58] G. Hong, A. S. Holmes, M. E. Heaton, "SU8 resist plasma etching and its optimization," *DTIP 2003 Proc.*, pp. 268-271, Mandelieu – La Napoule, France, May 5-6 2003.
- [59] B.-Y. Shew, T.-Y. Huang, K.-P. Liu, and C.-P. Chou, "Oxygen quenching effect in ultra-deep x-ray lithography with SU-8 resist," *J. Micromech. Microeng.*, vol. 14, pp. 410-414, 2004.
- [60] K. K. Tung, W. H. Wong, and E. Y. B. Pun, "Polymeric optical waveguides using direct ultraviolet photolithography process," *Appl. Phys. A*, 2003.
- [61] P. Rabiei, W. H. Steier, C. Zhang, and L. R. Dalton, "Polymer micro-ring filters and modulators," *J. Lightwave Technol.*, vol. 20, no. 11, pp. 1968-1975, Nov. 2002.
- [62] D. Nilsson, S. Balslev, and A. Kristensen, "Polymer microcavity dye laser based on a single mode SU-8 planar waveguide," *SPIE Proc.*, vol. 5707, pp. 208-216, Apr. 2005.
- [63] E. H. Conradie and D. F. Moore, "SU-8 thick photoresist processing as a functional material for MEMS applications," *J. Micromech. Microeng.*, vol. 12, pp. 368-374, 2002.
- [64] M. C. Peterman, P. Huie, D. M. Bloom, and H. A. Fishman, "Building thick photoresist structures from the bottom up," *J. Micromech. Microeng.*, vol. 13, pp. 380-382, 2003.
- [65] J. Carlier, S. Le Gac, S. Arscott, V. Thomy, J. C. Fourier, F. Caron, C. Cren-Olivé, C. Rolando, J. C. Camart, C. Druon, and P. Tabourier, "SU-8 technology and monolithic columns for integration in a biological

- lab-on-chip,” *Proc. 7th Int. Conf. Miniaturized Chem. Biochem. Analy. Sys.*, Squaw Valley, USA, Oct. 5-9, 2003.
- [66] M. Fleger, D. Siepe, and A. Neyer, “Microfabricated polymer analysis chip for optical detection,” *IEE Proc. Nanobiotechnol.*, vol. 151, no. 4, pp. 159-161, Aug. 2004.
- [67] J. Carlier, S. Arscott, V. Thomy, J. C. Fourier, F. Caron, J. C. Camart, C. Druon, and P. Tabourier, “Integrated microfluidics based on multi-layered SU-8 for mass spectrometry analysis,” *J. Micromech. Microeng.*, vol. 14, pp. 619-624, 2004.
- [68] T. Ouchi, A. Imada, T. Sato, and H. Sakata, “Direct coupling of VCSELs to plastic optical fibers using guide holes patterned in a thick photoresist,” *IEEE Photon. Technol. Lett.*, vol. 14, no. 3, pp. 263-265, Mar. 2002.
- [69] J. S. Kim, J. W. Kang, and J. J. Kim, “Simple and low cost fabrication of thermally stable polymeric multimode waveguides using a UV-curable epoxy,” *Jpn. J. Appl. Phys.*, vol. 42, pp. 1277-1279, 2003.
- [70] J.-N. Kuo, G.-B. Lee, and W.-F. Pan, “Projection display technique utilizing three-color-mixing waveguides and microscanning devices,” *IEEE Photon. Technol. Lett.*, vol. 17, no. 1, Jan. 2005.
- [71] Y. Liu, J. Bishop, L. Williams, S. Blair, and J. Herron, “Biosensing based upon molecular confinement in metallic nanocavity arrays,” *Nanotechnol.*, vol. 15, pp. 1368-1374, 2004.
- [72] Ancillaries: Omnicoat Adhesion Promoter/Release Layer, MicroChem Corp., Website: <http://www.microchem.com/products/pdf/OMNICOAT.pdf>.
- [73] J. Zhang, M. B. Chan-Park, and S. R. Conner, “Effect of exposure dose on the replication fidelity and profile of very high aspect ratio microchannels in SU-8,” *Lab Chip*, vol. 4, pp. 646-653, 2004.
- [74] Y. J. Chuang, F. G. Tseng, and W. K. Lin, “Reduction of diffraction effect of UV exposure on SU-8 negative thick photoresist by air gap elimination,” *Microsys. Technol.*, vol. 8, pp. 308-308, 2002.
- [75] C. Choi, L. Lin, Y. J. Liu, J. Choi, L. Wang, D. Haas, J. Magera, and R. T.

Chen, "Flexible optical waveguide film fabrications and optoelectronic devices integration for fully embedded board-level optical interconnects," *J. Lightwave Technol.*, vol. 22, no. 9, pp. 2168-2176, Sept. 2004.

- [76] NANO™ SU-8 2050, MicroChem Corp., Website:
http://www.microchem.com/products/pdf/SU8_2035-2100.pdf.
- [77] Master Bond UV Adhesive, Master Bond Inc., Website:
<http://www.masterbond.com/sg/uvsg.html>.
- [78] Kopp 7380 UV Absorbing Glass Product Data Sheet, Kopp Glass, Inc.,
Website: <http://www.koppglass.com/filterSummary.php>.
- [79] Ancillaries: SU-8 Developer, MicroChem Corp., Website:
<http://www.microchem.com/products/ancillaries.htm>.
- [80] MEMS-Exchange Forum Website: <http://www.mems-exchange.org>.
- [81] S. Musa, N. Lagali, Sulur, G. Sengo, and A. Driessen, "Fabrication of polymeric multimode waveguides for application in the local area network and optical interconnects," Proc. Symp. IEEE/LEOS, Benelux Chapter, Delft, The Netherlands, pp. 95-98, 2000.
- [82] Norland Optical Adhesive 65, Norland Products Inc., Website:
<https://www.norlandprod.com/adhesives/noa%2065.html>.

Appendix A: Matlab Calculation

Codes/Analysis Plots

The follow Matlab codes include numerical solutions to the designed imaging lengths according to specified parameters, analysis results, and respective graphs.

Section I: The following code calculates the image lengths for symmetric 1x1, 2x2, 3x3 images, asymmetric self-images, cross-images, mirror images with x, and mirror images with y.

```
% 3DMMI Theoretical Numerical Imaging Solutions
% Author: Nan Xie
% Parameters:
%          k0 = intrinsic propagation constant in vacuum
%          ky = propagation constant in y transverse direction
%          kx = propagation constant in x transverse direction
%          ng = index of the guide core
%          nc = index of the cladding
%          l = mode integer in x direction
%          m = mode integer in y direction
%          lamda = wavelength input
%          Wx = width of core in x direction
%          Wy = height of core in y direction
%          Wxeff = effective guide width in x direction
%          Wyeff = effective guide height in y direction
%          Lx = beat length of fundamental beta00 and beta10 modes
%          Ly = beat length of fundamental beta00 and beta01 modes
%          z = z direction of propagation
%          P = Phase factor as MMI occurs
% Equations:
%          k0 = 2*pi/lamda
%          ng^2*k0^2 = kx^2 + ky^2 + b^2
%          b = ng*k0*sqrt(1 + (-kx^2/(ng^2*k0^2)-ky^2/(ng^2*k0^2)))
%          kx = pi*(l+1)/Wxeff
%          ky = pi*(m+1)/Wyeff
%          Wxeff = Wx + lamda/(pi*sqrt(ng^2-nc^2))
%          Wyeff = Wy + lamda/(pi*sqrt(ng^2-nc^2))
```

```

%          ba = k0*ng*(1-0.5*((kx/(k0*ng))^2 + (ky/(k0*ng))^2))
%          Lx = 4*ng*Wxeff^2/(3*lamda)
%          Ly = 4*ng*Wyeff^2/(3*lamda)
% *****All Units in Microns (um)*****
clear all
% Calculations:
Z1(3,3)= [0:0]; % Symmetric 1x1, 2x2, 3x3 outputs
Z2(3,3)= [0:0]; % Non-symm self image, cross image
Z3(4,3)= [0:0]; % Mirror with X, mirror with Y
W(4,3)= [0:0]; % Widths of part 3, for X mirroring and Y mirroring
% PART 1 (50x50 Symmetrical NxN Image):
lamda = [0.67,0.98,1.55];
Wx = 50;
Wy = 50;
ng = [1.5953, 1.5846, 1.5765]; % average
nc = [1.513, 1.508, 1.502]; % (from manufacturer extrapolation)
IX(3,3)= [0:0];
IY(3,3)= [0:0];
K = 0;
for n = 1:3
    Wxeff(n) = Wx + lamda(n)/(pi*sqrt(ng(n)^2-nc(n)^2));
    Wyeff(n) = Wy + lamda(n)/(pi*sqrt(ng(n)^2-nc(n)^2));
    Lx(n) = 4*ng(n)*Wxeff(n)^2/(3*lamda(n));
    Ly(n) = 4*ng(n)*Wyeff(n)^2/(3*lamda(n));
    for Nx=1:3 % 1x1, 2x2, 3x3 possibilities
        IX(Nx+K)= 3*Lx(n)/(4*Nx);
    end
    for Ny=1:3
        IY(Ny+K)= 3*Lx(n)/(4*Ny);
    end
    K=K+3;
end
Z1 = IX;
% PART 2 (50x50 Non-symmetrical 2x2 Image & Self Image & Cross Axis Image):
for K = 0:3:6
    for n = 1:3
        if K==0 % Self Image (1)
            Z2(n+K)= 6*Lx(n);
        elseif K==3 % Cross Axis Image (2)
            Z2(n+K)= 3*Lx(n);
        elseif K==6 % 2x2 Image (3)
            Z2(n+K)= 3*Lx(n)/2;
        end
    end
end

```



```

end
Z2 = Z2';
% PART 3 (50xUnknown Quadrant Input Mirror with X, Mirror with Y):
% Mirror about X-Axis
% Py= 1, 3, Px =1 (Py always odd)
% Wxeff/Wyeff = sqrt(0.5) or sqrt(1.5)
% Mirror about Y-Axis
% Py= 1, Px =1, 3 (Px always odd)
% Wxeff/Wyeff = sqrt(2) or sqrt(2/3)
% Wy = 50; %Constant
IX(3,3)=[0:0];
IY(3,3)=[0:0];
G = 0;
for K=[0.5,1.5,2.0,2/3]
    for n = 1:3
        Wxeff(n) = sqrt(K)*Wyeff(n);
        Wx(G+1,n) = Wxeff(n) - lamda(n)/(pi*sqrt(ng(n)^2-nc(n)^2));
        Lx(n) = 4*ng(n)*Wxeff(n)^2/(3*lamda(n));
        if K==2.0
            Z3(G+1,n)= 3*Lx(n);
        elseif K==2/3
            Z3(G+1,n)= 9*Lx(n);
        else
            Z3(G+1,n)= 6*Lx(n);
        end
    end
end
G=G+1;
end
W = Wx;

```

Section II: The following code produces the analysis of 3DMMI devices based on the effects of wavelength on image length, effects of both x and y dimensions, effects of n_c , effects of n_g , effects of polarization, image resolution, optical bandwidth, fabrication tolerances such as length, n_g , and width.

```

% 3DMMI Analysis
% Author: Nan Xie
clear all
s = false;
% Effects of Lamda
lamda1 = [0.60:0.01:1.59];
ng = 1.585;

```

```

nc = 1.52;
Wx = 30;
Wy = 30;
Wxeff = Wx + lamda1/(pi*sqrt(ng^2-nc^2));
Wyeff = Wy + lamda1/(pi*sqrt(ng^2-nc^2));
% Beating Lengths
Lx = 4*ng*Wxeff.^2./(3*lamda1);
Ly = 4*ng*Wyeff.^2./(3*lamda1);
for Nx=1:5
    Ny = Nx;
    IX1 = 3*Lx/(4*Nx);
    IY1 = 3*Ly/(4*Ny);
    if s == true
        % Plotting:
        figure(1)
        title('3DMMI Symmetrical Input N Image Lamda')
        xlabel('Input Wavelength (um)')
        ylabel('Distance of Travel (um)')
        plot(lamda1,IX1,'b')
        hold on
    end
end
% Effects of Both Widths (keeping the same)
lamda1=1.55;
ng = 1.585;
nc = 1.52;
% 100 array
Wy = [3:1:102];
Wx = [3:1:102];
Wxeff1 = Wx + lamda1/(pi*sqrt(ng^2-nc^2));
Wyeff1 = Wy + lamda1/(pi*sqrt(ng^2-nc^2));
% Beating Lengths
Lx = 4*ng*Wxeff1.^2./(3*lamda1);
Ly = 4*ng*Wyeff1.^2./(3*lamda1);
for Nx=1:5
    Ny = Nx;
    IX1 = 3*Lx/(4*Nx);
    IY1 = 3*Ly/(4*Ny);
    if s == true
        % Plotting:
        figure(2)
        title('3DMMI Symmetrical Input MxN Image Width')
        xlabel('MMI Width (um)')
        ylabel('Image Distance (um)')
    end
end

```

```

        plot(Wx,IX1,'b')
        hold on
    end
end
% Effects of nc
    lamda = 1.55;
    ng = 1.585;
    nc = [1.00:0.001:1.584];
    Wx = 30;
    Wy = 30;
    Wxeff = Wx + lamda./(pi.*sqrt(ng^2-nc.^2));
    Wyeff = Wy + lamda./(pi.*sqrt(ng^2-nc.^2));
    % Beating Lengths
    Lx = 4*ng*Wxeff.^2/(3*lamda);
    Ly = 4*ng*Wyeff.^2/(3*lamda);
for Nx=1:5
    Ny = Nx;
    IX1 = 3*Lx/(4*Nx);
    IY1 = 3*Ly/(4*Ny);
    if s == true
        % Plotting:
        figure(3)
        title('3DMMI Symmetrical Input MxN Image nc')
        xlabel('Cladding Index')
        ylabel('Image Distance (um)')
        plot(nc,IX1,'b')
        hold on
    end
end
% Effects of ng
    lamda = 1.55;
    ng = [1.56:0.001:1.595];
    nc = 1.52;
    Wx = 30;
    Wy = 30;
    Wxeff = Wx + lamda./(pi.*sqrt(ng.^2-nc.^2));
    Wyeff = Wy + lamda./(pi.*sqrt(ng.^2-nc.^2));
    % Beating Lengths
    Lx = 4.*ng.*Wxeff.^2/(3*lamda);
    Ly = 4.*ng.*Wyeff.^2/(3*lamda);
for Nx=1:5
    Ny = Nx;
    IX1 = 3*Lx/(4*Nx);
    IY1 = 3*Ly/(4*Ny);

```

```

if s == true
    % Plotting:
    figure(4)
    title('3DMMI Symmetrical Input MxN Image ng')
    xlabel('Guide Index')
    ylabel('Image Distance (um)')
    plot(ng,IX1,'b')
    hold on
end
end
% Effects of Polarization
lamda = 1.55;
%Polization Effects: nc/ng change of Weff affecting Transverse Magnetic Fields Hx or Hy
ng = 1.585;
nc = [1.00:0.001:1.584];
nm = nc/ng;
Wx = 30;
Wy = 30;
% Suppose TE, so transverse H field in y directions, thus Wyeff is
% affected
Wxeff = Wx + lamda./(pi.*sqrt(ng^2-nc.^2));
Wyeff = Wy + nm.^2.*lamda./(pi.*sqrt(ng^2-nc.^2));
% Beating Lengths
Lx = 4*ng*Wxeff.^2/(3*lamda);
Ly = 4*ng*Wyeff.^2/(3*lamda);
for Nx=1:5
    Ny = Nx;
    IX1 = 3*Lx/(4*Nx);
    IY1 = 3*Ly/(4*Ny);
    if s == true
        % Plotting:
        figure(5)
        title('3DMMI Symmetrical Input MxN Image Polarization Effects')
        xlabel('nc/ng')
        ylabel('Image Distance (um)')
        plot(nm,IY1,'b')
        plot(nm,IX1,'r')
        hold on
    end
end
end
if s == true
    figure(6)
    title('3DMMI Symmetrical Polarization Effect of Wyeff')
    xlabel('nc/ng')

```

```

        ylabel('Wyeff (um)')
        plot(nn,Wyeff,'b')
        hold
        plot(nn,Wxeff,'r')
        hold off
    end
% Determine Image Resolution
    lamda = 1.55;
    ng = 1.585;
    nc = 1.52;
    WxHW = [3:1:100];
    WxeffHW = WxHW + lamda/(pi*sqrt(ng^2-nc^2));
    Mxy = pi/4*(2*WxHW/lamda).^2*(ng^2-nc^2);
    M = sqrt(Mxy);
    MM = int16(M);
    MMM = double(MM);
    HW = 1.5*(WxeffHW./MMM)/(sqrt(2*log(2)));
    Mxy = Mxy';
%%%%%%%%%%%%%%%%%%%%%%%%%%%%%%%%%%%%%%%%%%%%%%%%%%%%%%%%%%%%%%%%%%%%%%%%
% Bandwidth and Tolerance
% 2D PLOTS VERSION (3D plots also possible)
%%%%%%%%%%%%%%%%%%%%%%%%%%%%%%%%%%%%%%%%%%%%%%%%%%%%%%%%%%%%%%%%%%%%%%%%
    %Factor a = General (3) /Symm (3/4) /Paired (1)
    for a = [3, 1, 3/4];
        %Limit to axis
        b = 150;
        %Number of Images
        for N = [1,5];
            %N = 1;
            % Beam Waist
            w0 = 6.66; % due to HW = 3.33um
            lamda = 1.55;
            nc = 1.52;
            ng = 1.585;
            Wx = 30;
            Wy = 30;
            Wxeff = Wx + lamda/(pi*sqrt(ng^2-nc^2));
            Wyeff = Wy + lamda/(pi*sqrt(ng^2-nc^2));
            % Beating Lengths
            Lx = 4*ng*Wxeff.^2./(3*lamda);
            Ly = 4*ng*Wyeff.^2./(3*lamda);
            for Nx=1:5
                Ny = Nx;
                IX1(Nx)= a*Lx/(Nx);
            end
        end
    end

```

```

    IY1(Nx)= a*Ly/(Ny);
end
dLx = [-b:1:b];
dLy = zeros(1,2*b+1);
zx = (2*lamda*dLx)/(pi*ng*w0^2);
zy = (2*lamda*dLy)/(pi*ng*w0^2);
for i = -b:1:b
    for g = -b:1:b
        T(i+(b+1),g+(b+1)) = 1/(sqrt(1+zx(i+(b+1)))^2)*sqrt(1+zy(g+(b+1)))^2);
    end
end
end
% 2D PLOTS
for i = -b:1:b
    Loss(i+(b+1)) = 10*log10(T(i+(b+1), 1));
end
figure(7)
if N == 1
    if a == 3
        plot(dLx, Loss, 'b', 'Linewidth', 2)
    elseif a == 1
        plot(dLx, Loss, 'r', 'Linewidth', 2)
    else
        plot(dLx, Loss, 'm', 'Linewidth', 2)
    end
end
else
    if a == 3
        plot(dLx, Loss, 'g', 'Linewidth', 2)
    elseif a == 1
        plot(dLx, Loss, 'c', 'Linewidth', 2)
    else
        plot(dLx, Loss, 'k', 'Linewidth', 2)
    end
end
end
title('Fabrication Tolerance Length', 'FontSize', 18)
xlabel('dLx (um)', 'FontSize', 14)
ylabel('Excess Loss (dB)', 'FontSize', 14)
hold on
dWxeff = dLx/IX1(N)*Wxeff*0.5;
dWx = dWxeff+Wx;
figure(8)
if N == 1
    if a == 3
        plot(dWx, Loss, 'b', 'Linewidth', 2)
    elseif a == 1

```

```

        plot(dWx,Loss,'r','Linewidth',2)
    else
        plot(dWx,Loss,'m','Linewidth',2)
    end
else
    if a ==3
        plot(dWx,Loss,'g','Linewidth',2)
    elseif a==1
        plot(dWx,Loss,'c','Linewidth',2)
    else
        plot(dWx,Loss,'k','Linewidth',2)
    end
end
end
title('Fabrication Tolerance Width','FontSize',18 )
xlabel('Wx (um)', 'FontSize',14 )
ylabel('Excess Loss (dB)','FontSize',14 )
hold on
dngx = dLx/IX1(N)*ng +ng;
figure(9)
if N == 1
    if a ==3
        plot(dngx,Loss,'b','Linewidth',2)
    elseif a==1
        plot(dngx,Loss,'r','Linewidth',2)
    else
        plot(dngx,Loss,'m','Linewidth',2)
    end
end
else
    if a ==3
        plot(dngx,Loss,'g','Linewidth',2)
    elseif a==1
        plot(dngx,Loss,'c','Linewidth',2)
    else
        plot(dngx,Loss,'k','Linewidth',2)
    end
end
end
title('Fabrication Tolerance ng','FontSize',18)
xlabel('ngx (um)','FontSize',14 )
ylabel('Excess Loss (dB)','FontSize',14 )
hold on
dlamdax = dLx/IX1(N)*lamda*1000;
figure(10)
if N == 1
    if a ==3

```

```

        plot(dlamdax,Loss,'b','Linewidth',2)
    elseif a==1
        plot(dlamdax,Loss,'r','Linewidth',2)
    else
        plot(dlamdax,Loss,'m','Linewidth',2)
    end
end
else
    if a ==3
        plot(dlamdax,Loss,'g','Linewidth',2)
    elseif a==1
        plot(dlamdax,Loss,'c','Linewidth',2)
    else
        plot(dlamdax,Loss,'k','Linewidth',2)
    end
end
end
title('3DMMI Optical Bandwidth','FontSize',18)
xlabel('dlamdax (nm)','FontSize',14 )
ylabel('Excess Loss (dB)','FontSize',14 )
hold on
end
end
%SET LEGENDS
figure(8)
legend('General 1x1', 'General 5x5', 'Paired 1x1', 'Paired 5x5', 'Symm 1x1', 'Symm 5x5')
figure(9)
legend('General 1x1', 'General 5x5', 'Paired 1x1', 'Paired 5x5', 'Symm 1x1', 'Symm 5x5')
figure(10)
legend('General 1x1', 'General 5x5', 'Paired 1x1', 'Paired 5x5', 'Symm 1x1', 'Symm 5x5')

```


Appendix B: Detailed SU-8 2050

Process Steps

The follow is a detailed systematic process procedure required to fabricate SU-8 3DMMI waveguide structures along with process procedures for UV-15. The schematic of these details can be reviewed in Fig. 5-1. These procedures are for glass substrates and the SU-8 2050 formulation.

50 μ m Procedure with SU-8 2050

SUBSTRATE PREPARATION: (~ 70min)

label 3 beakers (piranha, sulphuric, and peroxide)
2:1 or 4:1 ratio of (acid to base)
Teflon wafer holder
put on protection gear
add peroxide first
dip in wafers
wash beakers (de-label)
leave for **40min**
take out wafer diagonally
rinse in water
air dry with nitrogen (make sure has no liquid in it)
hotplate dehydration bake **200°C 10min**

COATING OMNICOAT: (~ 10min)

find container, and chuck for the spin
turn on nitrogen

RPM 1: 100, ramp1: 10s, time1: 5s
RPM 2: 500, ramp2: 5s, time2: 5s
RPM 3: 3000, ramp3: 10s, time3: 30s
Ramp4: 20s

pour over all wafers (use dropper)
close lit, Start spin
hotplate **200°C 1min**
let cool to RT

COATING SU-8: (~ 25min)

RPM 1: 100, ramp1: 10s, time1: 5s
RPM 2: 500, ramp2: 5s, time2: 10s
RPM 3: 3150, ramp3: 10s, time3: 30s
Ramp4: 20s

pour SU-8 ~ 1mL/inch of wafer (twist bottle to avoid drip)
close lid, sit for **5min**
start spin
after, let sit **15min**
turn on hotplate to prepare (clean with acetone for uniformity)
turn off nitrogen

SOFT BAKE: (~ 30 min)

avoid light
transfer wafer over WITHOUT TWEEZERS
set **65C 4min**
set **95C 6min**
reset to 65C
transfer to clean paper to cool to RT (can wait 2hr to relax)
turn on Ernie or UV lamps (red button on right, lever on bottom then start)

EXPOSE: (~ 15 min)

align wafer, then mask
use **26mJ/cm²** (when 30.2mW/sq. cm, take ~10s, less with Si)
expose **40s** with Kopp 7380
preheat hotplate @ 65C

PEB: (~ 25 min)

ASAP ASAP after exposure
set **65C 4min**
set **95C 5min**
reset to 65C
transfer to clean paper to cool to RT (can wait 2hr to relax)

DEVELOPE: (~ 15 min)

label container suited for wafer for SU-8 developer
transfer wafer over for strong agitation for **3min (NOTE: 2nd Layer SU-8 ≥ 5min)**
use IPA to check for milky film, is so, develop more (NO WATER NO WATER)
developer goes down drain
rinse container and de-label
blow dry wafer with nitrogen

HARD BAKE (optional): (~ 30 min)

bake in oven for **100C 20min**
make sure no quick ramp to 100C

COATING UV-15: (~ 20min)

find container, and chuck for the spin
turn on nitrogen

RPM 1: 100, ramp1: 10s, time1: 5s
RPM 2: 500, ramp2: 5s, time2: 30s
RPM 3: 500, ramp3: 1s, time3: 0s
Ramp4: 20s

pour over most of wafer (use dropper)
close lit, wait **3min**
start spin
expose **3 J/cm²** (I-line)
apply additional layers as required.

HARD BAKE (optional): (~ 40 min)

bake on hotplate **125°C 30min** after exposure
(Increases crosslink, water resistance, and operating temperature to 150°C)
